CONFIDENTIAL

NACA

RESEARCH MEMORANDUM

LOW-SPEED CASCADE INVESTIGATION OF THIN LOW-CAMBER NACA 65-SERIES BLADE SECTIONS AT HIGH INLET ANGLES

By James C. Emery

Langley Aeronautical Laboratory
Langley Field, Va.

NATIONAL ADVISORY COMMITTEE
FOR AERONAUTICS

WASHINGTON
June 28, 1957

CONFIDENTIAL

ERRATA

NACA Research Memorandum L57E03

By James C. Emery
June 1957

Page 3, line 7:

The definition for θ should be revised as follows:

θ turning angle (angle through which flow is turned by the blade element), deg

In addition, the use of the expression "exit angle" throughout the text should be replaced with the expression "turning angle."

Issued 5-7-58

NATIONAL ADVISORY COMMITTEE FOR AERONAUTICS

RESEARCH MEMORANDUM

LOW-SPEED CASCADE INVESTIGATION OF THIN LOW-CAMBER NACA 65-SERIES BLADE SECTIONS AT HIGH INLET ANGLES

By James C. Emery

SUMMARY

An investigation of 6-percent-thick NACA 65-series compressor blade sections has been conducted in a two-dimensional porous-wall cascade tunnel. Blades cambered to have isolated airfoil lift coefficients of 0, 0.4, 0.8, and 1.2 were tested over the usable angle-of-attack range at inlet-air angles of 60°, 70°, and 75° and solidities of 0.75, 1.00, and 1.50. A few tests were made at a solidity of 2.00.

The results of this investigation indicate a continuous variation of blade-section performance as the major cascade parameters (camber, inlet angle, and solidity) change and provide design information for a range of cascade configurations that heretofore has been supplied by extrapolation.

INTRODUCTION

A systematic series of low-speed cascade tests of the NACA 65-series compressor blades for sections of 10 percent maximum thickness is presented in reference 1. Reference 2 provides information necessary to predict the trend in performance as the blade-section maximum thickness is varied from 6 percent to 15 percent. These data of reference 2, however, are limited to one airfoil-section design, a lift coefficient of 1.2, and two inlet-angle configurations of 45° and 60°.

A large number of successful compressor designs have been based on the low-speed two-dimensional cascade data. However, the range of cascade configurations for which design data were reported in references 1 and 2 is not great enough to include all the configurations used in present compressor design. In particular, the thickness of rotor-tip sections is usually 4 percent to 6 percent of the chord and is seldom as

high as 10 percent. The thickness has an appreciable effect on the design angle of attack at high inlet-air angles. This effect is not predictable without test data.

Additional cascade data in the scope of this paper are needed also for the design of underwater ducted propulsion units. In order to avoid rotor cavitation, it is necessary to design the rotor-tip sections for inlet angles of 70° to 75°, exit angles between 0° and 3°, and thickness-chord ratios between 0.03 and 0.06. Such characteristics are outside the range of published cascade data and cannot be accurately obtained by extrapolation. Current research on underwater rotors indicates that the need will increase for cascade data in the range covered by the present investigation.

Low-speed cascade tests were made by using 6-percent-thick blades cambered to have isolated airfoil coefficients of 0, 0.4, 0.8, and 1.2 over a range of angles of attack at inlet angles of 60°, 70°, and 75° and solidities of 0.75, 1.00, 1.50, and 2.00.

SYMBOLS

c	blade chord, ft
c_d	section drag coefficient based on upstream dynamic pressure
c_l	section lift coefficient based on upstream dynamic pressure
c_{l_o}	camber, expressed as design lift coefficient of isolated airfoil
c_w	wake-momentum-difference coefficient based on upstream dynamic pressure
c_{N_P}	section normal-force coefficient obtained by integration of blade-surface pressure distribution
L/D	lift-drag ratio
R	Reynolds number based on blade chord and entering velocity
P	total pressure
p	static pressure
q	dynamic pressure

S pressure coefficient, $\frac{P - p_l}{q_1}$

t/c maximum thickness-chord ratio

α angle of attack (angle between entering flow and blade chord), deg

β inlet-air angle, angle between inlet-flow direction and perpendicular to a plane through leading edge of airfoils, deg

θ flow exit angle, deg

σ solidity, chord of blade divided by distance between adjacent-blade leading edges

Subscripts:

d design, when used with blades

l local

1 upstream

APPARATUS, TEST PROGRAM, AND PROCEDURE

Apparatus

The test apparatus used in this investigation was a 5-inch low-speed porous-wall cascade tunnel at the Langley Laboratory described in references 1 and 2.

The 5-inch-chord airfoil sections tested were 6-percent-thick NACA 65-series blades and were cambered for a uniform mean-line loading along the chord (a = 1.0, refs. 3 and 4). The rearward portion of the basic blade section was modified to include a trailing-edge radius of 1 percent chord. The amount of camber is expressed in reference 3 as design lift coefficient c_{l_o} (called c_{l_i} in ref. 3) for the isolated airfoil and that notation has been retained. Ordinates and slopes for the a = 1.0 mean line are given for $c_{l_o} = 1.0$ in table II of reference 1. Both ordinates and slopes are scaled directly to obtain other cambers.

Test Program

The test program included various combinations of inlet-air angle, solidity, and camber which are shown in the following table:

σ	Blade cambers at -		
	$\beta = 60^\circ$	$\beta = 70^\circ$	$\beta = 75^\circ$
0.75	0.4 .8 1.2	0.4 .8 1.2	0 .4 .8
1.00	0.4 .8 1.2	0.4 .8 1.2	0 .4 .8
1.50	0.4 .8 1.2	0.4 .8 1.2	0 .4
2.00	0 .4	0 .4	

Procedure

Tests were made by using the porous-wall method as described in reference 5 for each cascade combination listed in the preceding table over a range of angles of attack at intervals of 2° to 3°. Generally, this range covered the interval from negative to positive stall, where stall was indicated by a large increase in drag. The tests were made in a speed range considered incompressible and at a Reynolds number of 245,000 or more. The critical Reynolds number for the test cascade is considered to be about 200,000 (ref. 5).

Surveys of wake total-pressure loss and exit angle were made downstream of the cascade, and blade pressure distributions were measured at the midspan position of the central airfoil at each angle of attack. Upstream pressure and flow direction were measured in the same manner as in reference 2.

Wake-survey and blade-pressure-distribution data were recorded and force values calculated as nondimensional coefficients based numerically

on the upstream dynamic pressure q_1. A detailed derivation of the method of calculating the blade force coefficients is presented in the appendix of reference 1.

ACCURACY OF RESULTS

The accuracy of the measurements of the exit angle and blade normal-force coefficient was somewhat reduced at the inlet angles of 70° and 75°. As inlet angle increases, the wake-free part of the free stream behind the cascade decreases for a constant solidity; therefore, it becomes more difficult to determine accurately the exit angle. The exit angles near design are believed to be within ±1.0° for the inlet angles of 70° and 75° and ±0.5° for the inlet angle of 60°. The blade normal-force coefficient calculated from pressure-rise and momentum considerations was compared with the normal-force coefficient obtained from the blade pressure distribution as a check on the overall accuracy of individual tests. Since these values are directly affected by errors in exit angle, by laminar-separation effects, and by failure to achieve two-dimensionality, the comparison was not as good at inlet angles of 70° and 75° as at 60°. The agreement between normal-force coefficients was within 12 percent for the inlet angles of 70° and 75° and 6 percent for an inlet angle of 60°.

DISCUSSION OF RESULTS

An index to the figures from which the results were obtained is presented in table I. The greatest effect of increasing the inlet-air angle is the increase in static-pressure rise as shown on the blade-surface pressure distributions (figs. 1 to 30). The static-pressure rise for a given exit angle increases markedly as the inlet-air angle increases above 60° since the increase in flow-passage area is a function of the cosine of the flow angles. For example, compare the static-pressure rise for an exit angle of about 5.2° at inlet-air angles of 60° and 75° from figures 1(c) and 24(d). The horizontal line at the 100-percent-chord point on the pressure distribution gives the ratio of the downstream to the upstream dynamic pressure. Subtracting this ratio from 1.00 then gives the ratio of the static-pressure rise to the entering dynamic pressure. This ratio is 0.17 for the 60° case and 0.27 for the 75° case. Since, for a given exit angle, the static-pressure rise changes rapidly with changes in inlet angle, the range of usable turning angles is decreased at the higher inlet angles.

Summaries of the relationships between exit angle and angle of attack for four cambers are presented in figure 31. The rate of change of exit angle with angle of attack is, in general, about the same for all cambers at a given solidity. Figure 32 shows the variation of design exit angle and design angle of attack with camber. For a given solidity and inlet-air angle, θ_d and α_d appear to vary linearly with camber. The estimated useful operating range for the various sections at the solidities and inlet angles tested was based on an index of twice minimum drag and is presented in figure 33. As expected, the operating range generally becomes smaller as the inlet angle is increased. The decrease in range is greatest at the highest solidity, probably because of the greater changes in passage-area distribution. The smaller operating range is also attributed to the profile thickness (ref. 2) and to the greater increase in pressure rise for a given increase in exit angle at the higher inlet-air angles. Near design angle of attack, the drag and lift-drag ratios are reasonable and compare favorably with thicker sections surveyed at lower inlet angles (ref. 1).

Design Angle of Attack

In references 1 and 2, the design angle of attack is defined as the angle which gives a peak-free pressure distribution and was found to be constant for each solidity over a lower range of inlet angles. The design angle of attack decreases at higher inlet angles. Figure 34 gives the variation of design angle of attack and design exit angle with inlet angle for each solidity. The maximum change in α_d and θ_d was 2° for a solidity of 0.75. The minimum occurred in α_d for the noncambered airfoil at a solidity of 2.00. This decrease in design angle of attack is associated with the variation of c_{N_p} at constant angle of attack with inlet angles as presented in figure 35. This plot indicates that, as inlet angle increases, the normal-force coefficient increases and, as a result, the lift coefficient per blade increases and each blade in the cascade approaches an isolated airfoil condition. Therefore, the design angle of attack, when selected in the usual manner (peak-free pressure distribution) will decrease at the higher inlet angles as shown by the carpet plot (fig. 36). This change in design angle of attack at high inlet angles is significant because of the narrow operating range associated with high pressure-rise conditions.

Carpet Plots

Inasmuch as design angle of attack and design exit angle are functions of camber, solidity, and inlet angle, the carpet-plotting technique (ref. 6) is used to present these values. A carpet plot of design angle of attack as a function of camber, solidity, and inlet angle is presented

in figure 36. A carpet plot of blade camber as a function of inlet-air angle, exit angle, and solidity is given in figure 37.

CONCLUSIONS

The low-speed two-dimensional cascade investigation of NACA 65-series thin low-camber blades at high inlet angles provides design data for a range of cascade configurations which heretofore has depended, in most instances, on extrapolation from lower inlet angles and thicker blade sections. In addition, the following conclusions are significant:

1. The design angle of attack decreases with increasing inlet-air angle, particularly for low solidities.

2. Near design angle of attack, the thin low-camber blade sections have low drag and a lift-drag ratio comparable to thicker sections tested at lower inlet angles.

3. The useful operating angle-of-attack range, in general, decreases as inlet angle increases.

Langley Aeronautical Laboratory,
National Advisory Committee for Aeronautics,
Langley Field, Va., April 10, 1957.

REFERENCES

1. Herrig, L. Joseph, Emery, James C., and Erwin, John R.: Systematic Two-Dimensional Cascade Tests of NACA 65-Series Compressor Blades at Low Speeds. NACA TN 3916, 1957. (Supersedes NACA RM L51G31.)

2. Herrig, L. Joseph, Emery, James C., and Erwin, John R.: Effect of Section Thickness and Trailing-Edge Radius on the Performance of NACA 65-Series Compressor Blades in Cascade at Low Speeds. NACA RM L51J16, 1951.

3. Abbott, Ira H., von Doenhoff, Albert E., and Stivers, Louis S., Jr.: Summary of Airfoil Data. NACA Rep. 824, 1945. (Supersedes NACA WR L-560.)

4. Erwin, John R., and Yacobi, Laura A.: Method of Estimating the Incompressible-Flow Pressure Distribution of Compressor Blade Sections at Design Angle of Attack. NACA RM L53F17, 1953.

5. Erwin, John R., and Emery, James C.: Effect of Tunnel Configuration and Testing Technique on Cascade Performance. NACA Rep. 1016, 1951. (Supersedes NACA TN 2028.)

6. Felix, A. Richard: Summary of 65-Series Compressor-Blade Low-Speed Cascade Data by Use of the Carpet-Plotting Technique. NACA TN 3913, 1957. (Supersedes NACA RM L54H18a.)

TABLE I.- INDEX TO FIGURES

NACA Blade sections	Solidity	Inlet-air angle	Description of figures	Figure
65-(0)06 65-($4A_{10}$)06 65-($8A_{10}$)06 65-($12A_{10}$)06	0.75, 1.00, 1.50, and 2.00	60°, 70°, and 75°	Detailed blade performance and summary plots	1 to 30
65-(0)06 65-($4A_{10}$)06 65-($8A_{10}$)06 65-($12A_{10}$)06	0.75, 1.00, 1.50, and 2.00	60°, 70°, and 75°	Summaries of the relationship between exit angle and angle of attack	31
65-($4A_{10}$)06 65-($8A_{10}$)06 65-($12A_{10}$)06	0.75, 1.00, and 1.50	60°	Variation of design exit angle and design angle of attack with camber at an inlet angle of 60°	32a
65-($4A_{10}$)06 65-($8A_{10}$)06 65-($12A_{10}$)06	0.75, 1.00, and 1.50	70°	Variation of design exit angle and design angle of attack with camber at an inlet angle of 70°	32b
65-(0)06 65-($4A_{10}$)06 65-($8A_{10}$)06	0.75, 1.00, and 1.50	75°	Variation of design exit angle and design angle of attack with camber at an inlet angle of 75°	32c
65-($4A_{10}$)06 65-($8A_{10}$)06 65-($12A_{10}$)06	0.75, 1.00, and 1.50	60°, 70°, and 75°	Variation of the estimated operating angle-of-attack range with inlet angle for several cambers	33
	0.75, 1.00, and 1.50		Variation of θ_d and α_d with three inlet angles for each solidity	34
65-($4A_{10}$)10 65-($4A_{10}$)06 65-($8A_{10}$)10 65-($8A_{10}$)06	0.75 and 1.00	30°, 45°, 60°, 70°, and 75°	Variation of c_{N_p} with inlet angle at constant angle of attack	35
65-(0)06 65-($4A_{10}$)06 65-($8A_{10}$)06 65-($12A_{10}$)06	0.75, 1.00, and 1.50	60°, 70°, and 75°	Carpet plots of design angle of attack and design exit angle	36 to 37

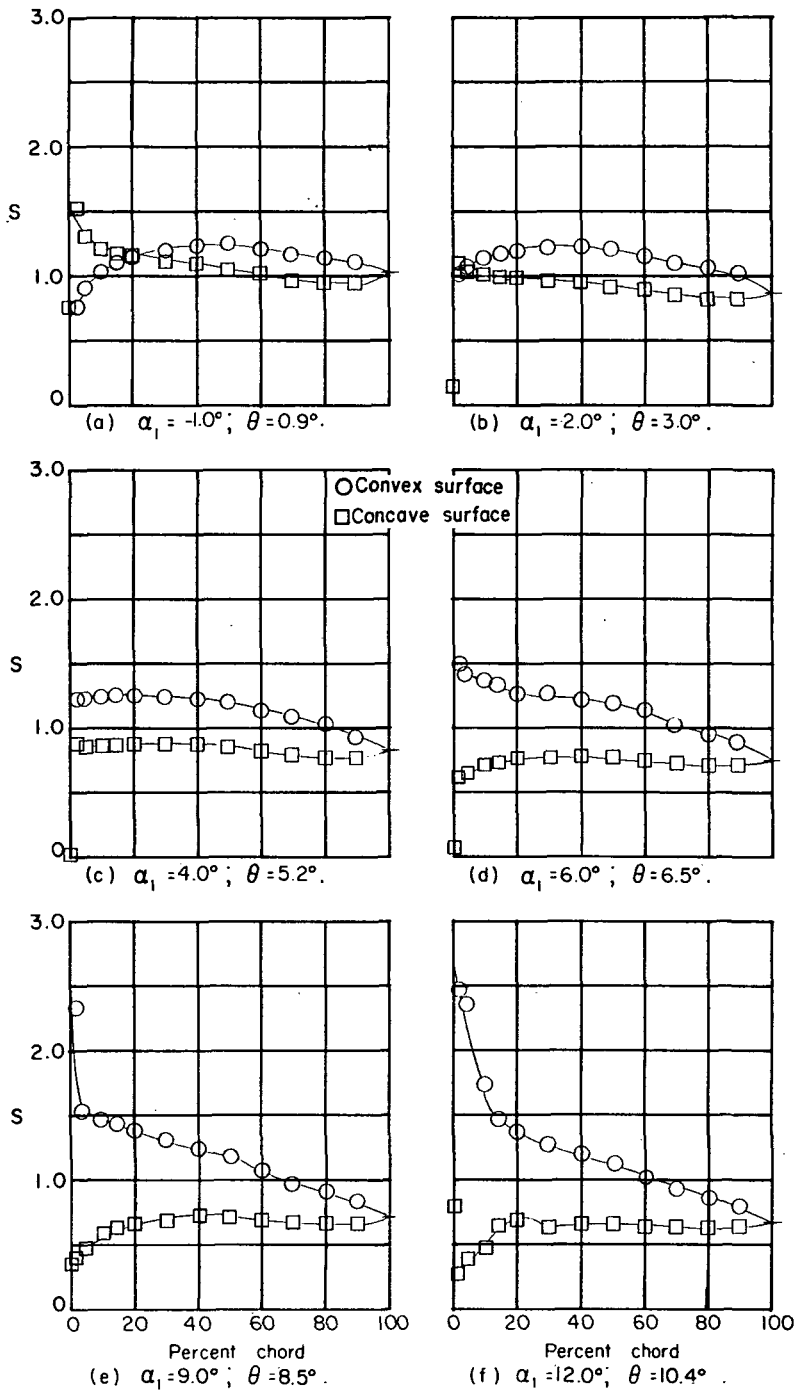

Figure 1.- Blade-surface pressure distributions and section characteristics for the cascade combination $\beta = 60°$, $\sigma = 0.75$, and blade section NACA 65-$(4A_{10})$06.

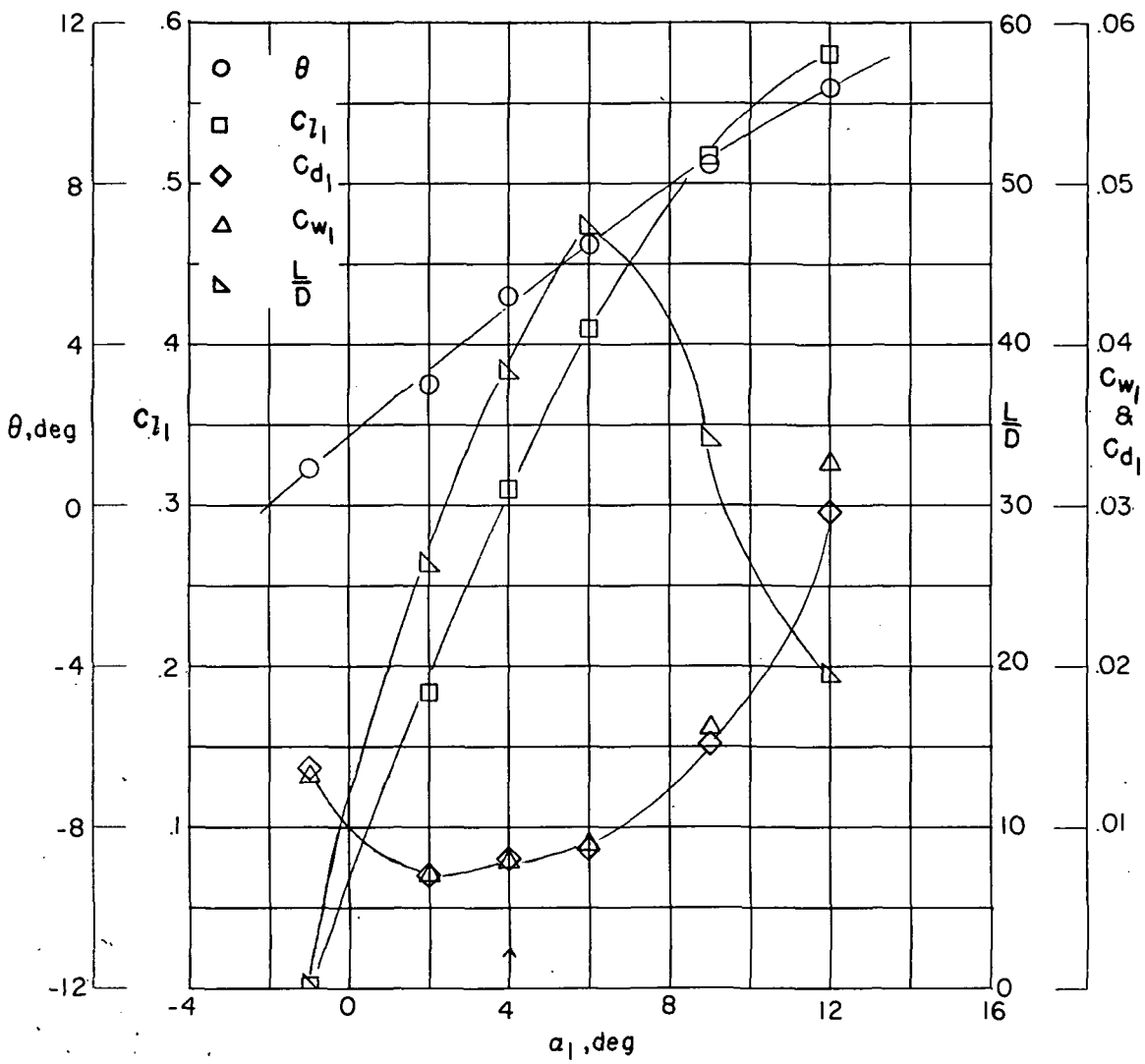

(g) Section characteristics. NACA 65-$(4A_{10})$06; β = 60°; σ = 0.75; R = 346,000. Arrow shows α_d.

Figure 1.- Concluded.

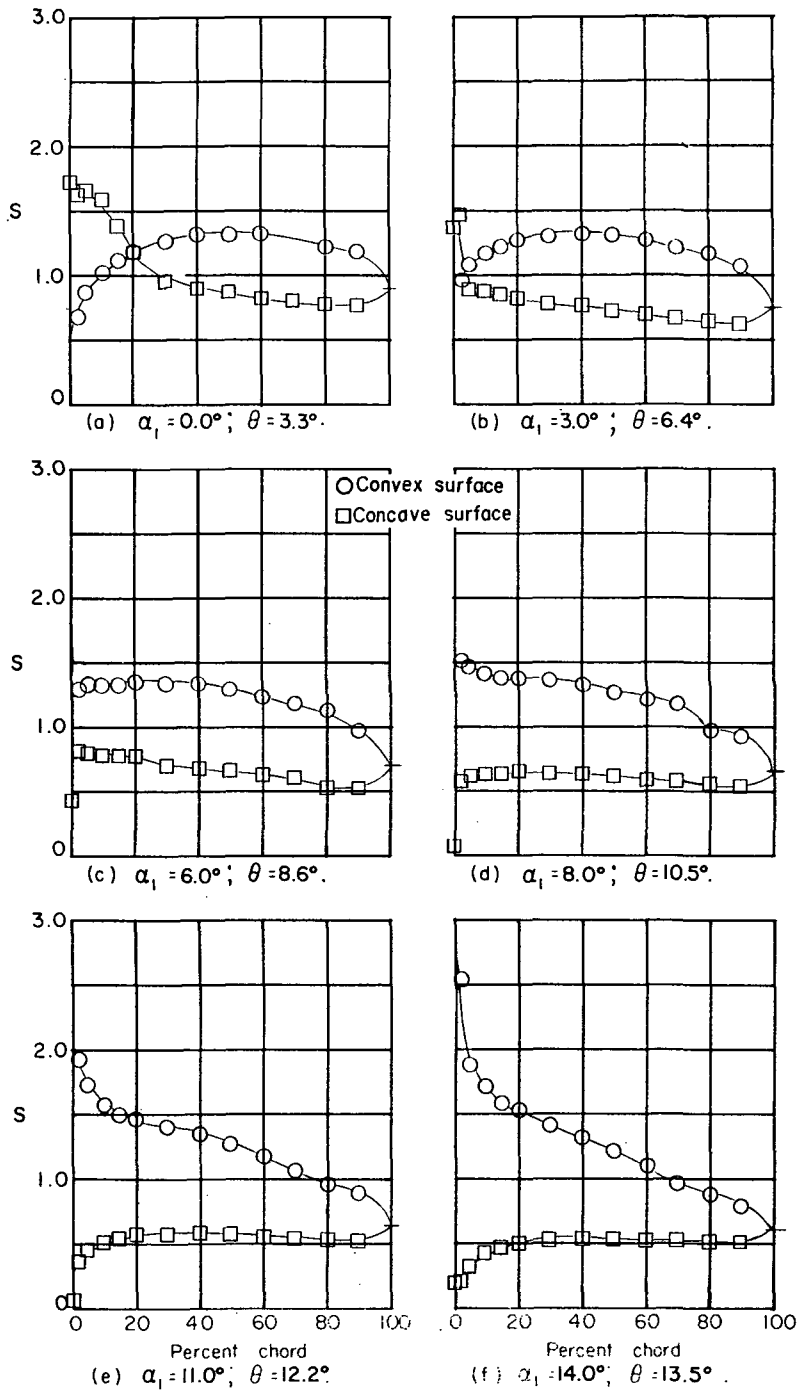

Figure 2.- Blade-surface pressure distributions and section characteristics for the cascade combination $\beta = 60^\circ$, $\sigma = 0.75$, and blade section NACA 65-$(8A_{10})$06.

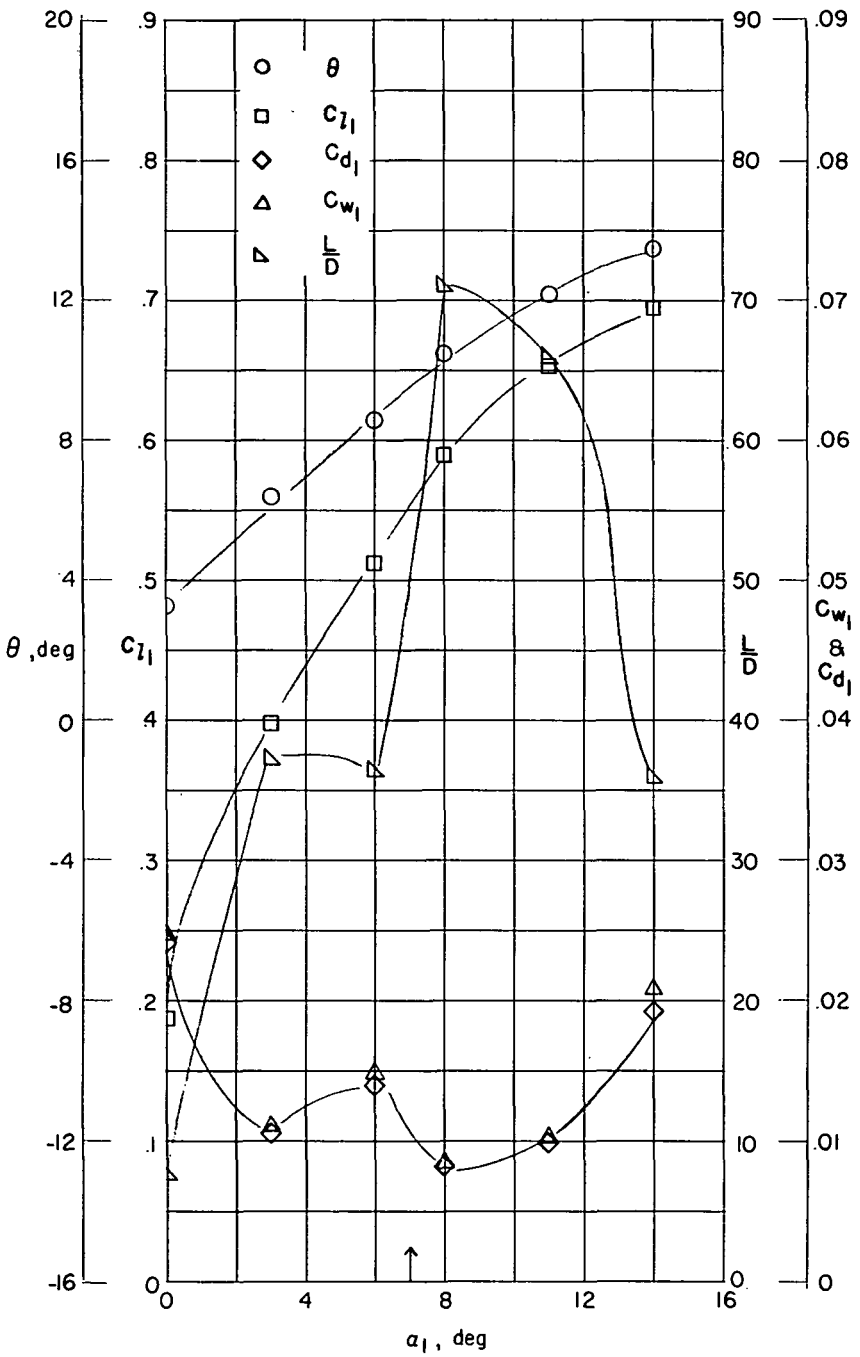

(g) Section characteristics. NACA 65-$(8A_{10})$06; β = 60°; σ = 0.75; R = 346,000. Arrow shows α_d.

Figure 2.- Concluded.

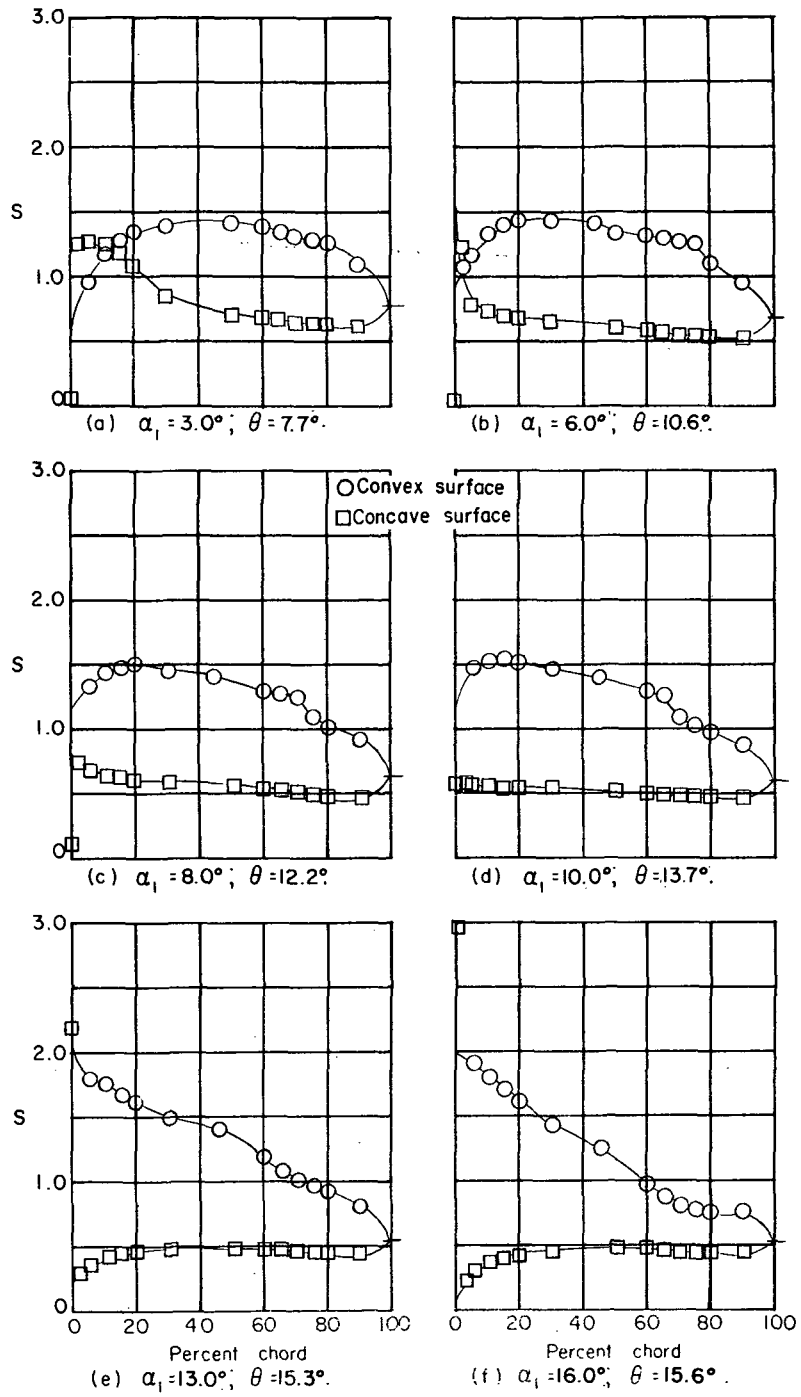

Figure 3.- Blade-surface pressure distributions and section characteristics for the cascade combination $\beta = 60°$, $\sigma = 0.75$, and blade section NACA 65-$(12A_{10})$06.

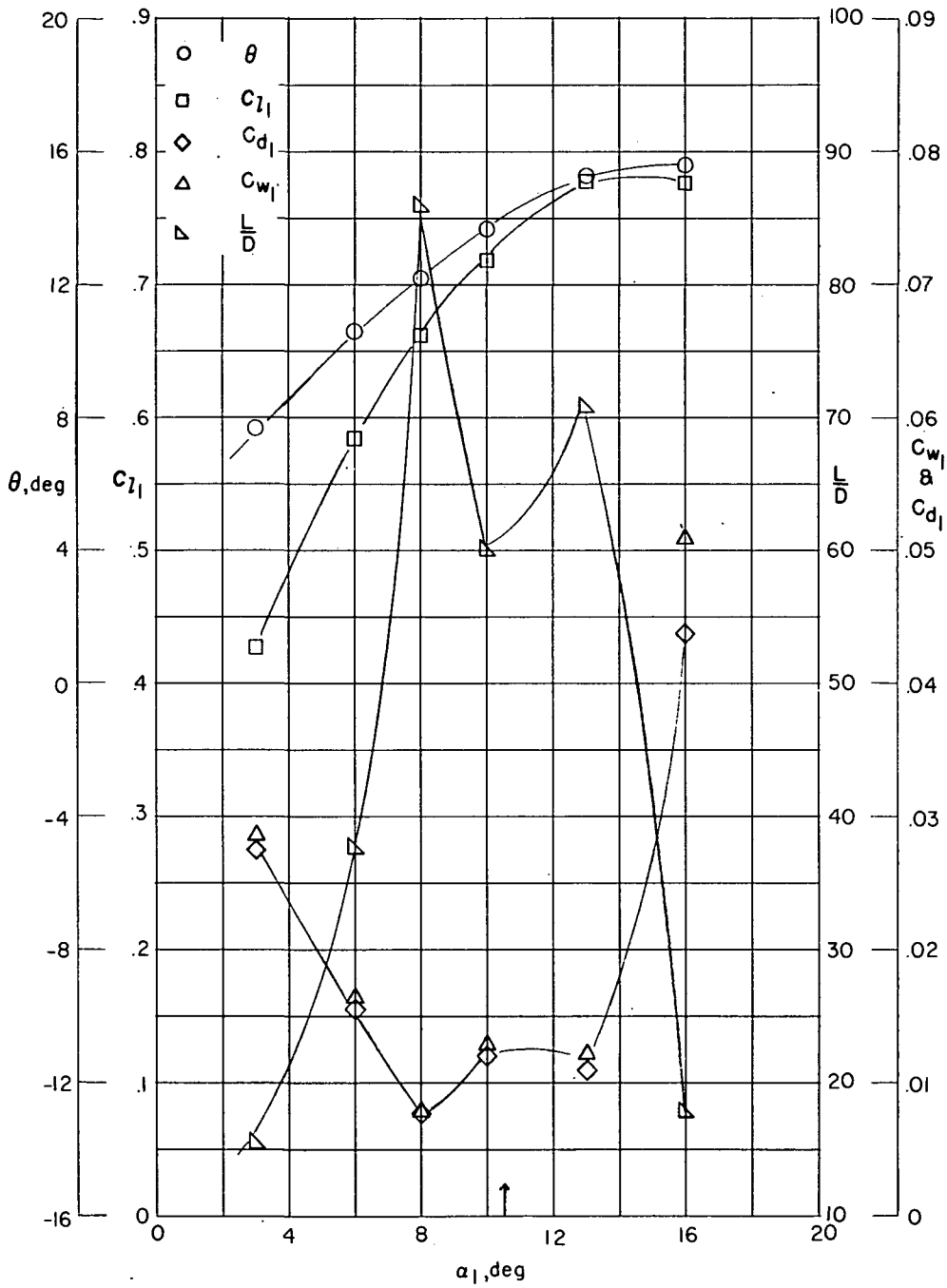

(g) Section characteristics. NACA 65-$(12A_{10})$06; $\beta = 60^{\circ}$; $\sigma = 0.75$; R = 346,000. Arrow shows α_d.

Figure 3.- Concluded.

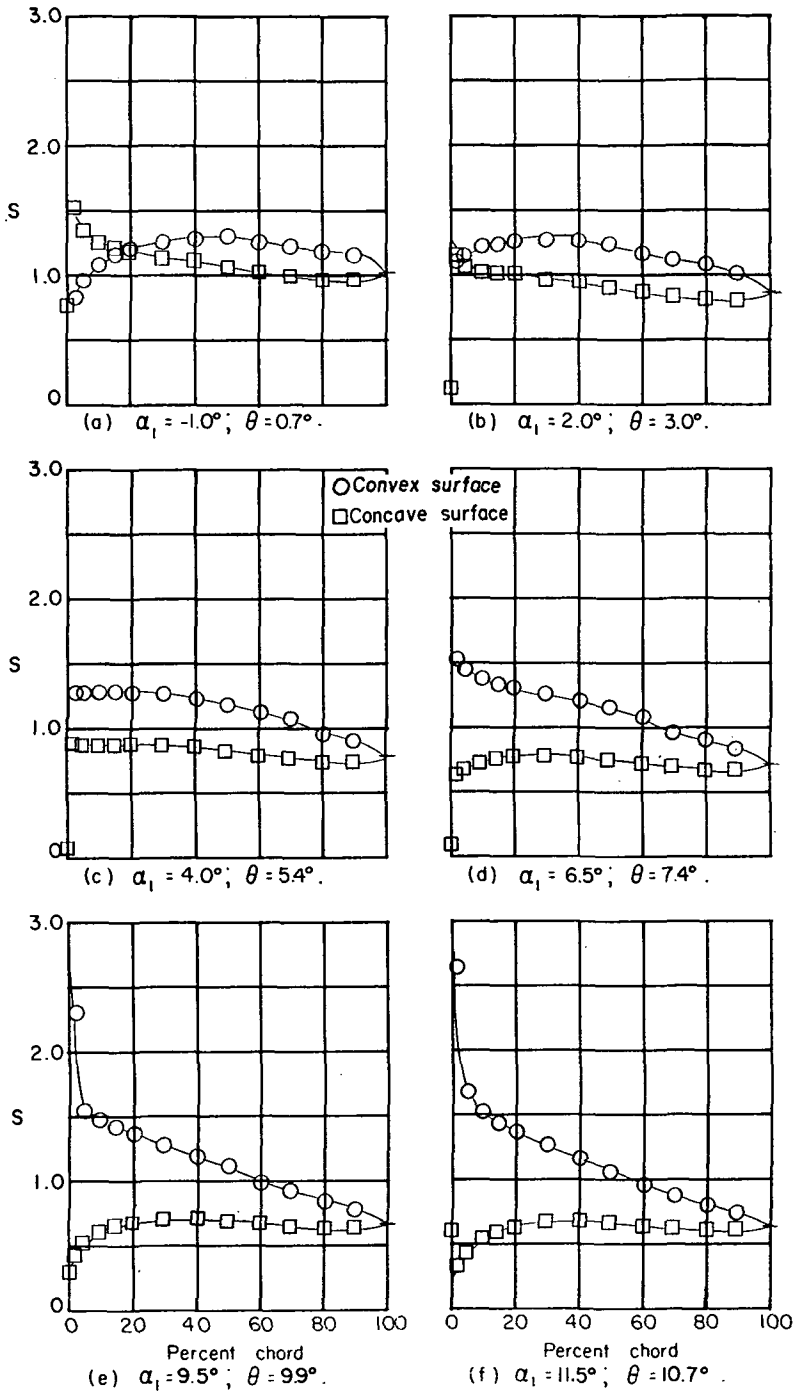

Figure 4.- Blade-surface pressure distributions and section characteristics for the cascade combination $\beta = 60°$, $\sigma = 1.00$, and blade section NACA 65-$(4A_{10})$06.

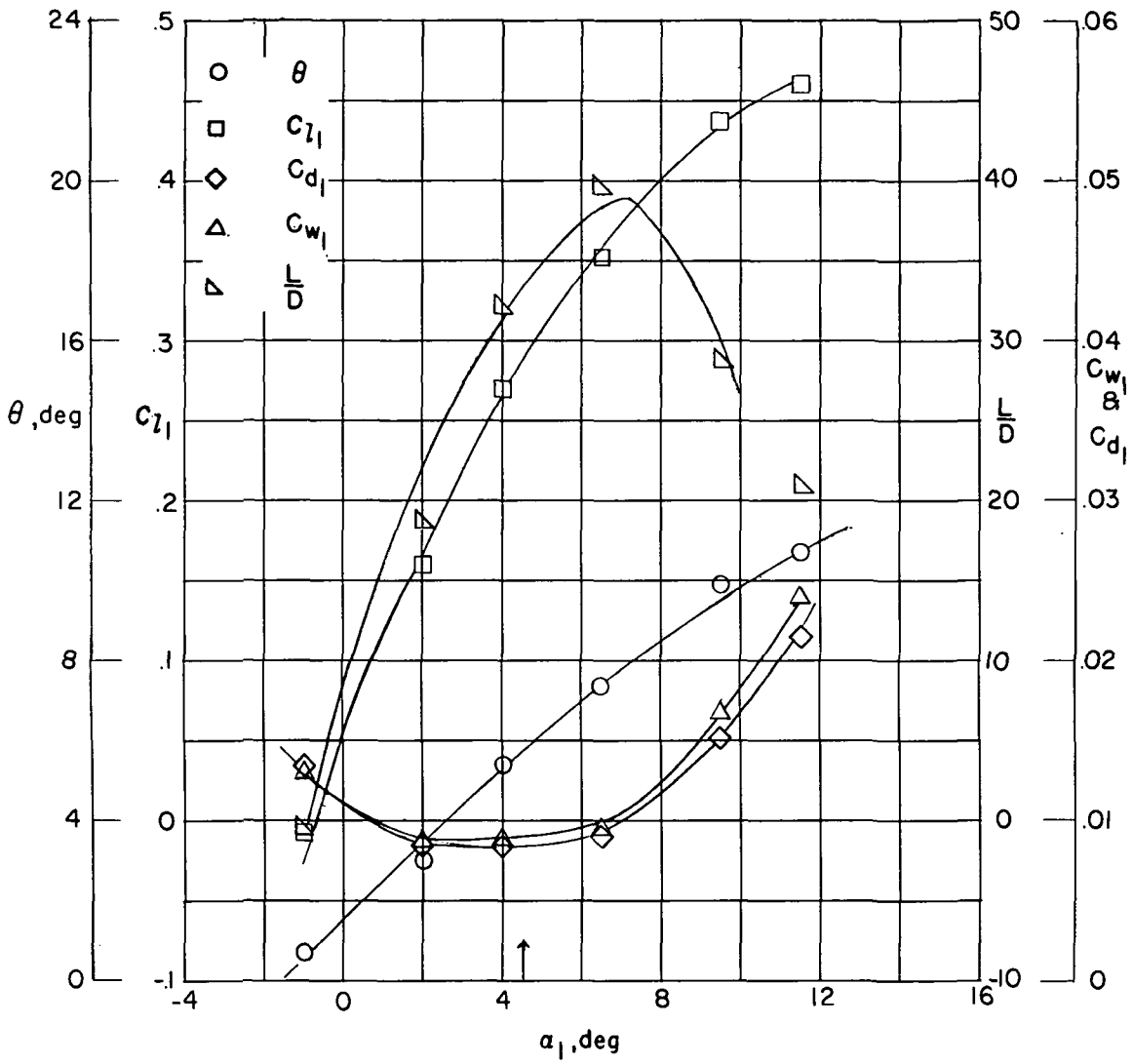

(g) Section characteristics. NACA 65-$(4A_{10})$06; $\beta = 60^\circ$; $\sigma = 1.00$; R = 346,000. Arrow shows α_d.

Figure 4.- Concluded.

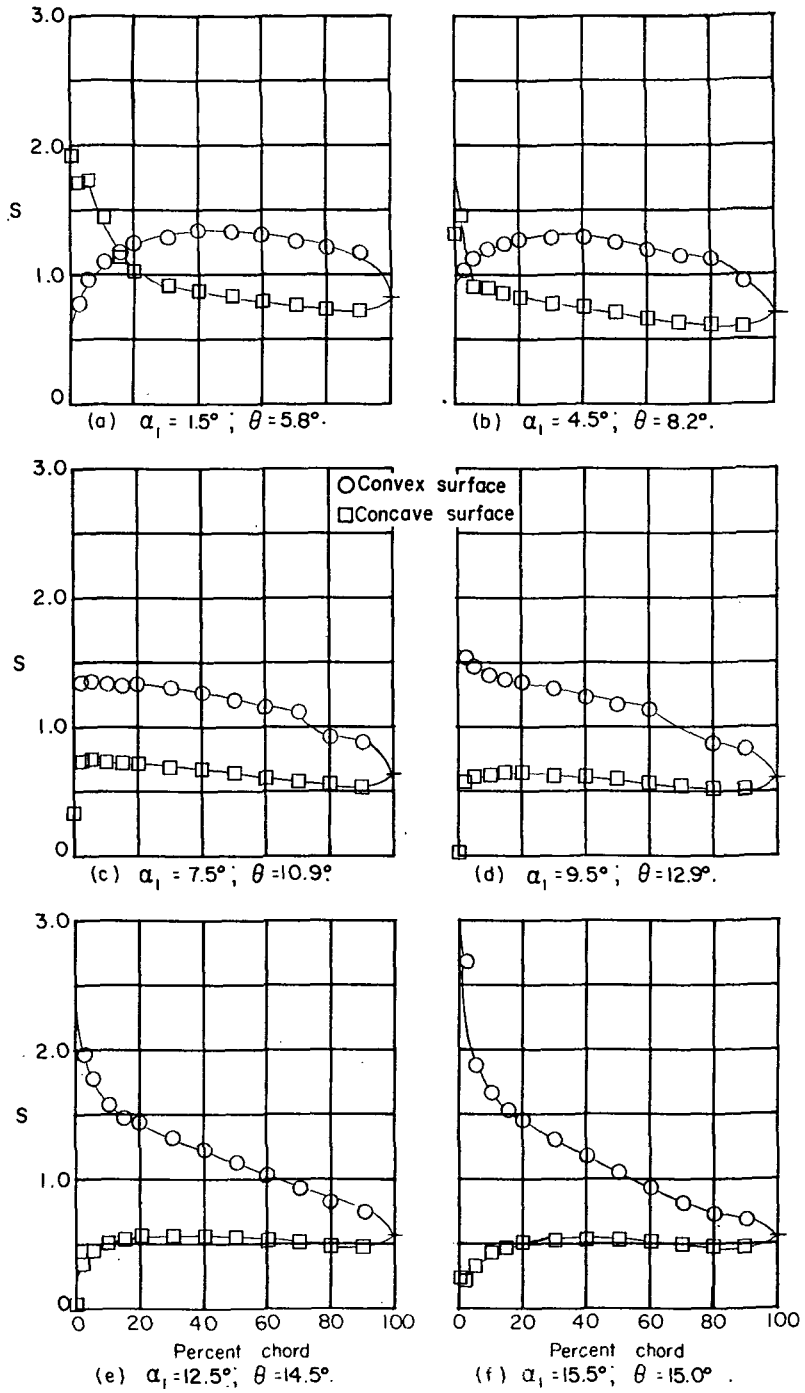

Figure 5.- Blade-surface pressure distributions and section characteristics for the cascade combination $\beta = 60^\circ$, $\sigma = 1.00$, and blade section NACA 65-$(8A_{10})$06.

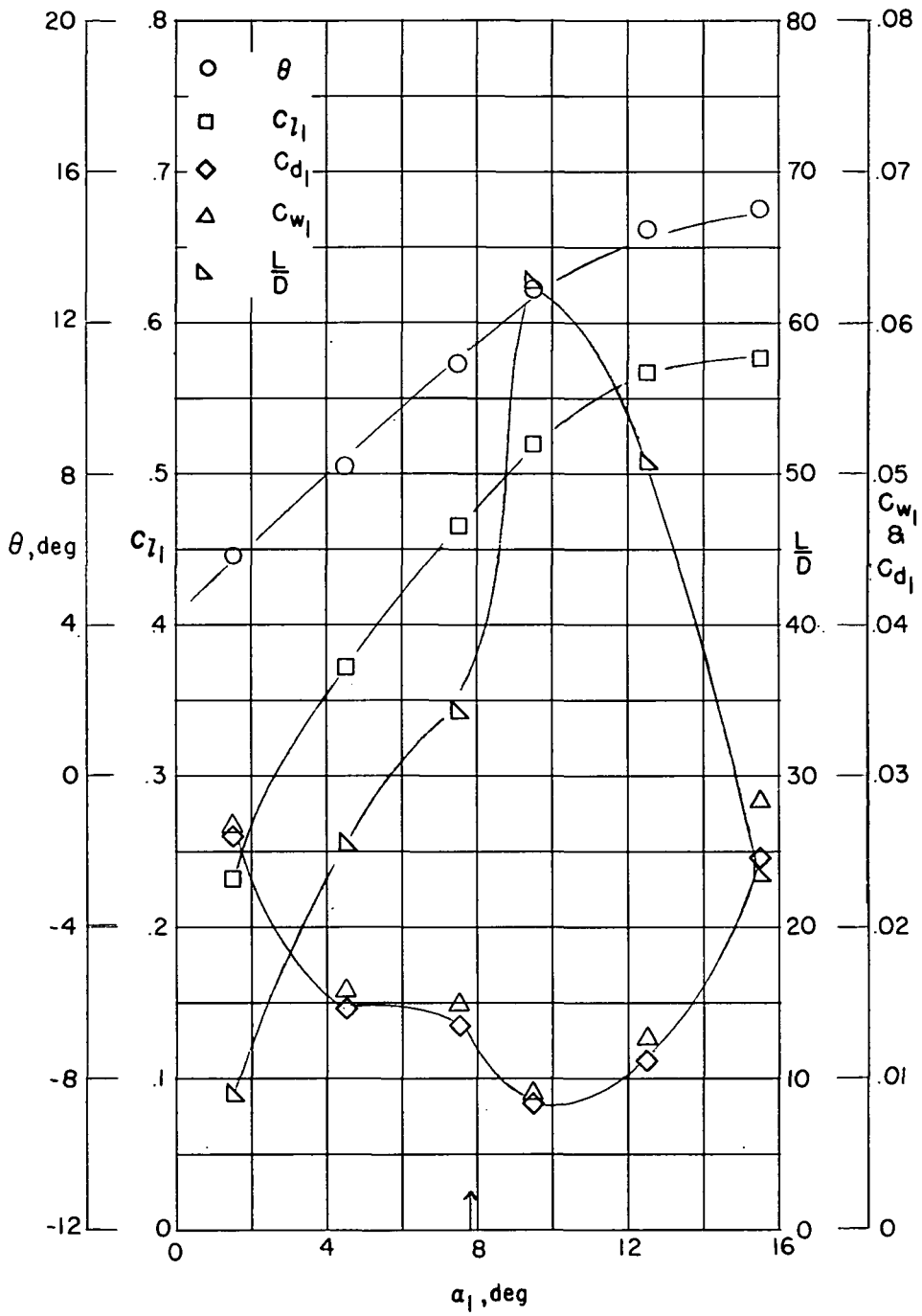

(g) Section characteristics. NACA 65-$(8A_{10})$06; β = 60°; σ = 1.00; R = 346,000. Arrow shows α_d.

Figure 5.- Concluded.

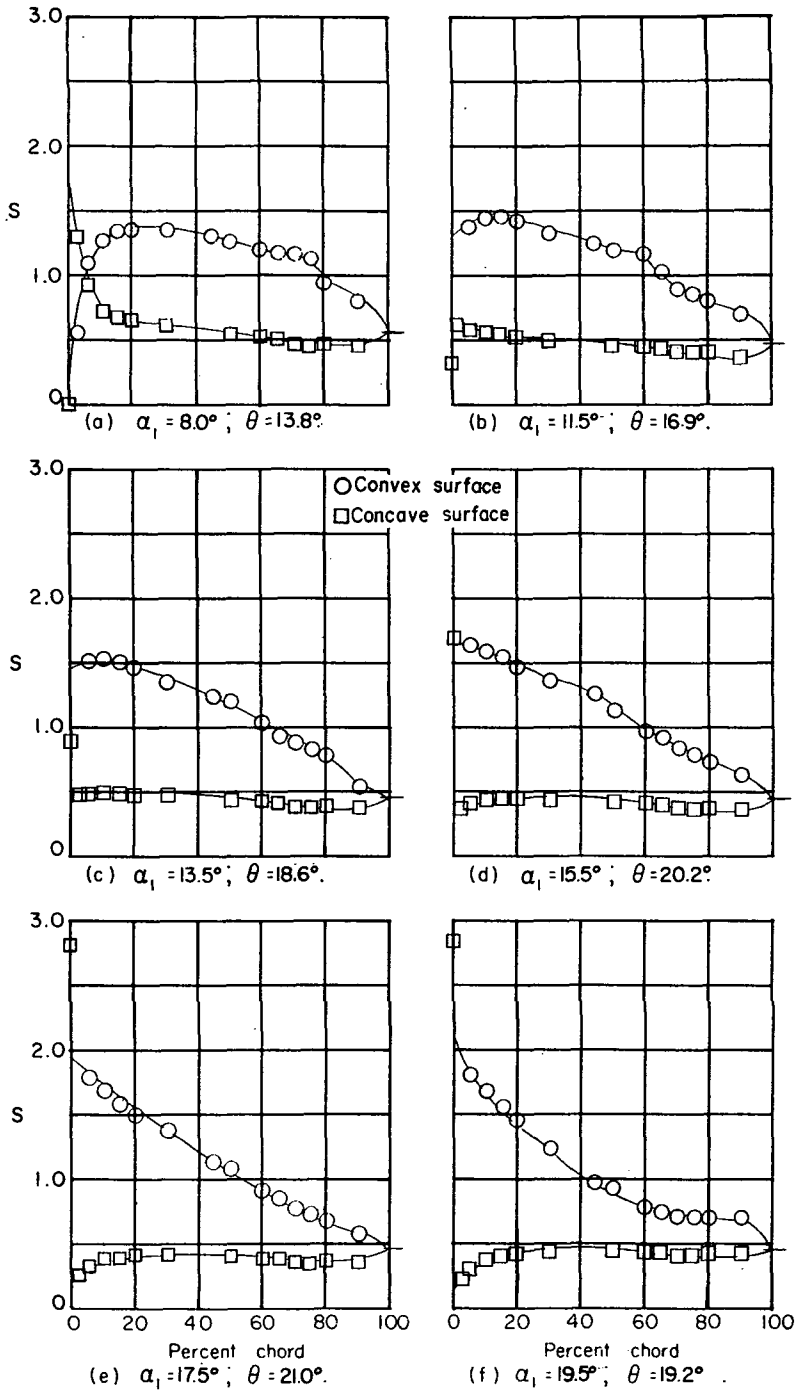

Figure 6.- Blade-surface pressure distributions and section characteristics for the cascade combination $\beta = 60^\circ$, $\sigma = 1.00$, and blade section NACA 65-$(12A_{10})$06.

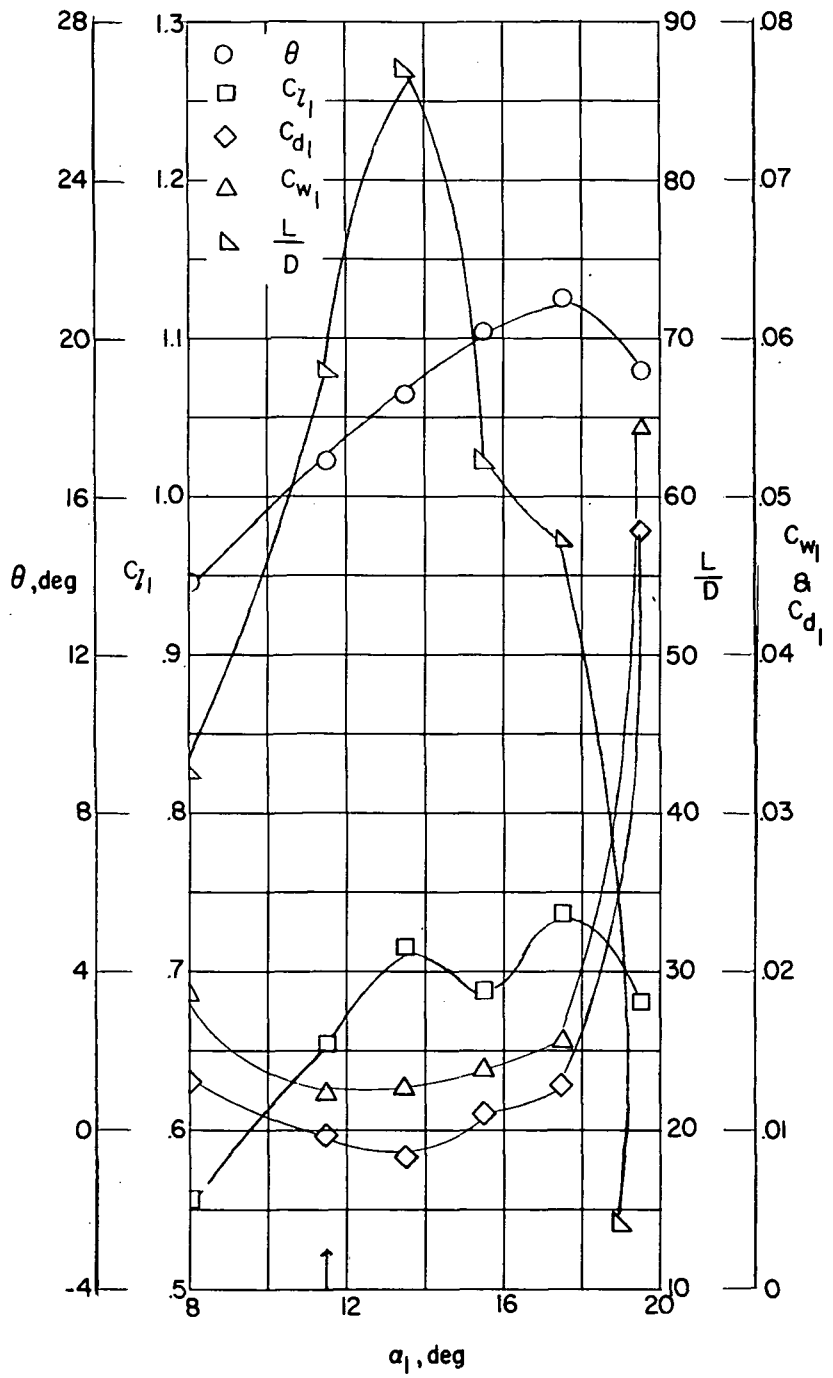

(g) Section characteristics. NACA 65-$(12A_{10})$06; $\beta = 60°$; $\sigma = 1.00$; $R = 245{,}000$. Arrow shows α_d.

Figure 6.- Concluded.

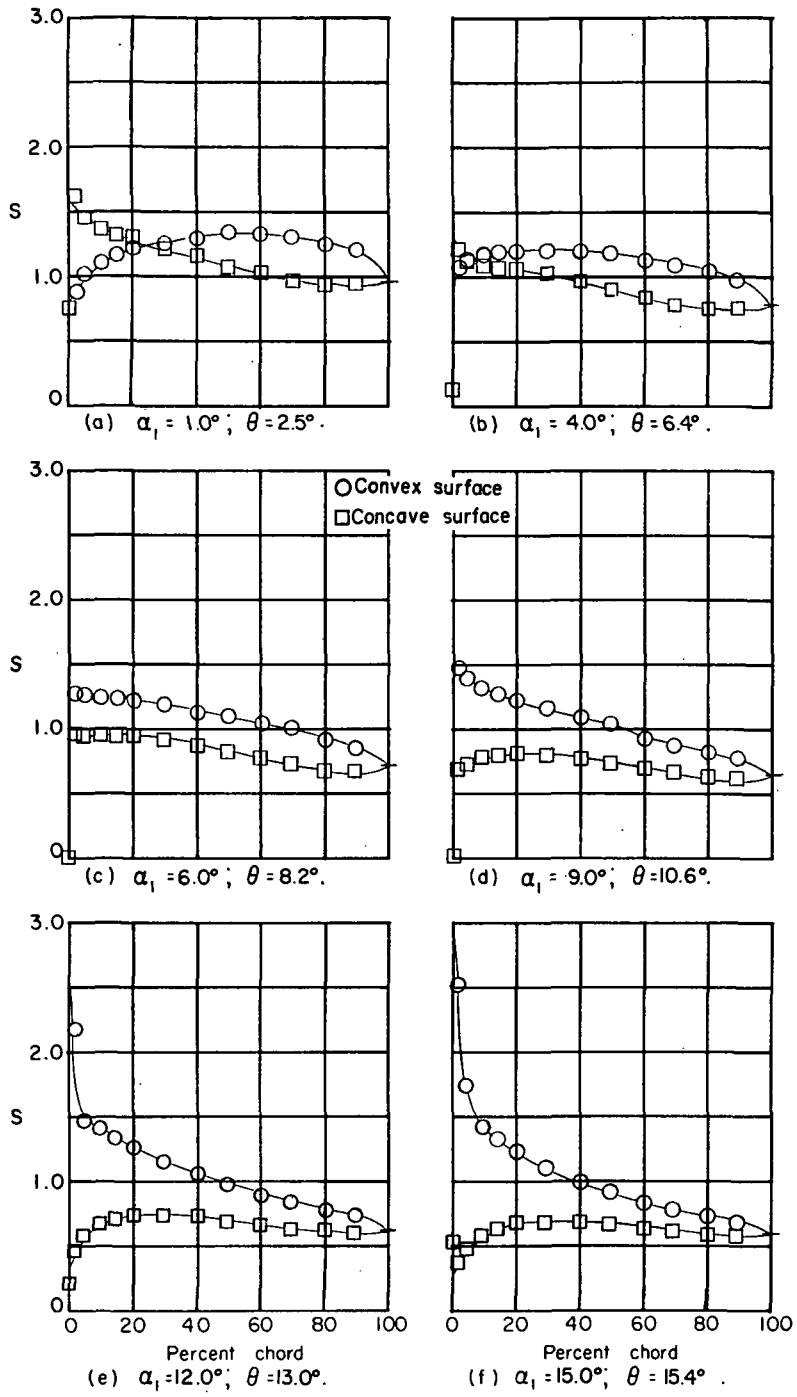

Figure 7.- Blade-surface pressure distributions and section characteristics for the cascade combination $\beta = 60^\circ$, $\sigma = 1.50$, and blade section NACA 65-$(4A_{10})$06.

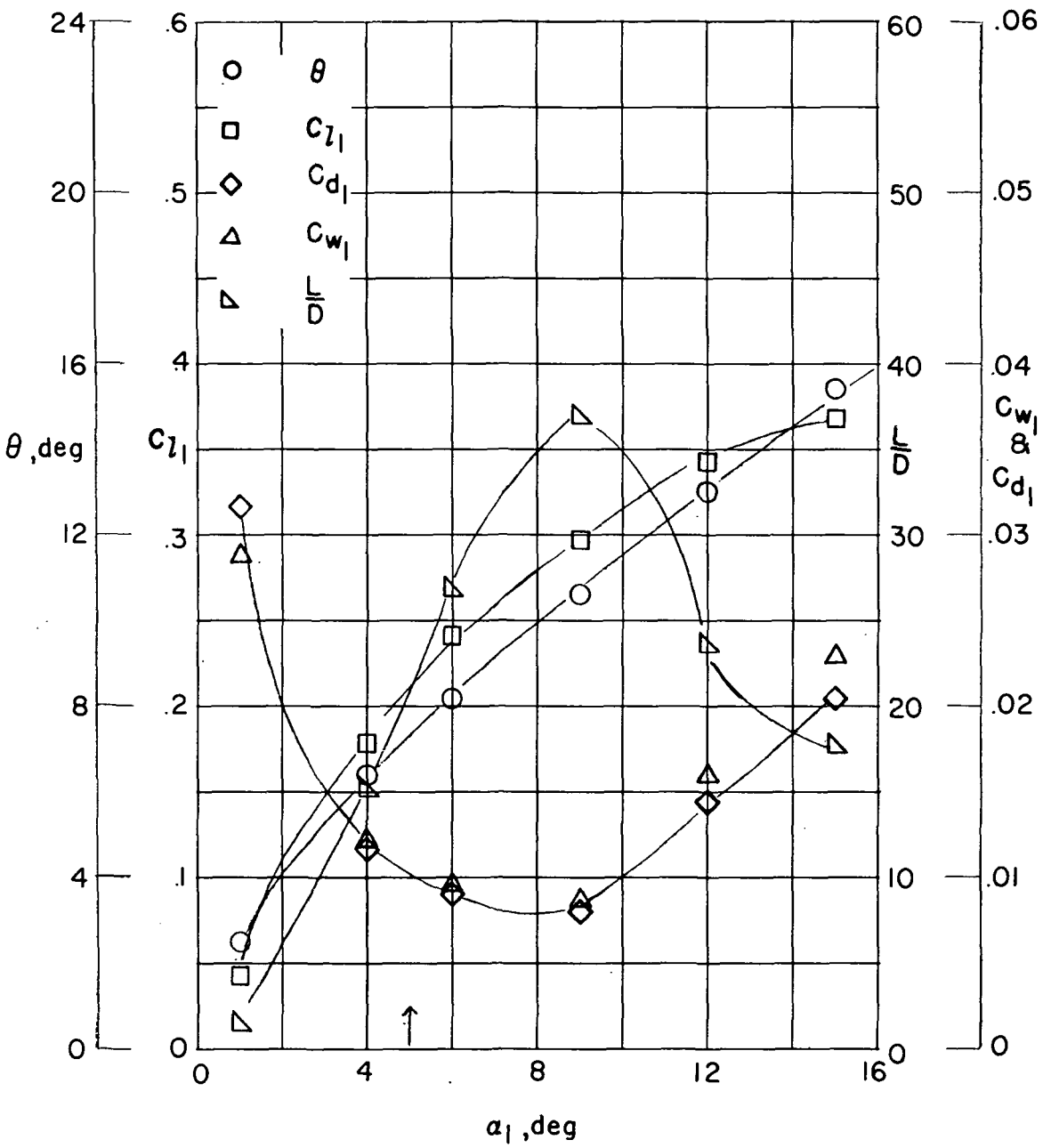

(g) Section characteristics. NACA 65-$(4A_{10})$06; $\beta = 60°$; $\sigma = 1.50$; R = 346,000. Arrow shows α_d.

Figure 7.- Concluded.

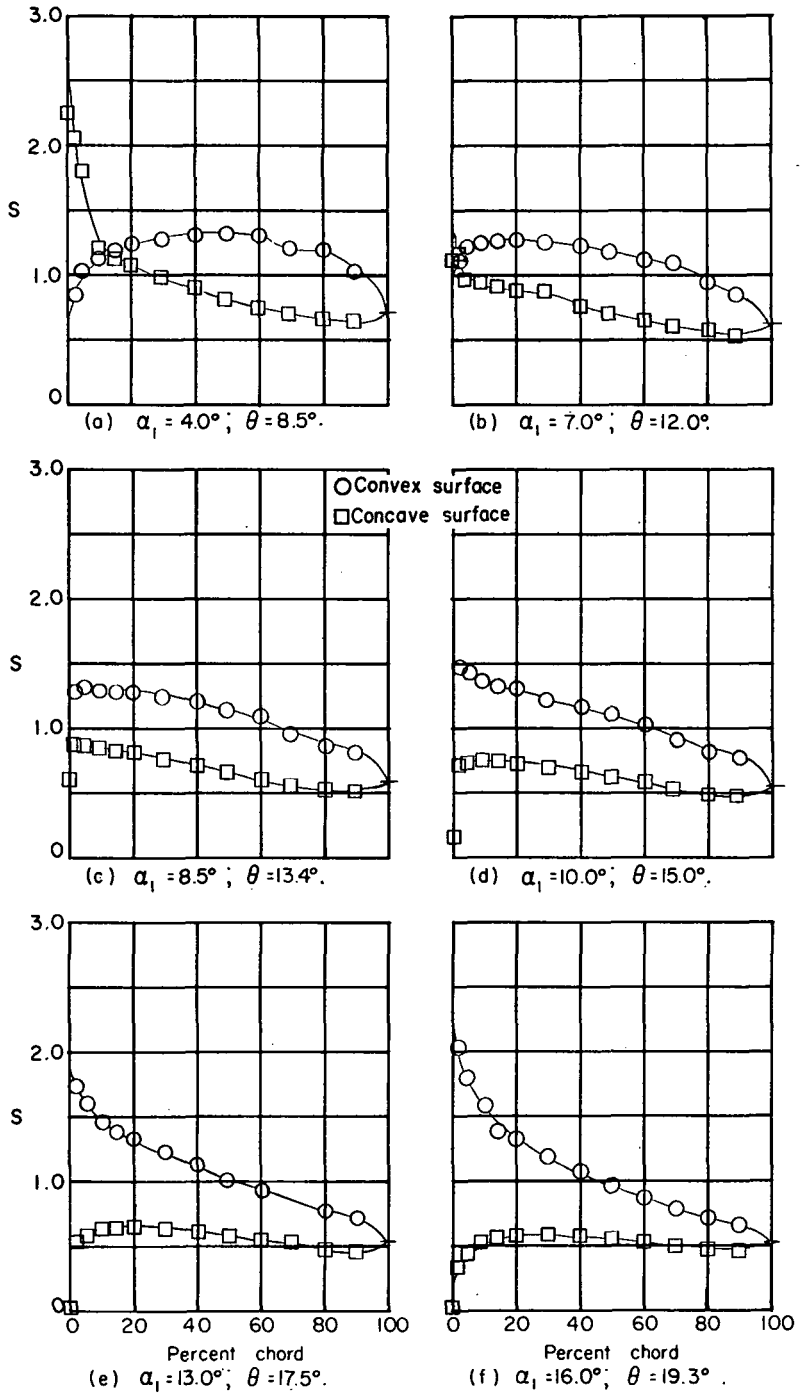

Figure 8.- Blade-surface pressure distributions and section characteristics for the cascade combination $\beta = 60°$, $\sigma = 1.50$, and blade section NACA 65-$(8A_{10})$06.

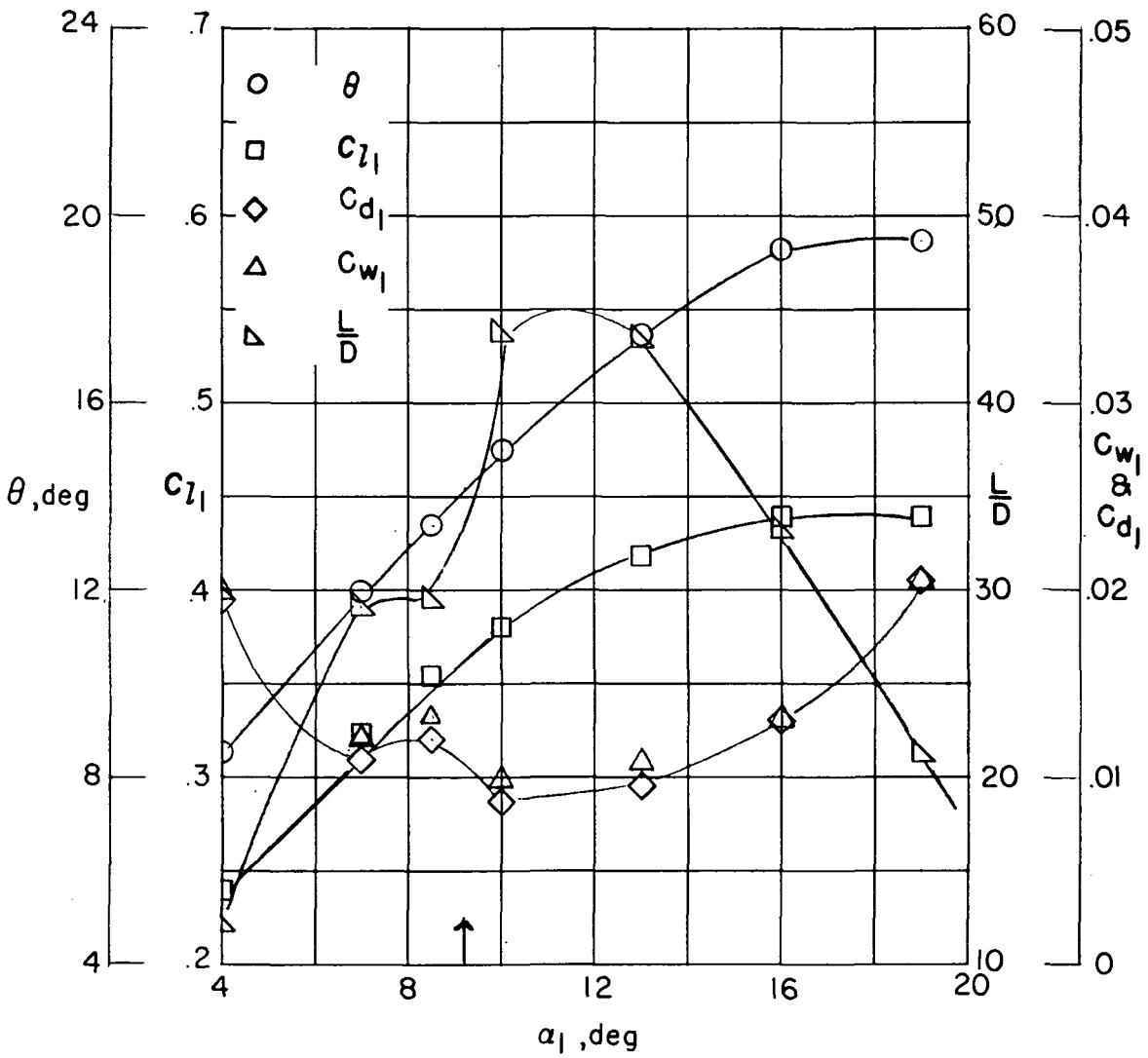

(g) Section characteristics. NACA 65-$(8A_{10})$06; β = 60°; σ = 1.50; R = 346,000. Arrow shows α_d.

Figure 8.- Concluded.

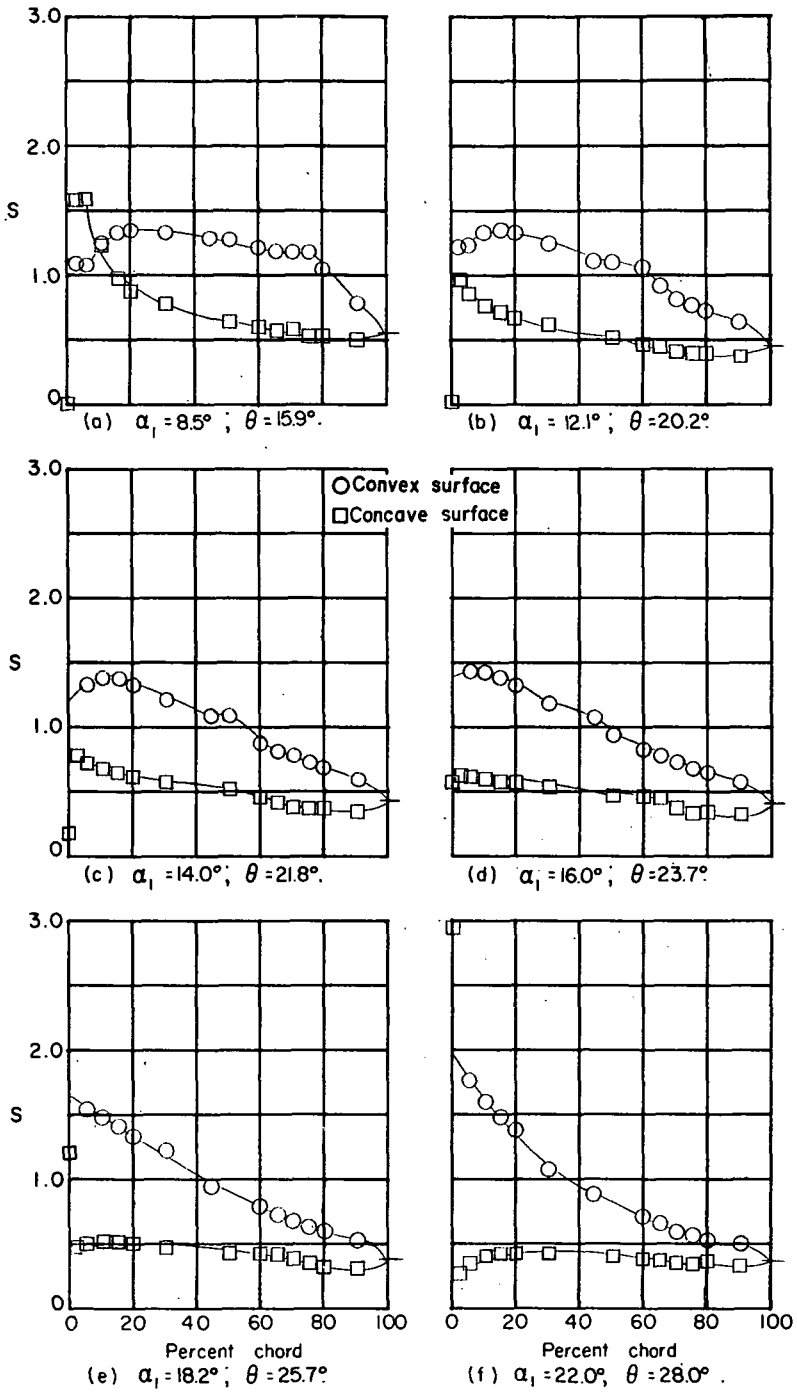

Figure 9.- Blade-surface pressure distributions and section characteristics for the cascade combination $\beta = 60^\circ$, $\sigma = 1.50$, and blade section NACA 65-$(12A_{10})$06.

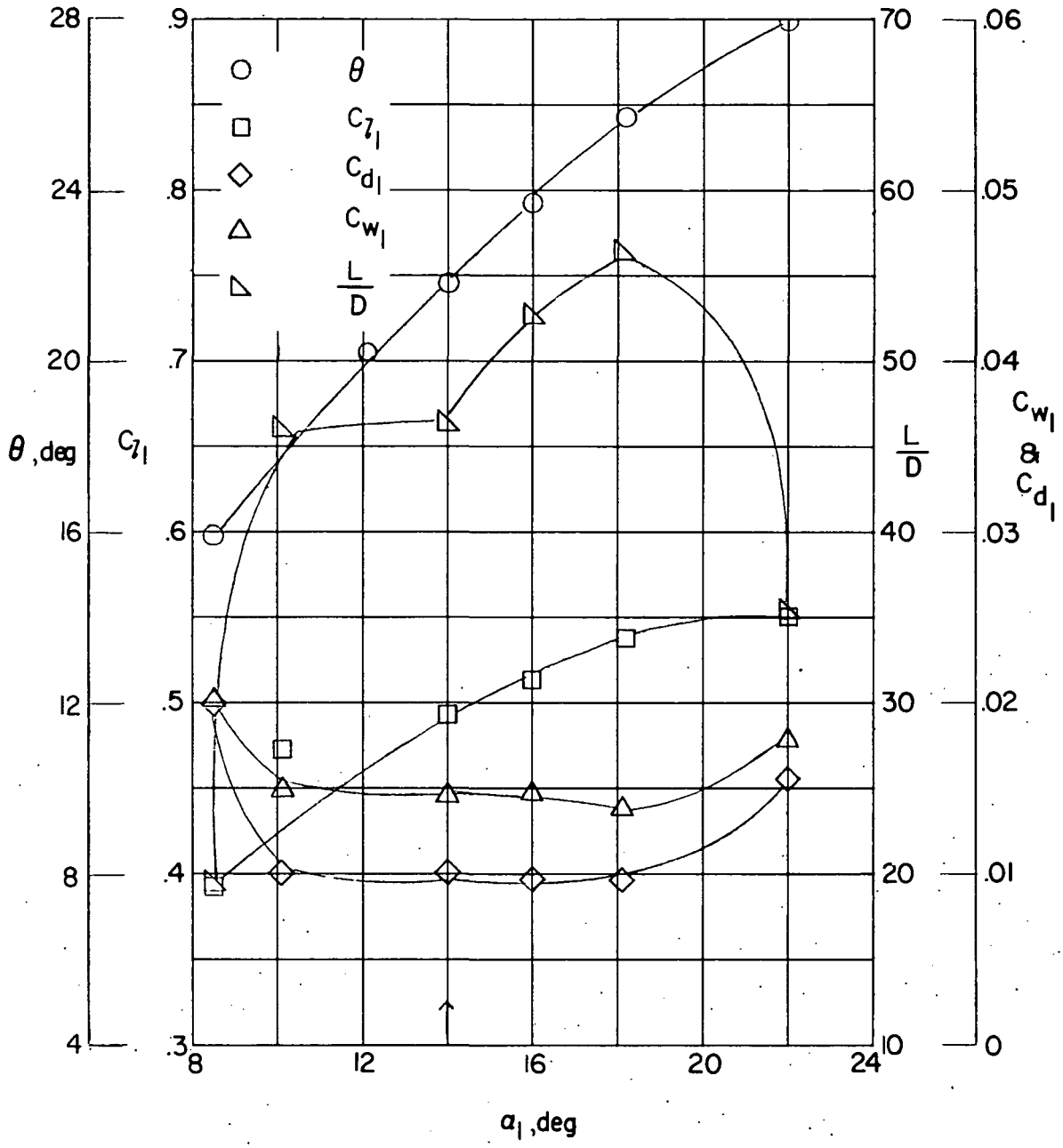

(g) Section characteristics. NACA 65-$(12A_{10})$06; $\beta = 60^\circ$; $\sigma = 1.50$; R = 245,000. Arrow shows α_d.

Figure 9.- Concluded.

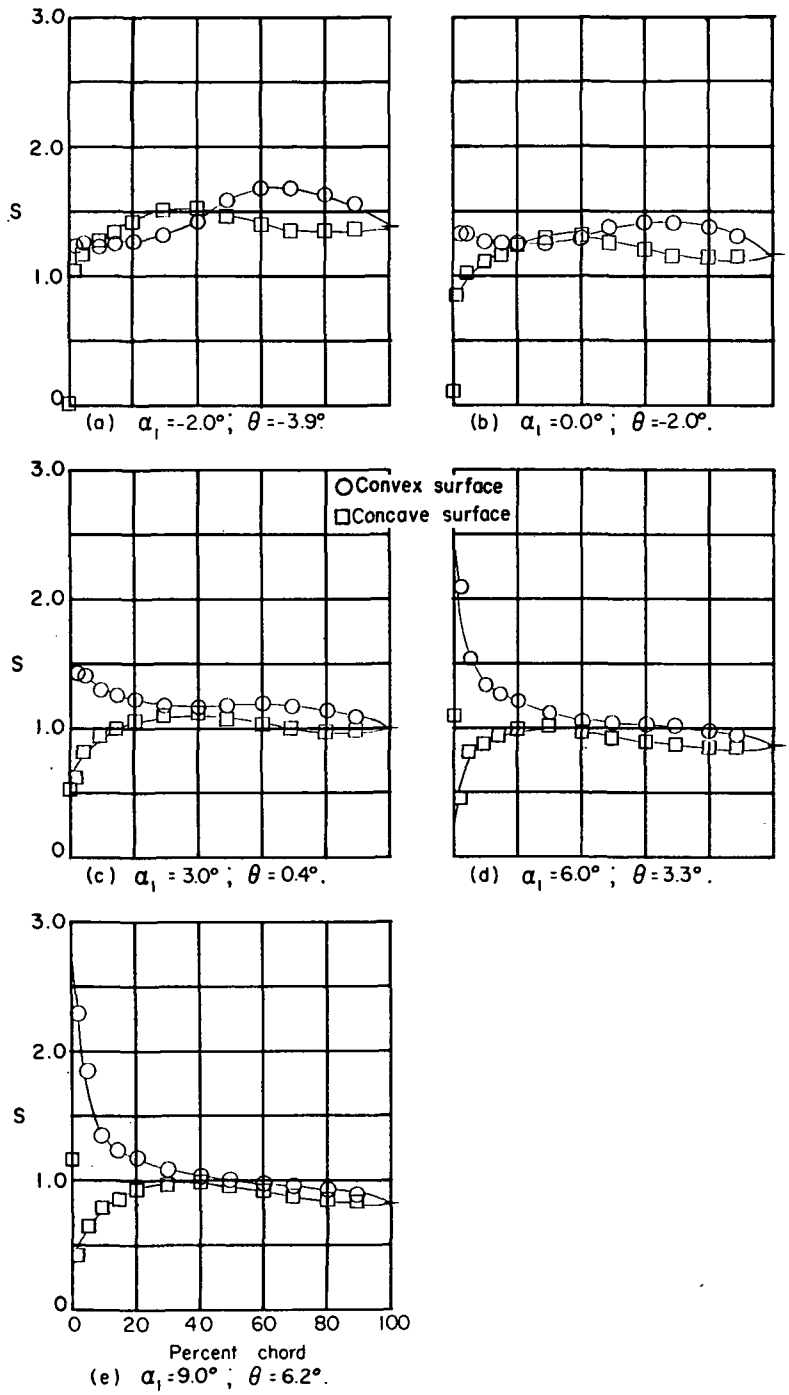

Figure 10.- Blade-surface pressure distributions and section characteristics for the cascade combination $\beta = 60^{\circ}$, $\sigma = 2.00$, and blade section NACA 65-(0)06.

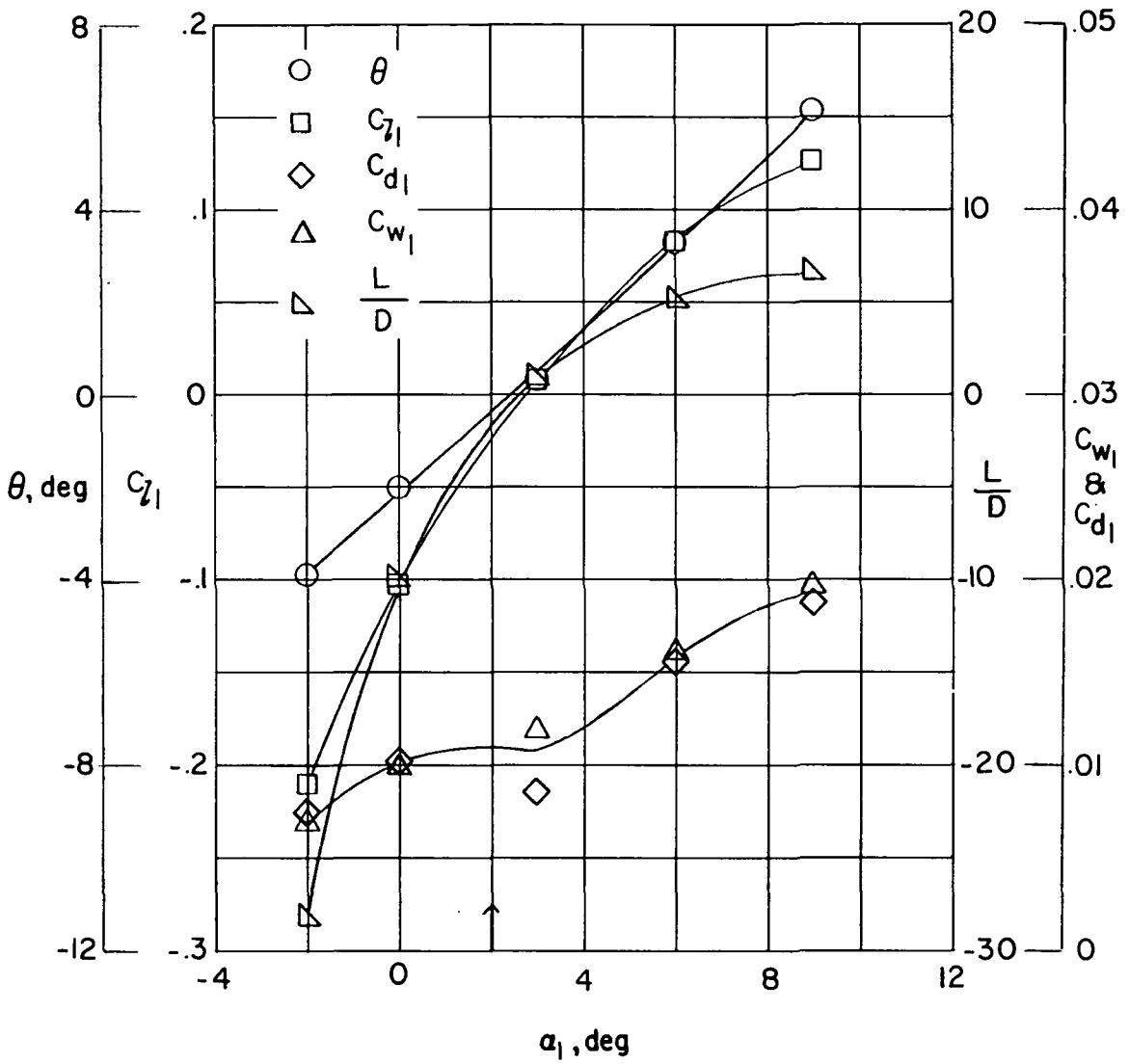

(f) Section characteristics. NACA 65-(0)06; $\beta = 60^\circ$; $\sigma = 2.00$; $R = 346{,}000$. Arrow shows α_d.

Figure 10.- Concluded.

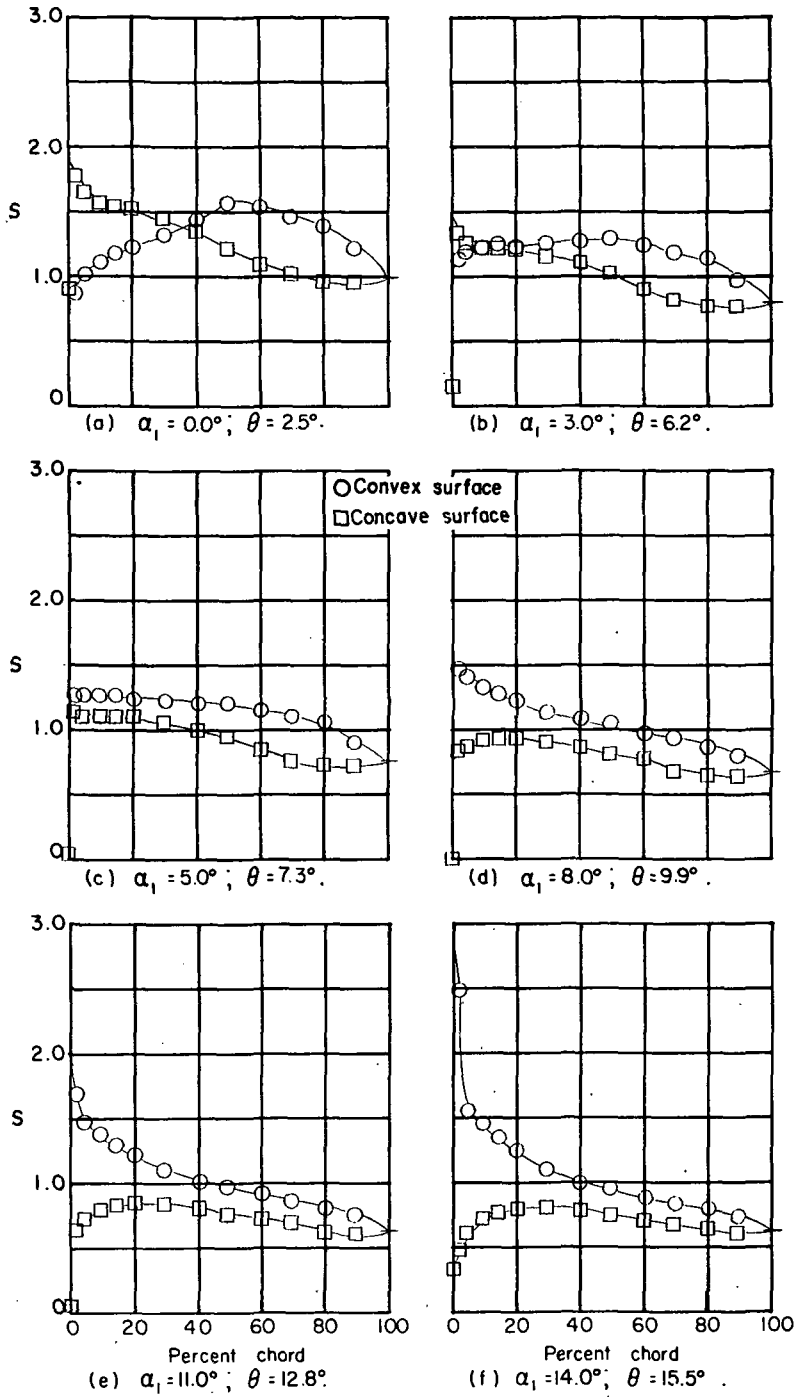

Figure 11.- Blade-surface pressure distributions and section characteristics for the cascade combination $\beta = 60°$, $\sigma = 2.00$, and blade section NACA 65-$\left(^{4}A_{10}\right)$06.

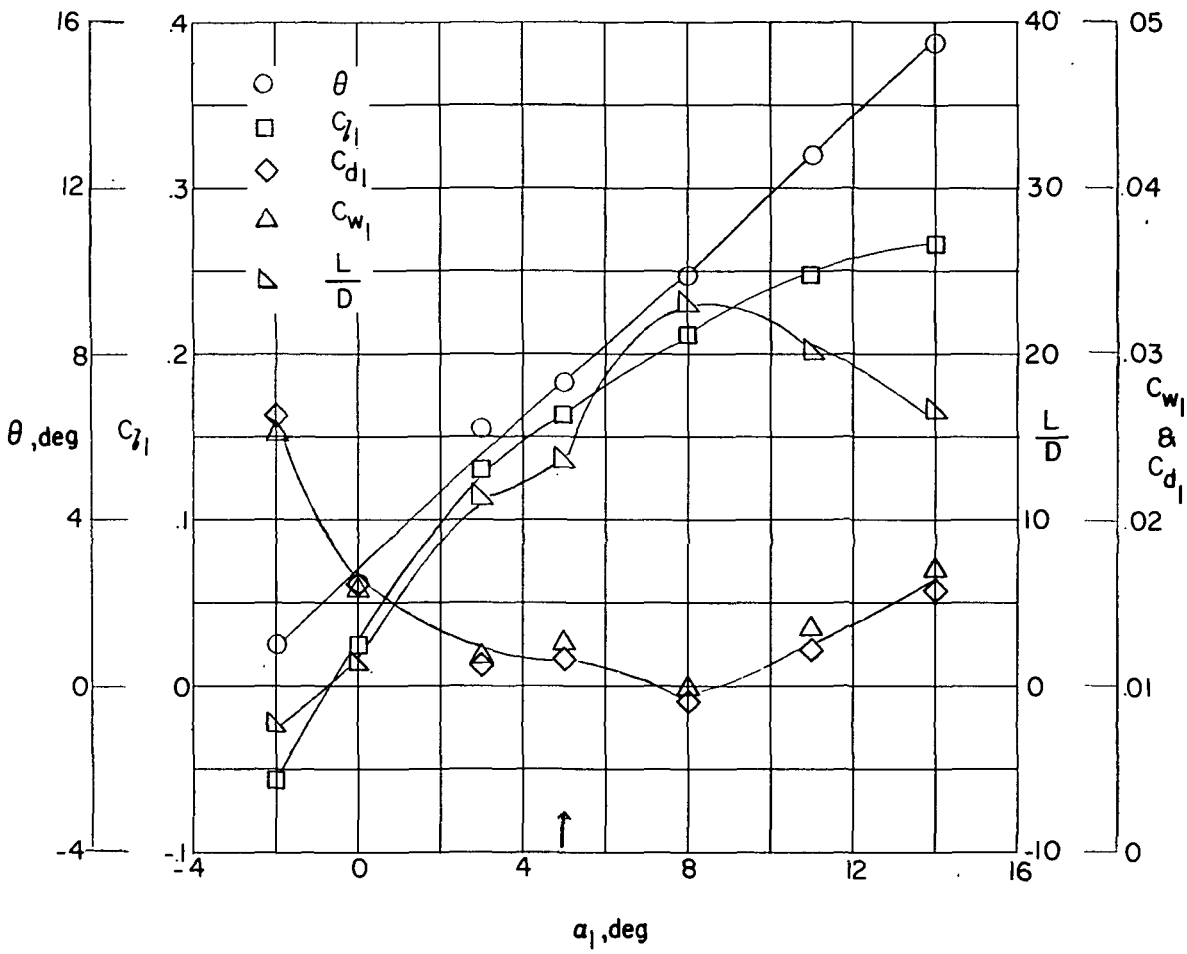

(g) Section characteristics. NACA 65-$(4A_{10})$06; $\beta = 60°$; $\sigma = 2.00$; $R = 346{,}000$. Arrow shows α_d.

Figure 11.- Concluded.

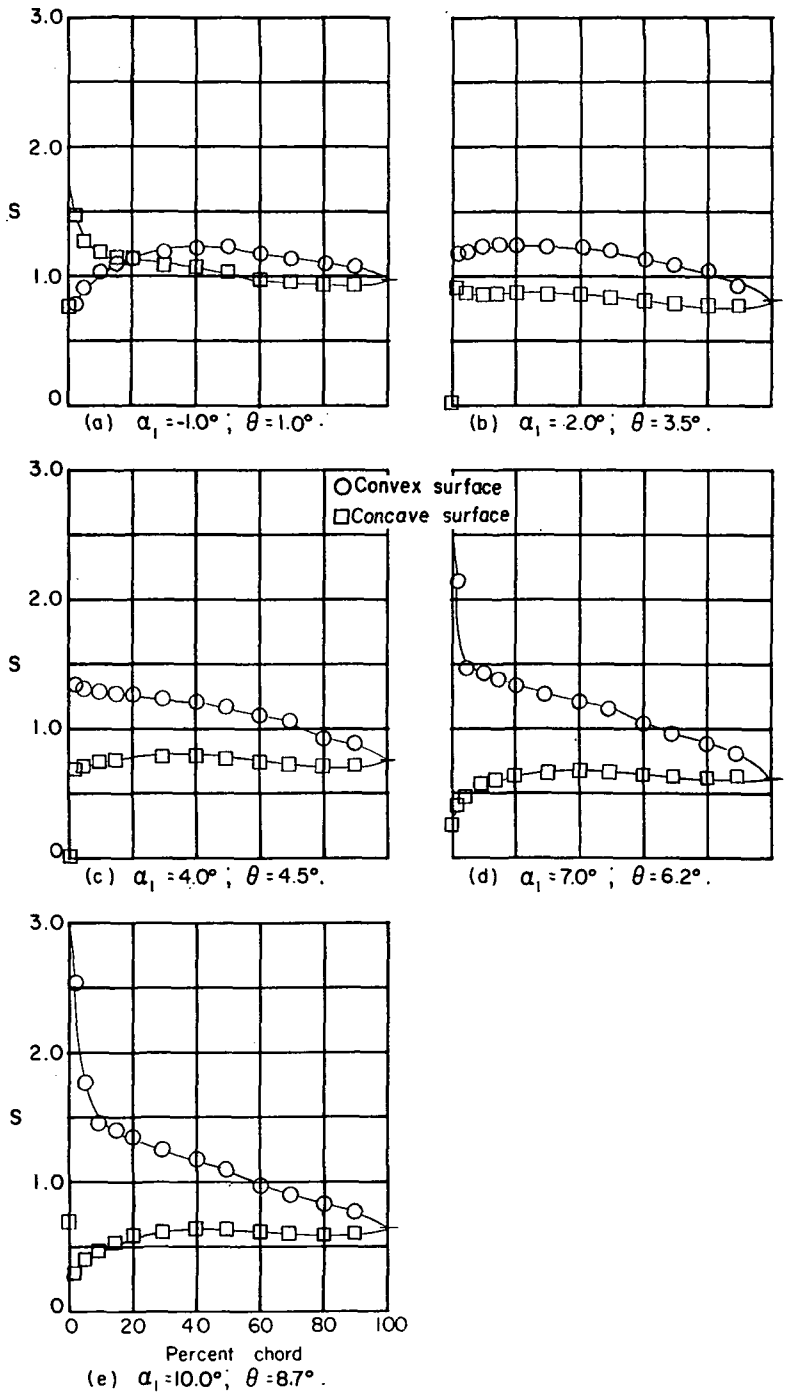

Figure 12.- Blade-surface pressure distributions and section characteristics for the cascade combination $\beta = 70^{\circ}$, $\sigma = 0.75$, and blade section NACA 65-$(4A_{10})$06.

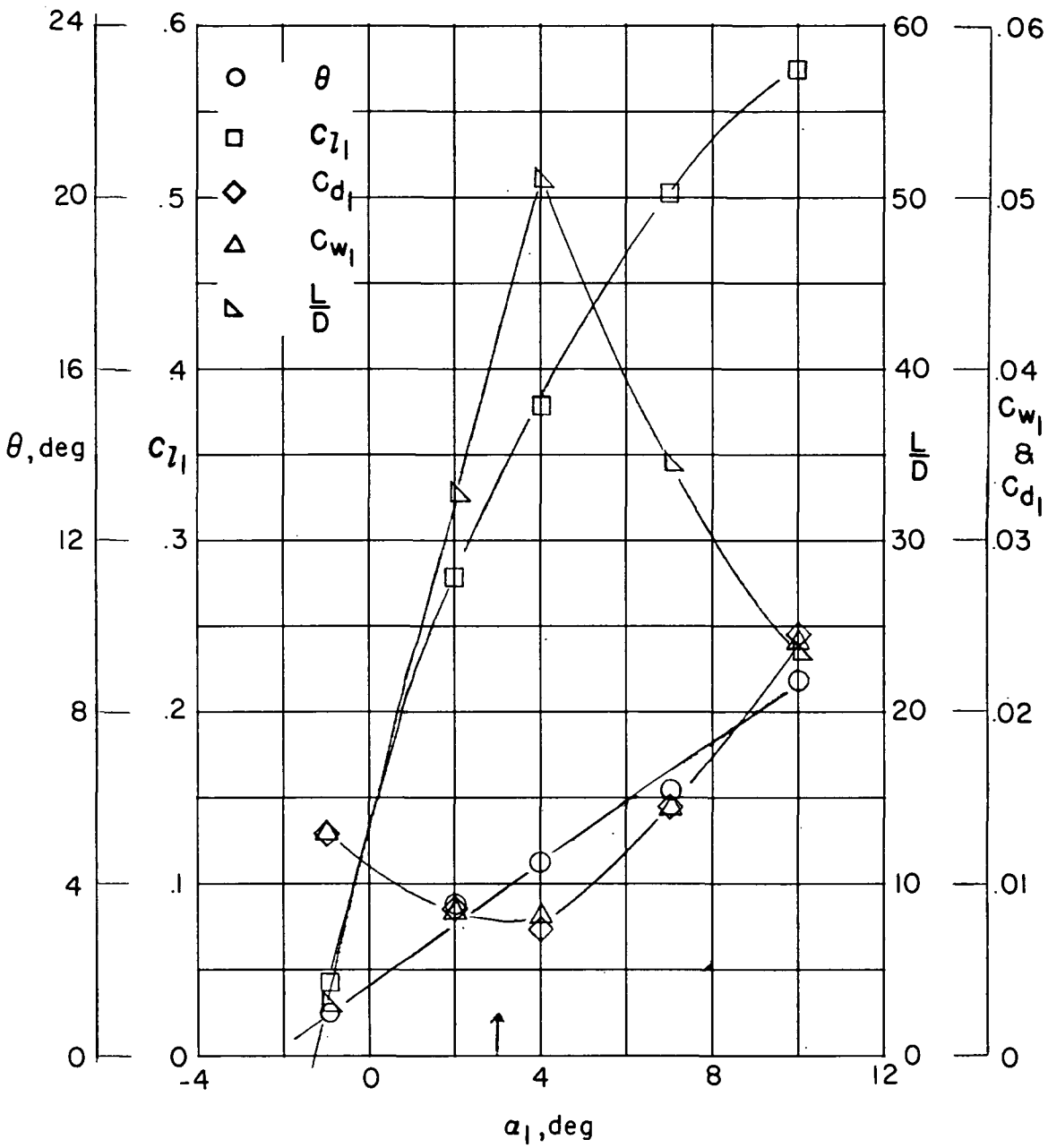

(f) Section characteristics. NACA 65-$(4A_{10})$06; $\beta = 70^\circ$; $\sigma = 0.75$; R = 346,000. Arrow shows α_d.

Figure 12.- Concluded.

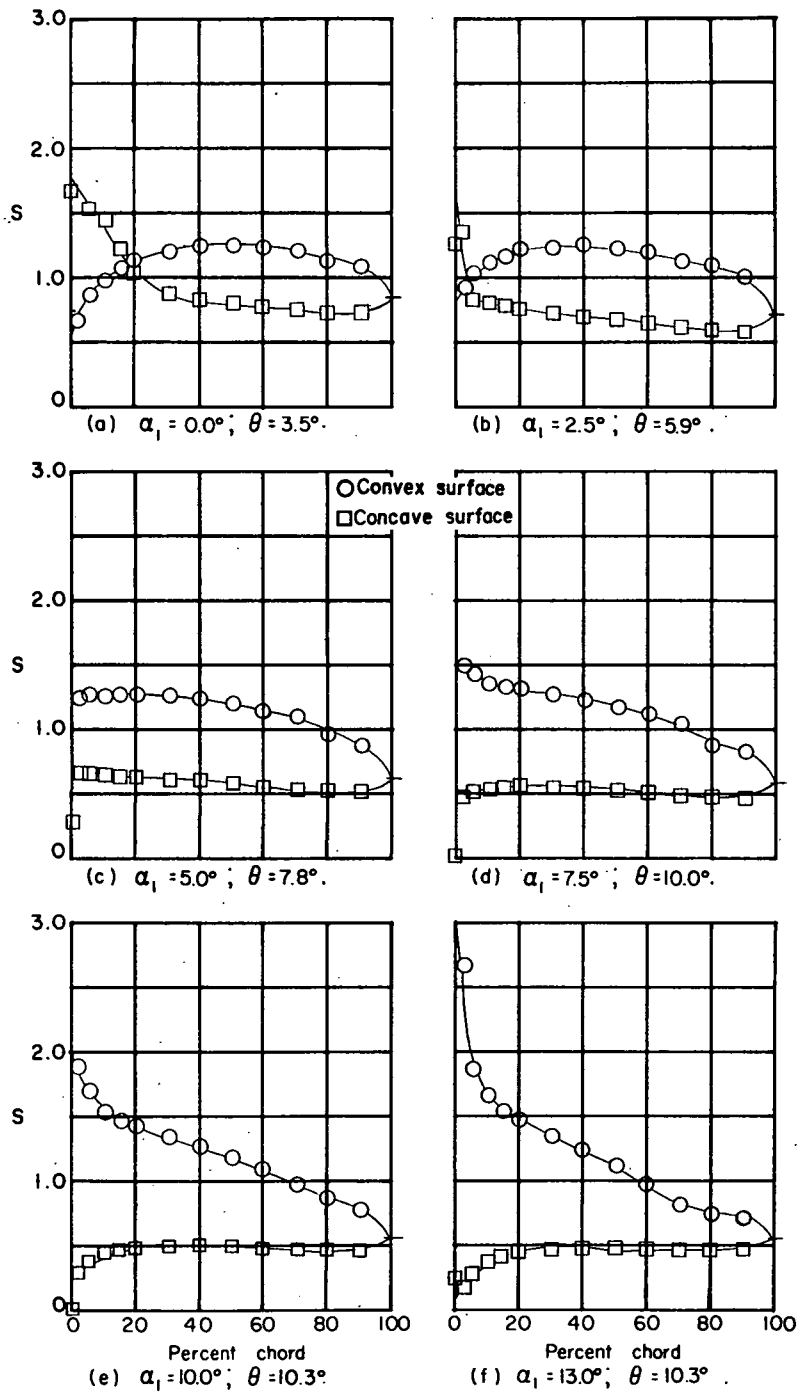

Figure 13.- Blade-surface pressure distributions and section characteristics for the cascade combination $\beta = 70°$, $\sigma = 0.75$, and blade section NACA 65-$(8A_{10})$06.

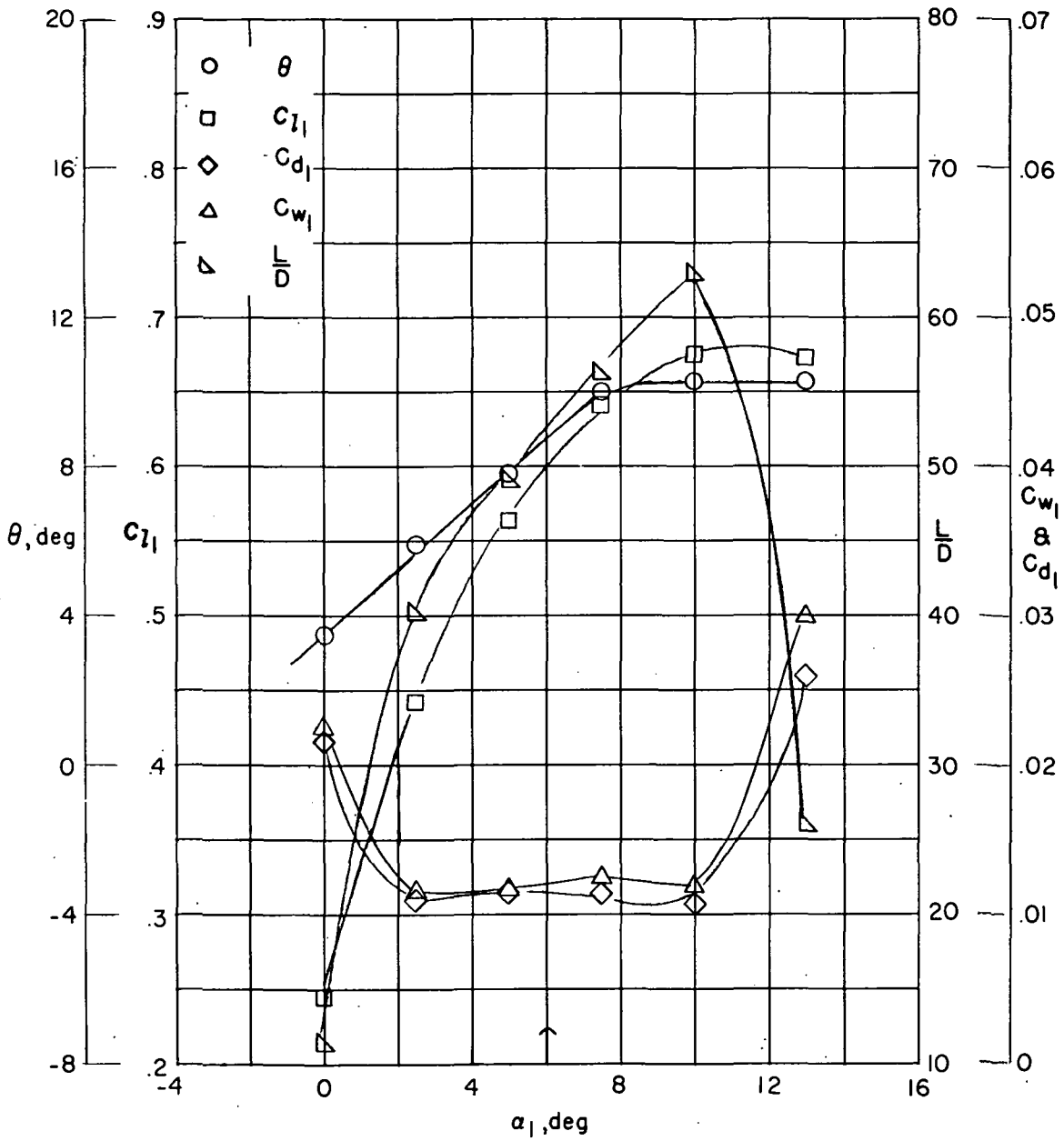

(g) Section characteristics. NACA 65-$(8A_{10})$06; β = 70°; σ = 0.75; R = 346,000. Arrow shows α_d.

Figure 13.- Concluded.

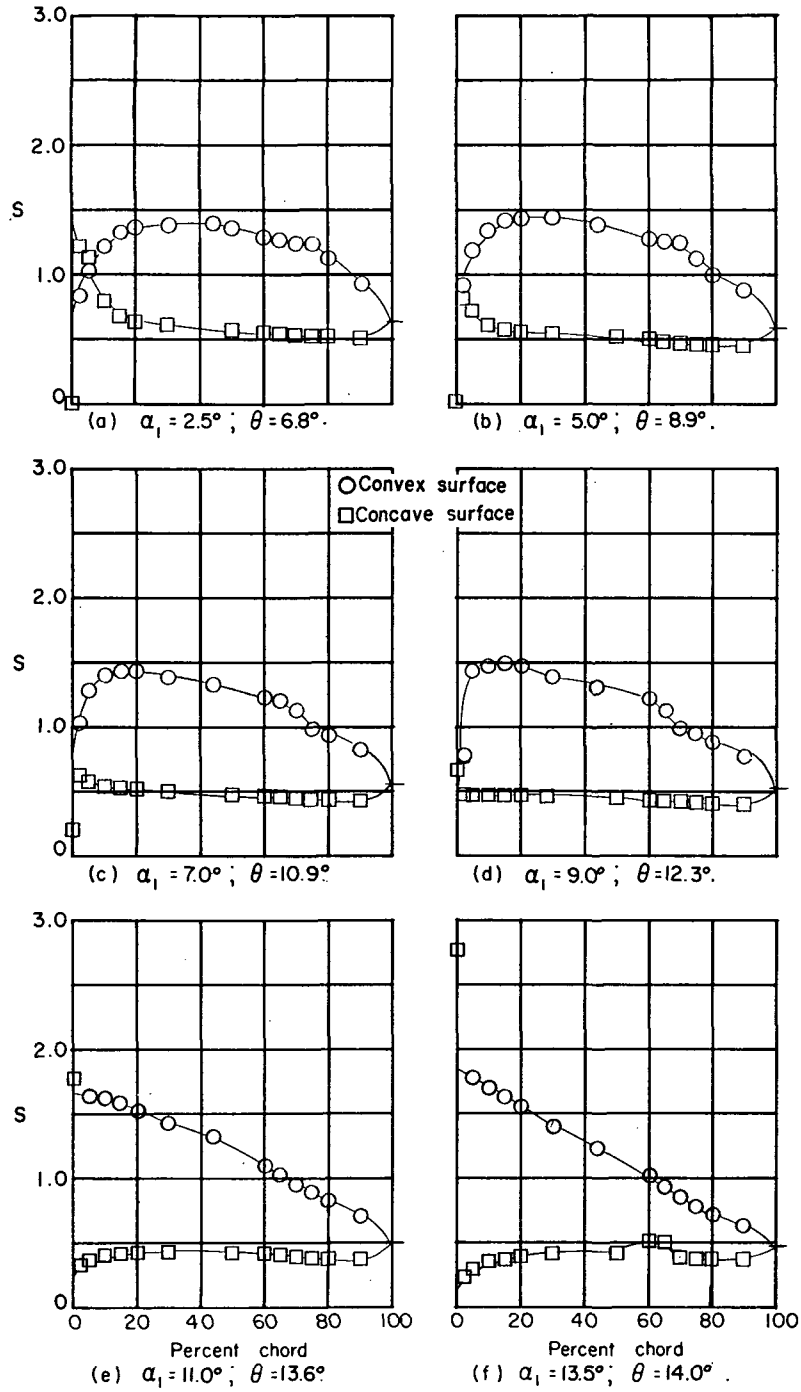

Figure 14.- Blade-surface pressure distributions and section characteristics for the cascade combination $\beta = 70°$, $\sigma = 0.75$, and blade section NACA 65-$(12A_{10})$06.

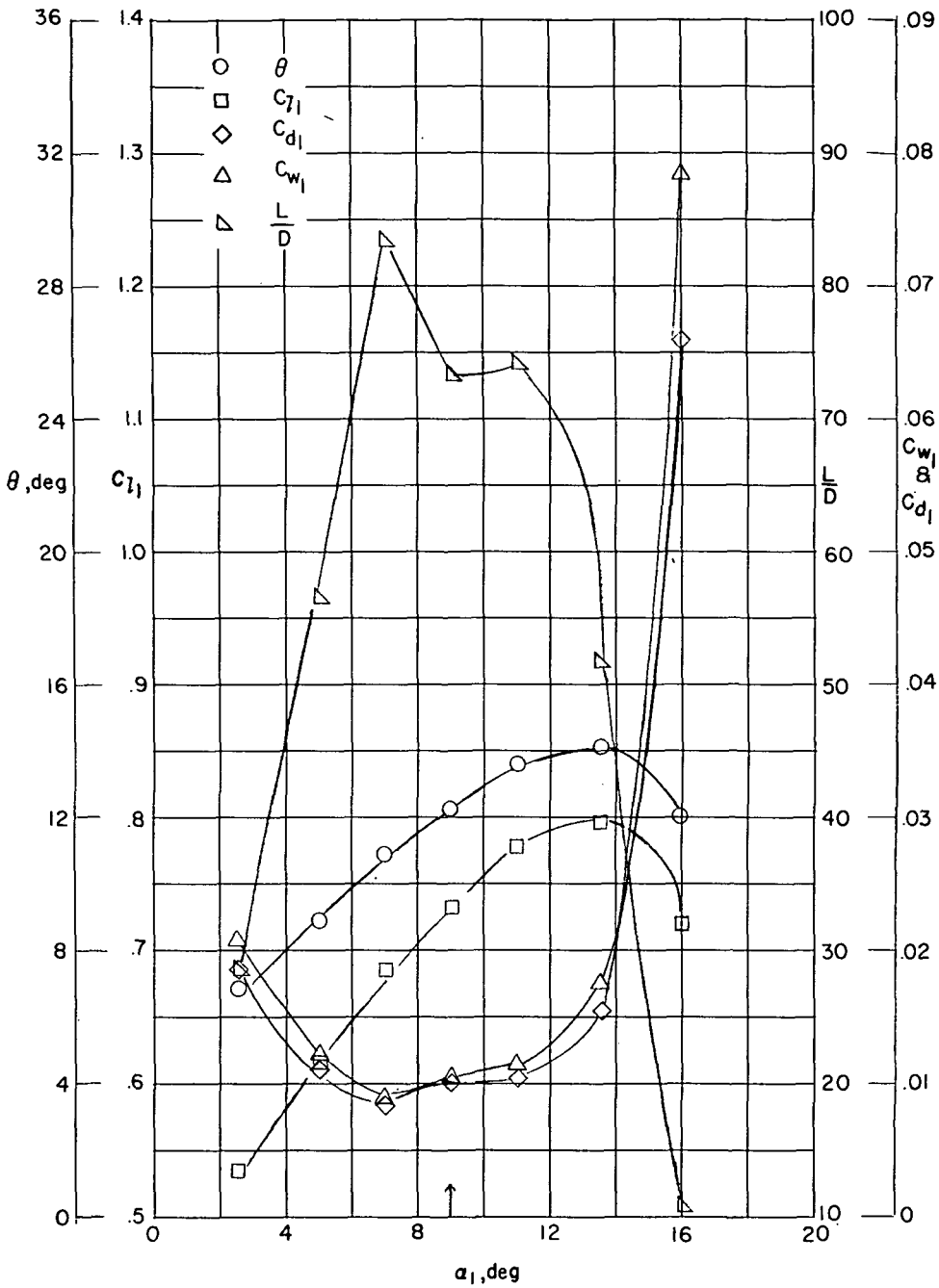

(g) Section characteristics. NACA 65-$(12A_{10})$06; $\beta = 70^{\circ}$; $\sigma = 0.75$; $R = 346{,}000$. Arrow shows α_d.

Figure 14.- Concluded.

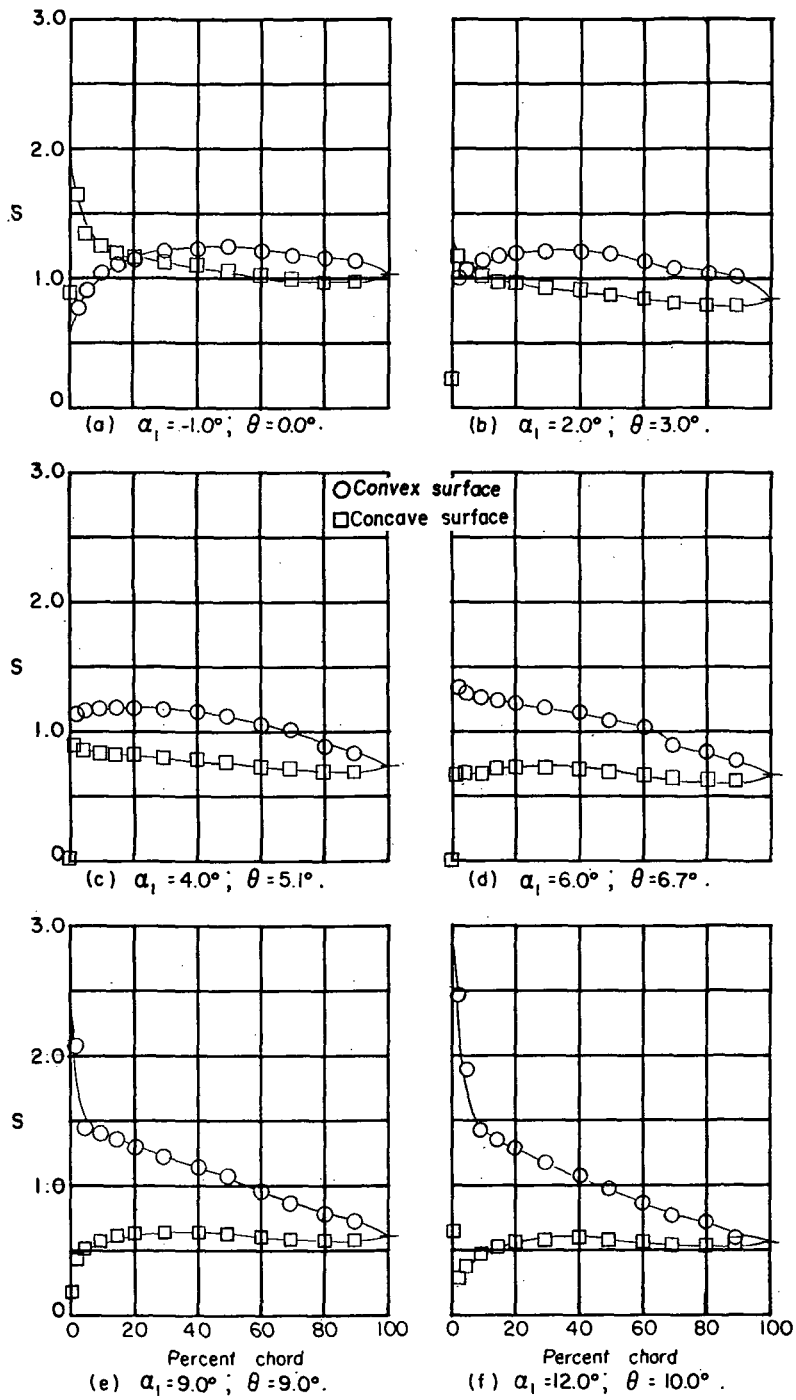

Figure 15.- Blade-surface pressure distributions and section characteristics for the cascade combination $\beta = 70°$, $\sigma = 1.00$, and blade section NACA 65-$(4A_{10})$06.

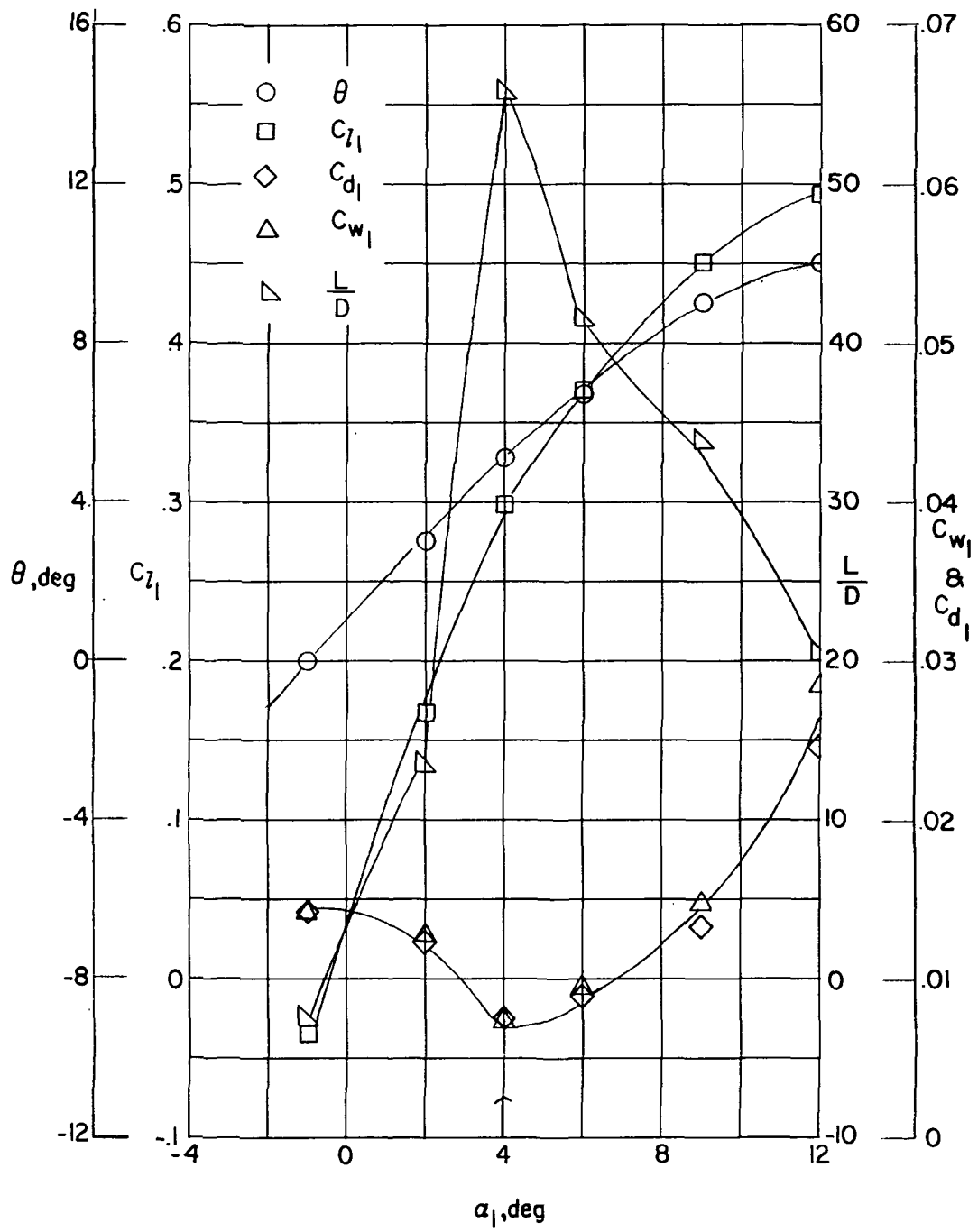

(g) Section characteristics. NACA 65-$(4A_{10})$06; β = 70°; σ = 1.00; R = 346,000. Arrow shows α_d.

Figure 15.- Concluded.

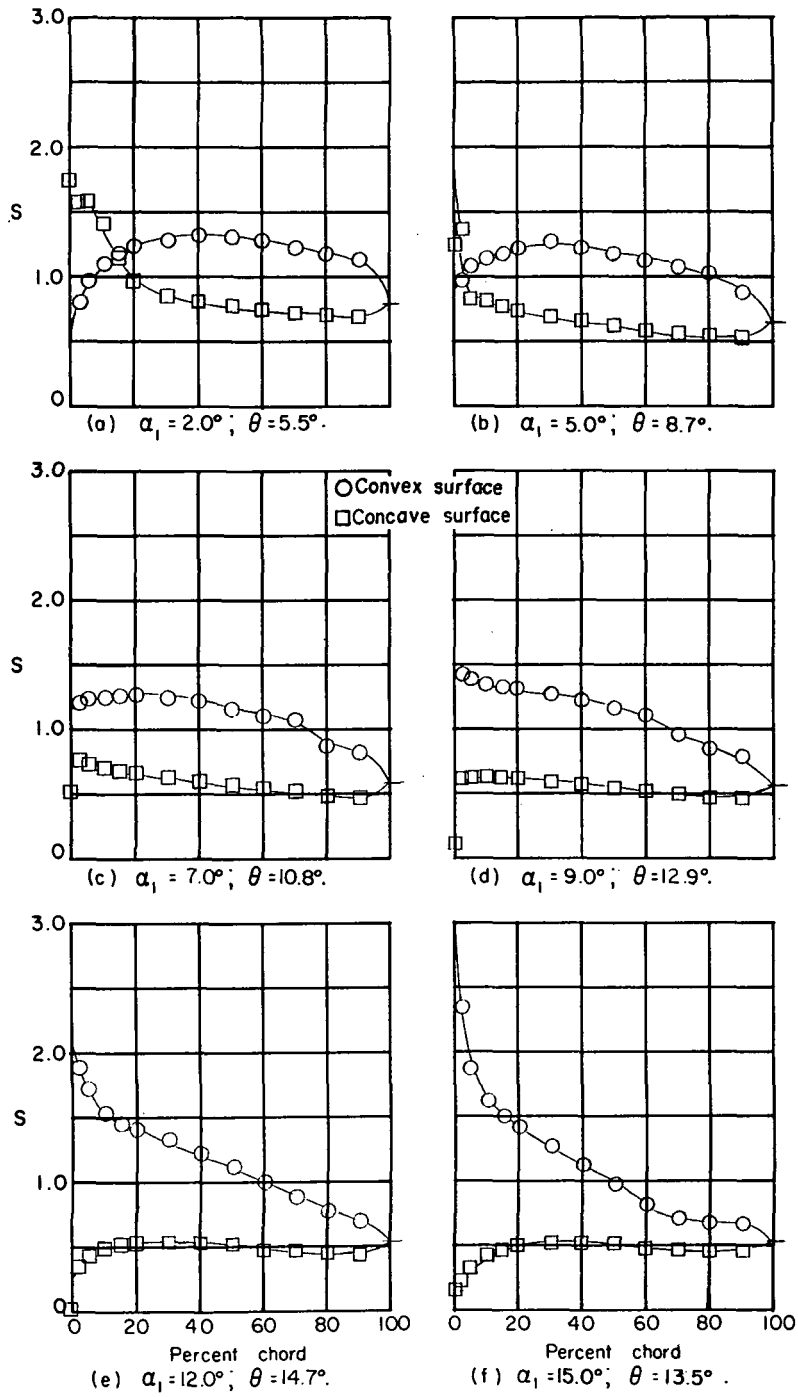

Figure 16.- Blade-surface pressure distributions and section characteristics for the cascade combination $\beta = 70°$, $\sigma = 1.00$, and blade section NACA 65-$(8A_{10})$06.

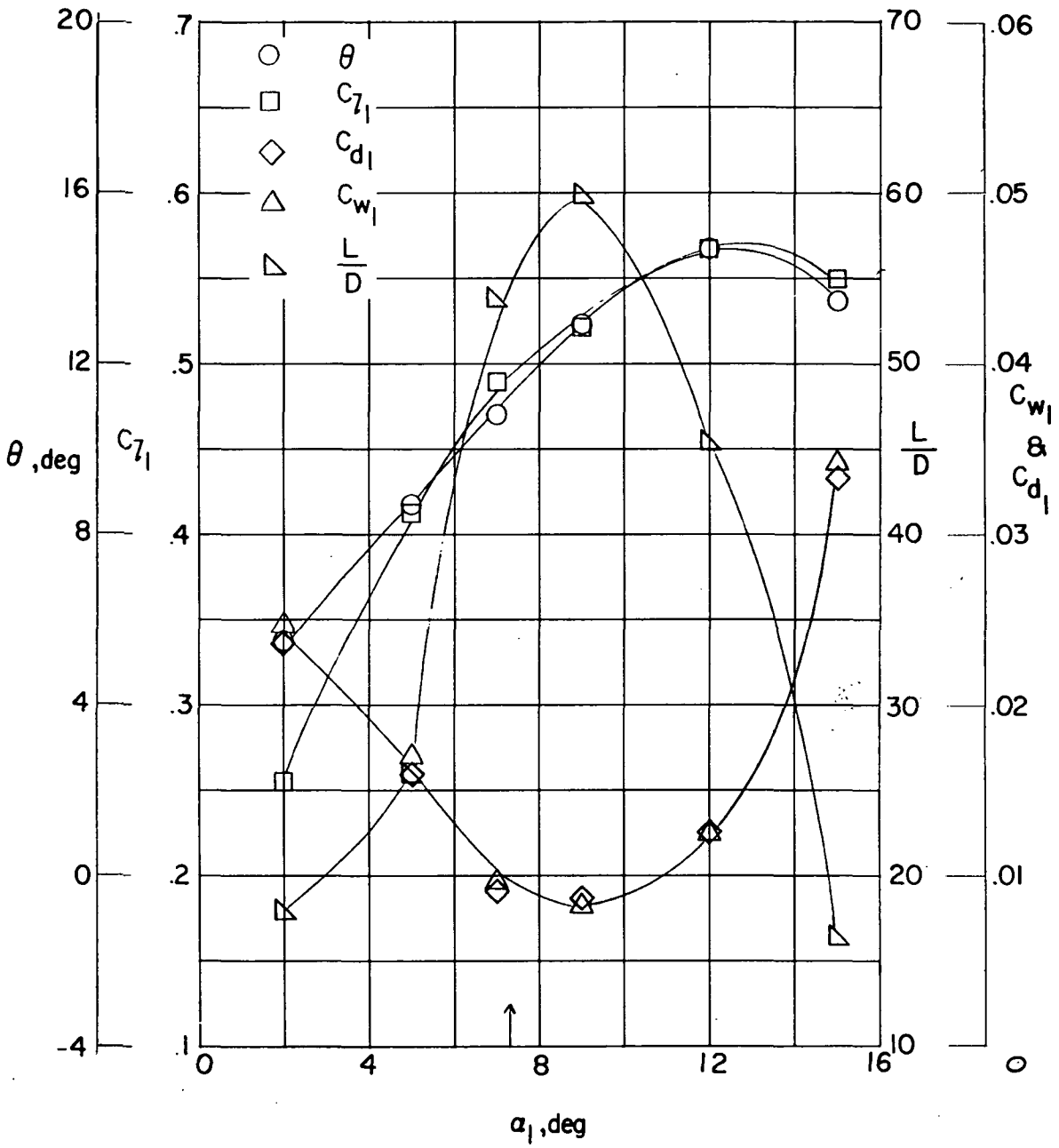

(g) Section characteristics. NACA 65-$(8A_{10})$06; β = 70°; σ = 1.00; R = 346,000. Arrow shows α_d.

Figure 16.- Concluded.

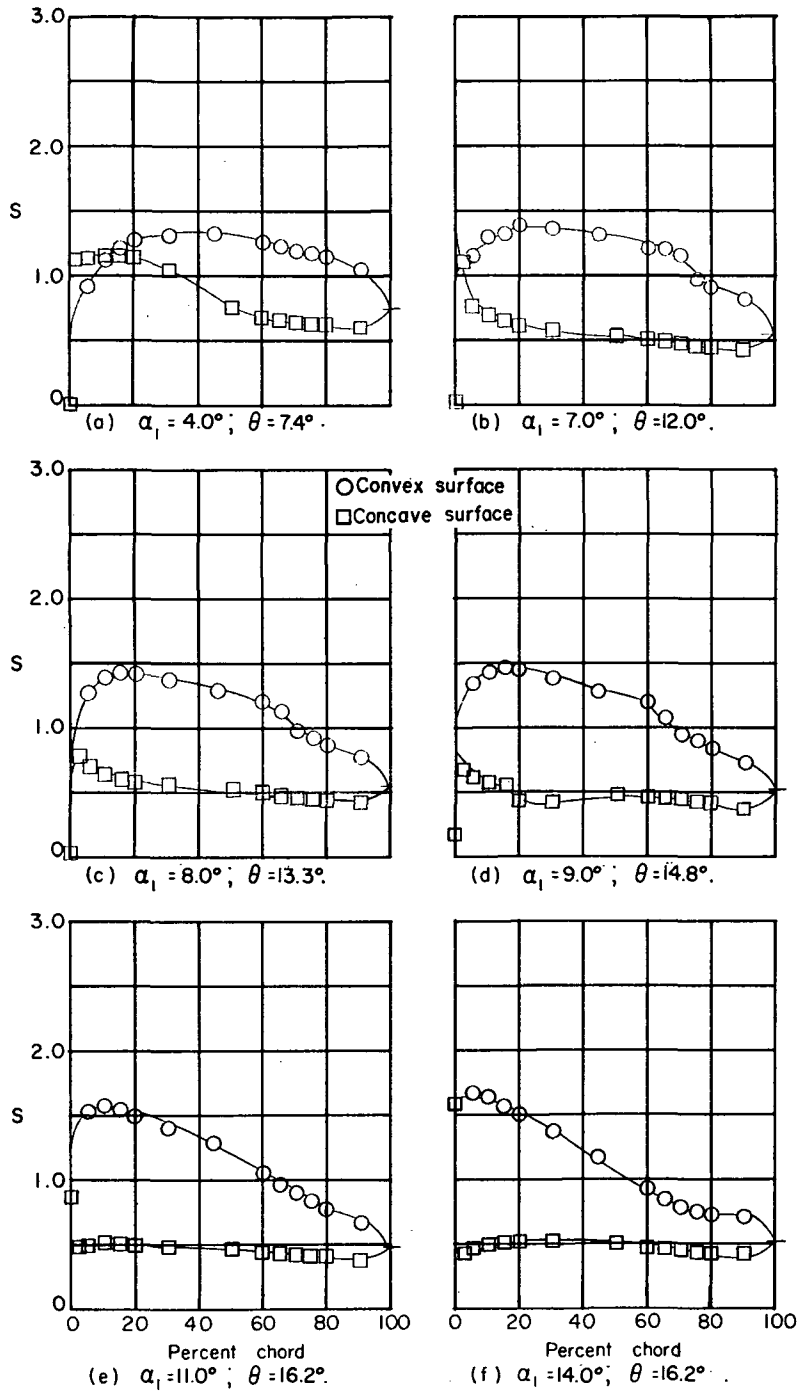

Figure 17.- Blade-surface pressure distributions and section characteristics for the cascade combination $\beta = 70°$, $\sigma = 1.00$, and blade section NACA 65-$(12A_{10})$06.

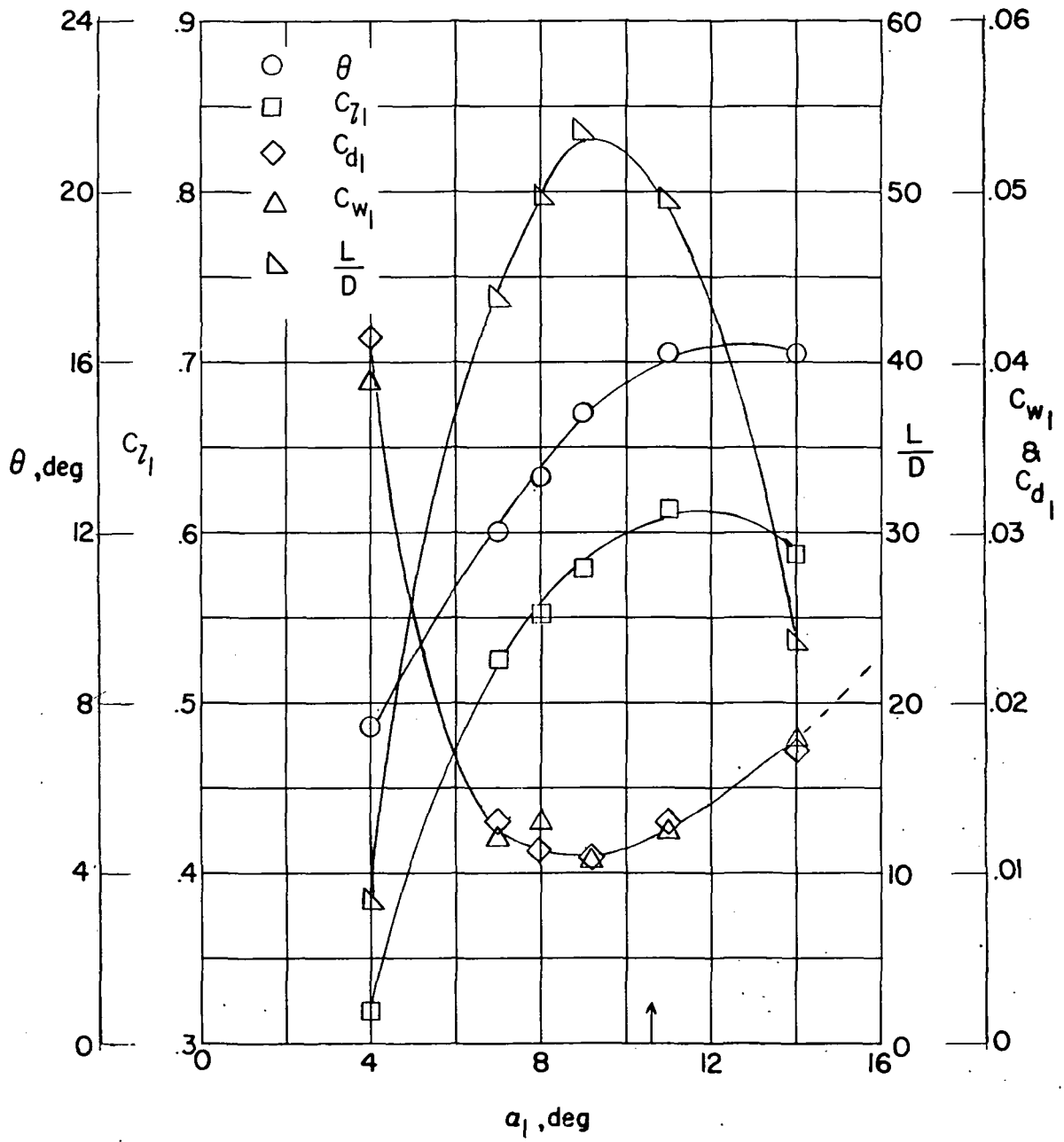

(g) Section characteristics. NACA 65-$(12A_{10})$06; β = 70°; σ = 1.00; R = 346,000. Arrow shows α_d.

Figure 17.- Concluded.

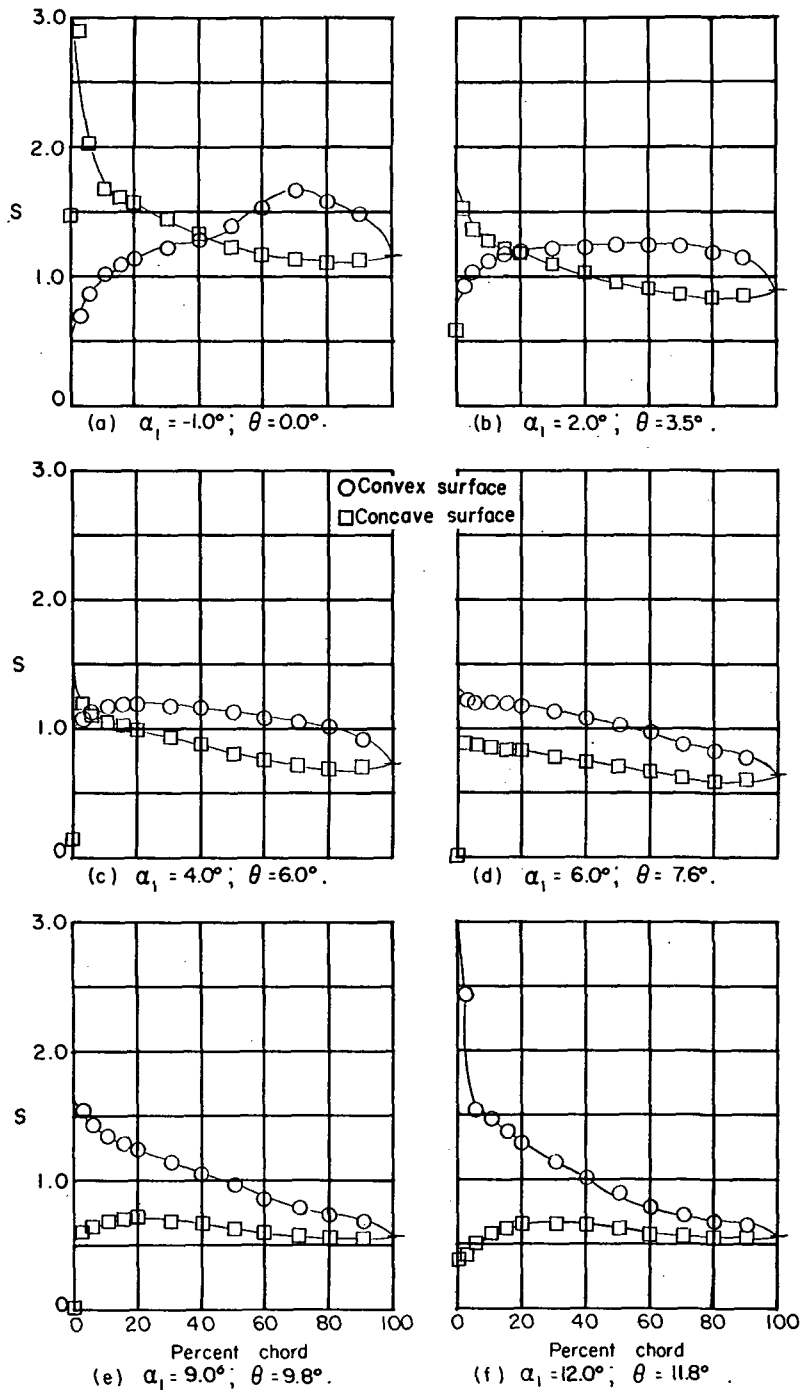

Figure 18.- Blade-surface pressure distributions and section characteristics for the cascade combination $\beta = 70^\circ$, $\sigma = 1.50$, and blade section NACA 65-$(4A_{10})$06.

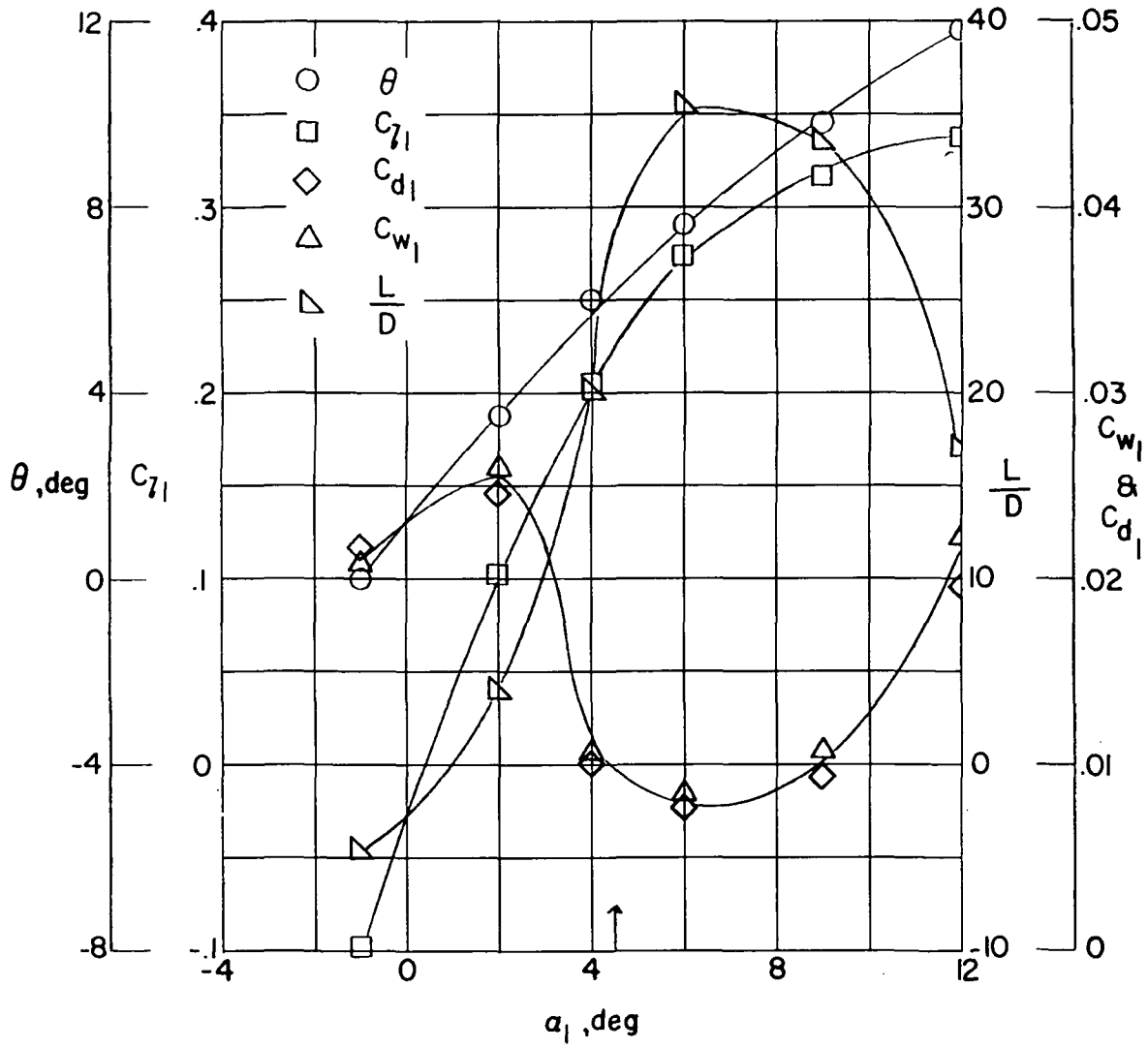

(g) Section characteristics. NACA 65-$\left(4A_{10}\right)$06; β = 70°; σ = 1.50; R = 346,000. Arrow shows α_d.

Figure 18.- Concluded.

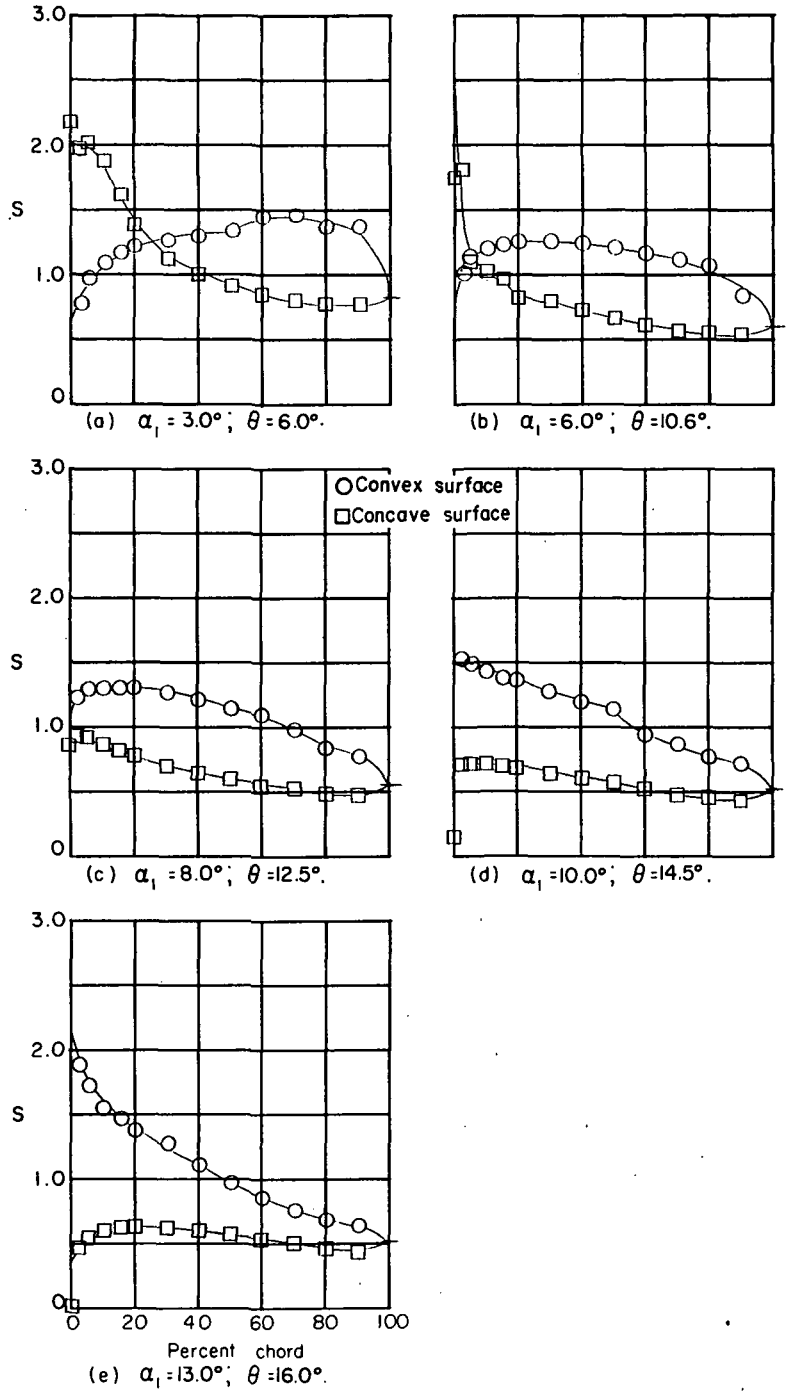

Figure 19.- Blade-surface pressure distributions and section characteristics for the cascade combination $\beta = 70°$, $\sigma = 1.50$, and blade section NACA 65-$(8A_{10})$06.

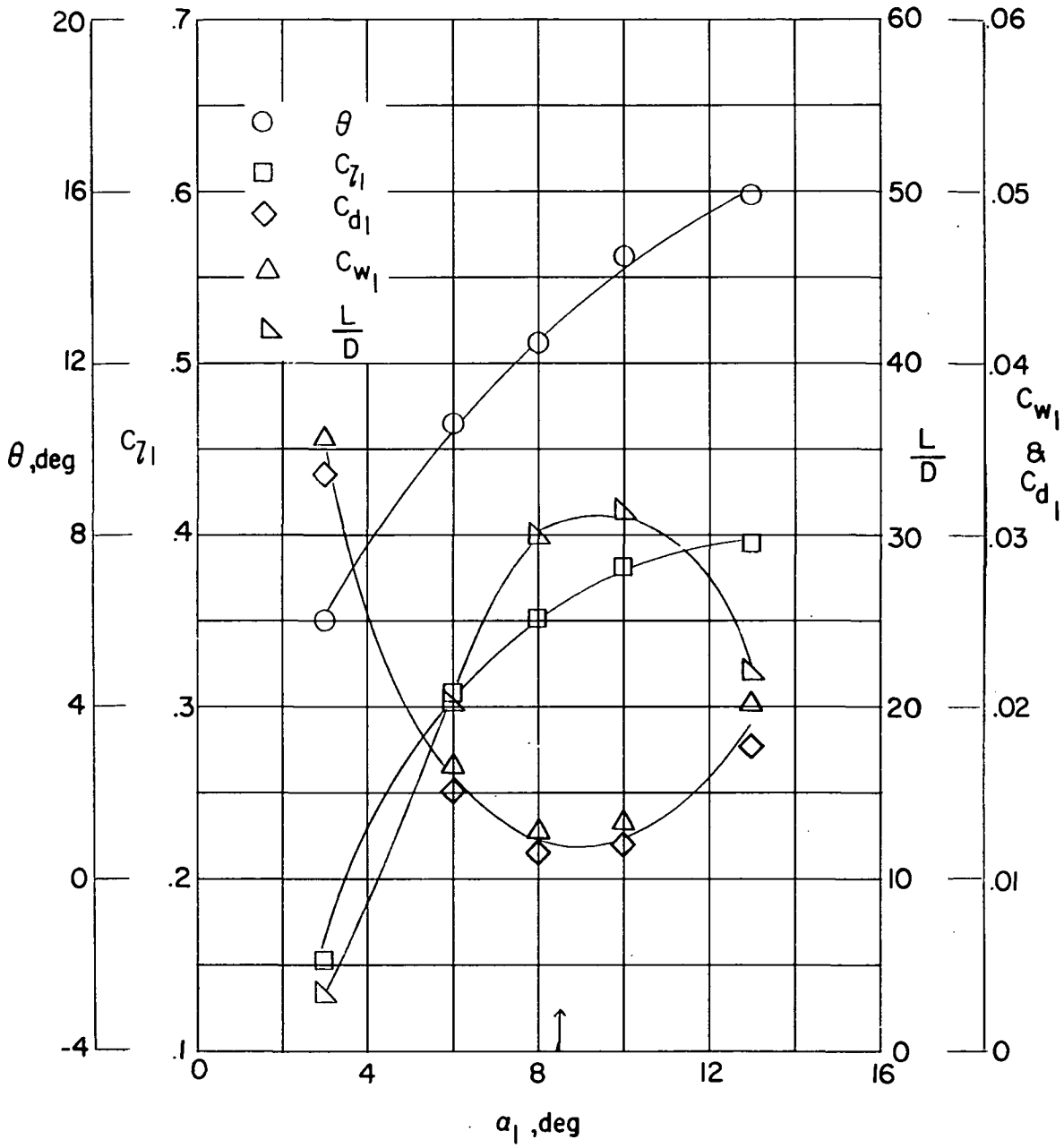

(f) Section characteristics. NACA 65-$(8A_{10})$06; $\beta = 70^\circ$; $\sigma = 1.50$; $R = 346{,}000$. Arrow shows α_d.

Figure 19.- Concluded.

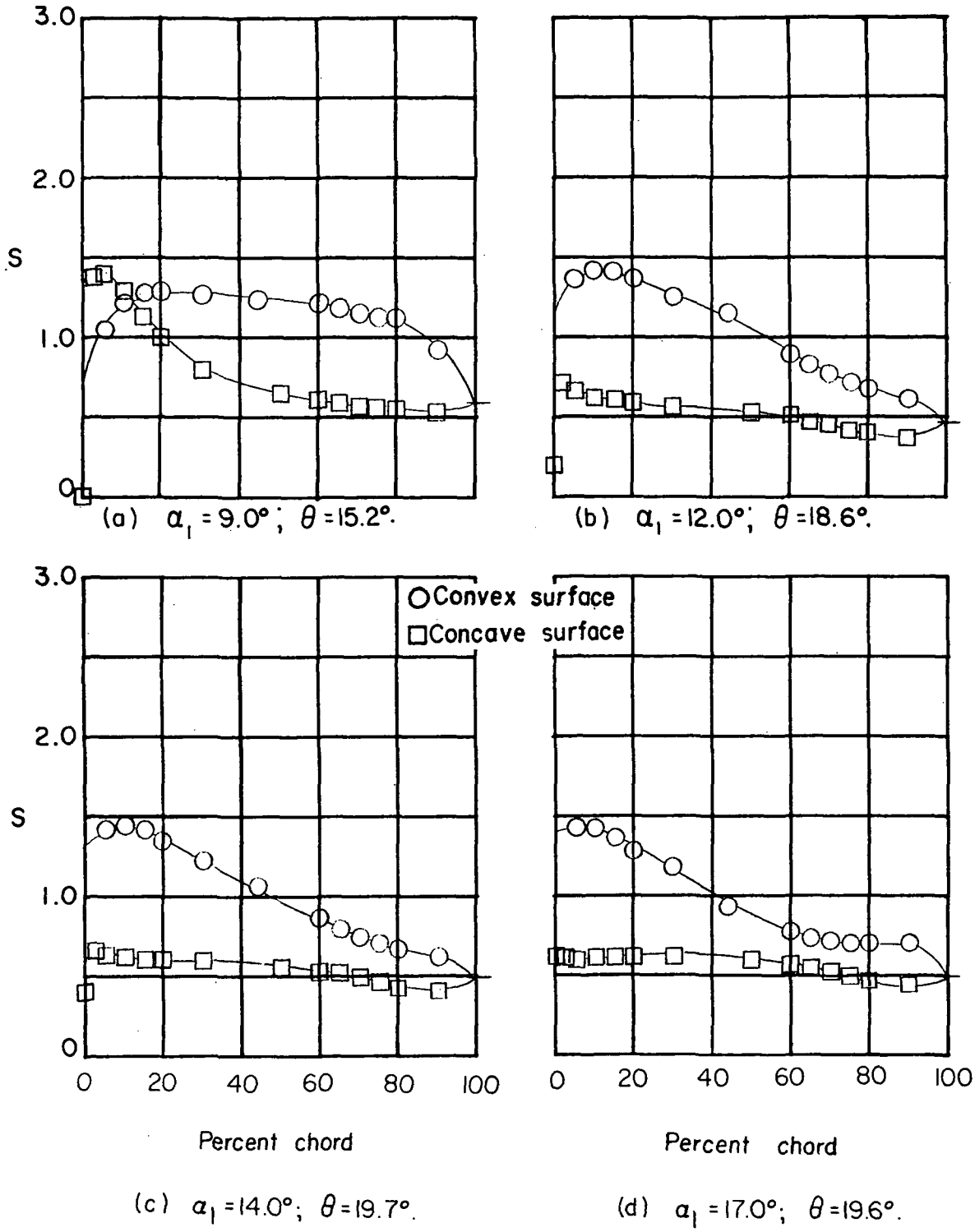

Figure 20.- Blade-surface pressure distributions and section characteristics for the cascade combination $\beta = 70°$, $\sigma = 1.50$, and blade section NACA 65-$(12A_{10})$06.

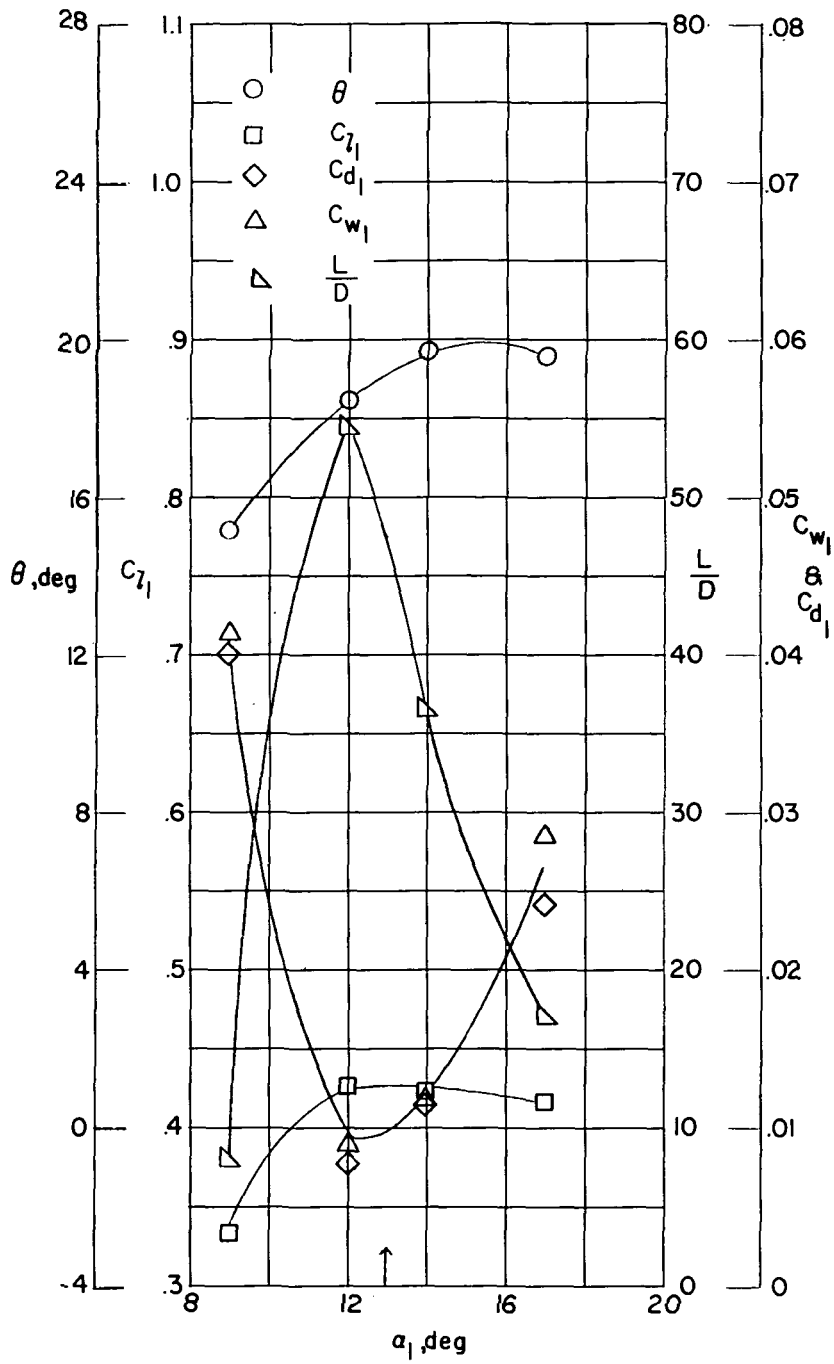

(e) Section characteristics. NACA 65-$(12A_{10})$06; $\beta = 70^\circ$; $\sigma = 1.50$; R = 346,000. Arrow shows α_d.

Figure 20.- Concluded.

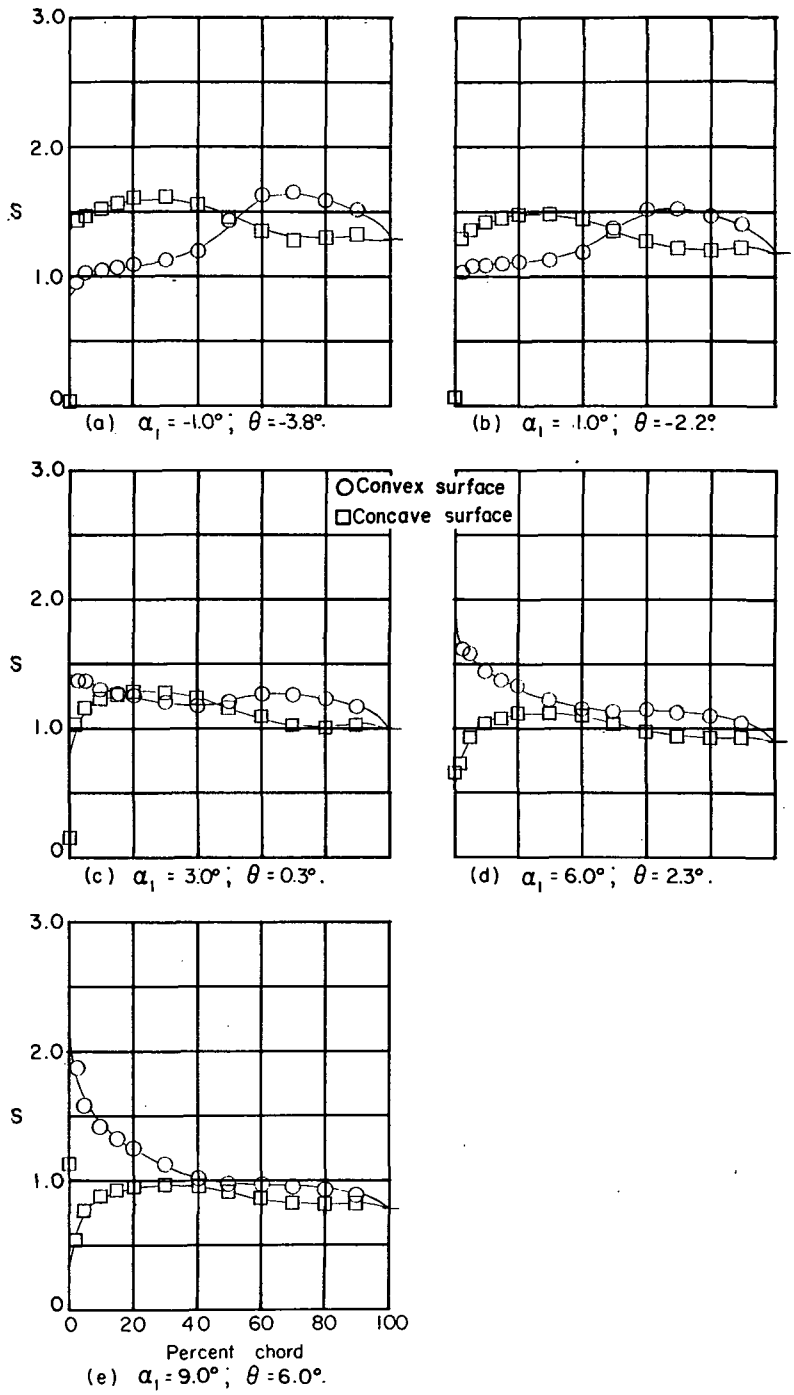

Figure 21.- Blade-surface pressure distributions and section characteristics for the cascade combination $\beta = 70°$, $\sigma = 2.00$, and blade section NACA 65-(0)06.

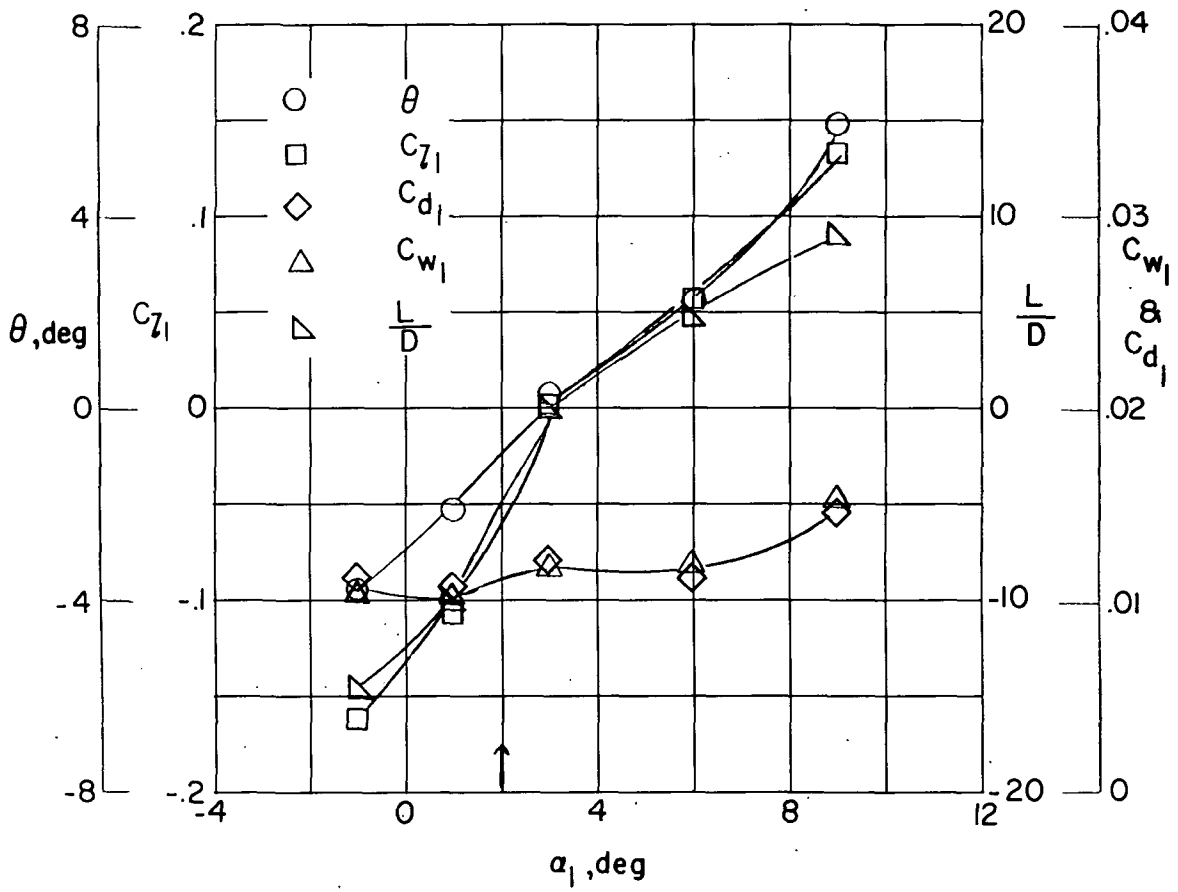

(f) Section characteristics. NACA 65-(0)06; $\beta = 70^\circ$; $\sigma = 2.00$; $R = 346{,}000$. Arrow shows α_d.

Figure 21.- Concluded.

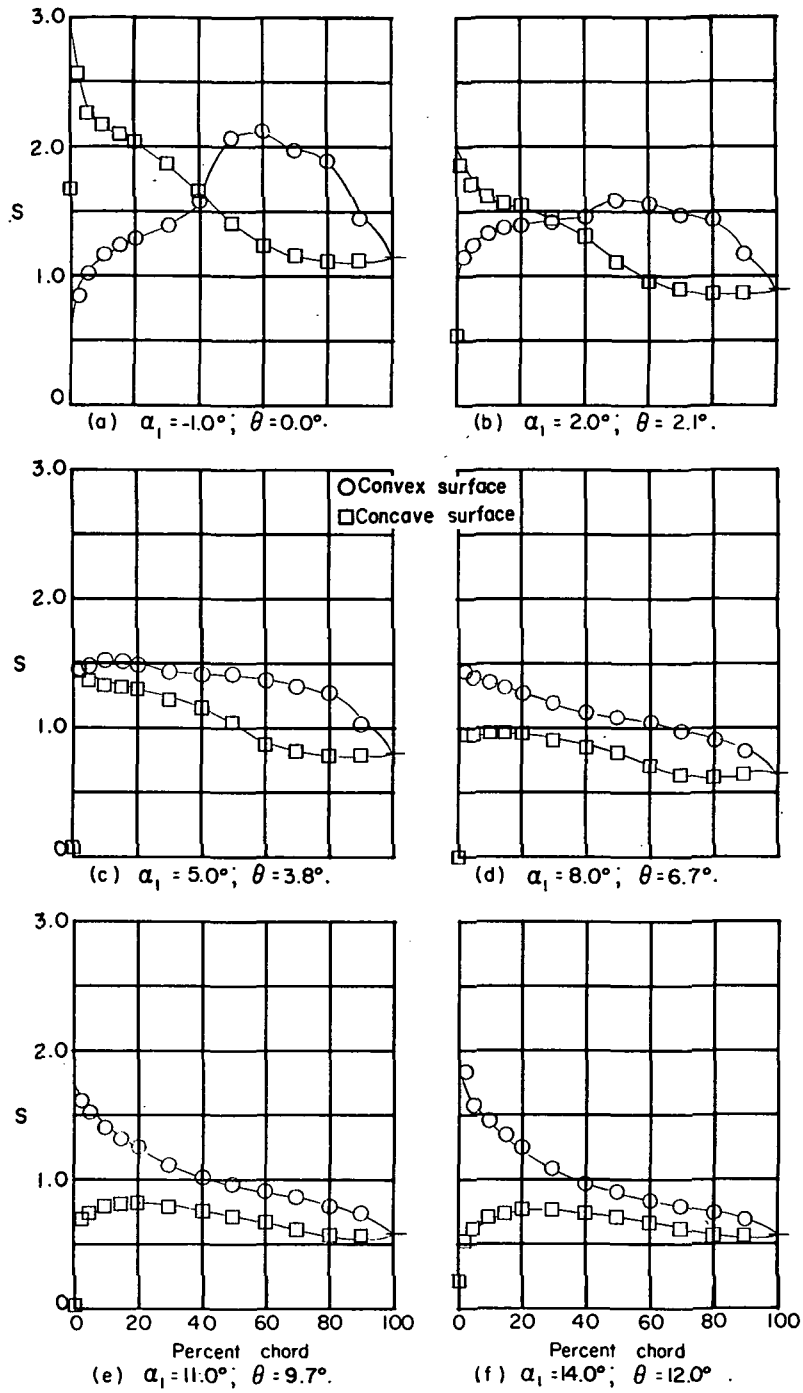

Figure 22.- Blade-surface pressure distributions and section characteristics for the cascade combination $\beta = 70°$, $\sigma = 2.00$, and blade section NACA 65-$\left(4A_{10}\right)$06.

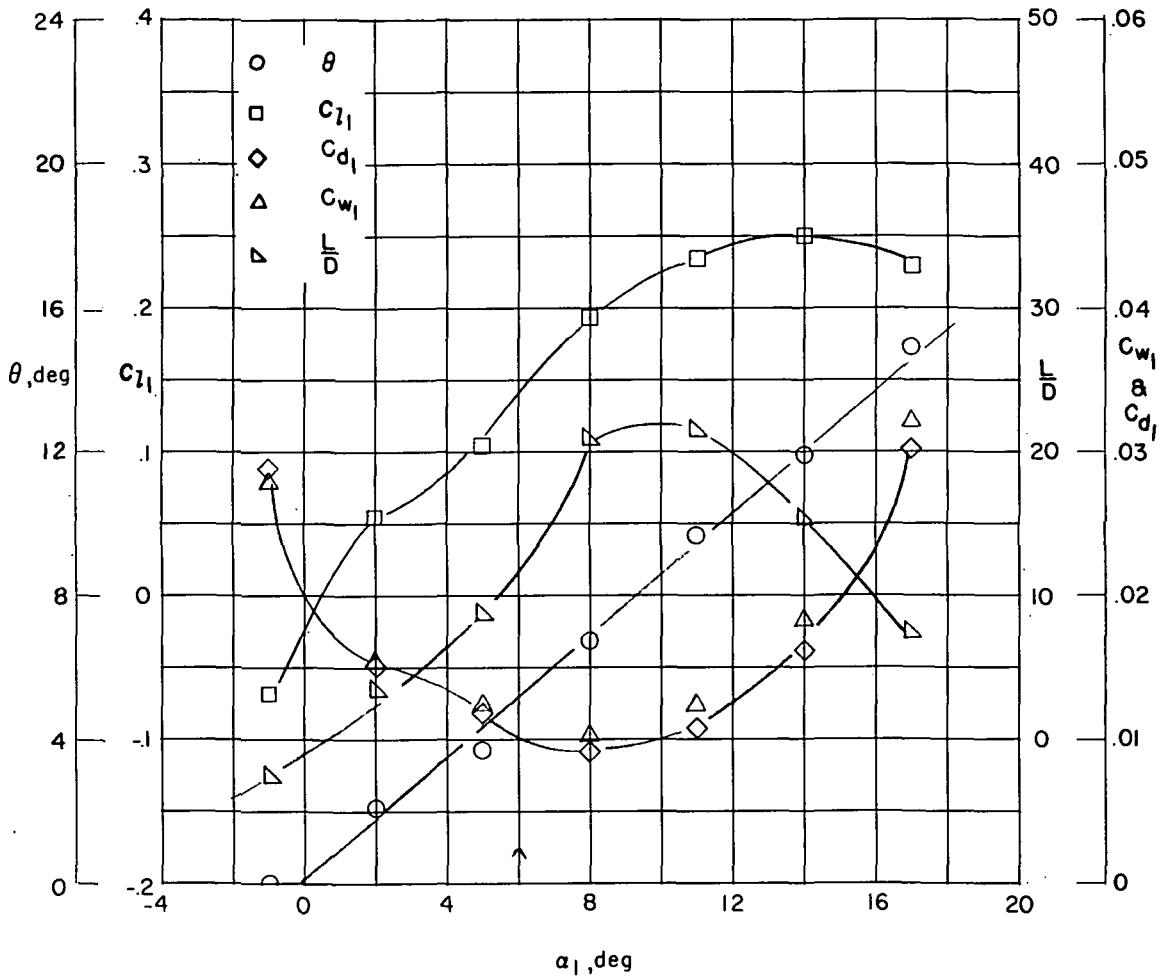

(g) Section characteristics. NACA 65-$(4A_{10})$06; β = 70°; σ = 2.00; R = 346,000. Arrow shows α_d.

Figure 22.- Concluded.

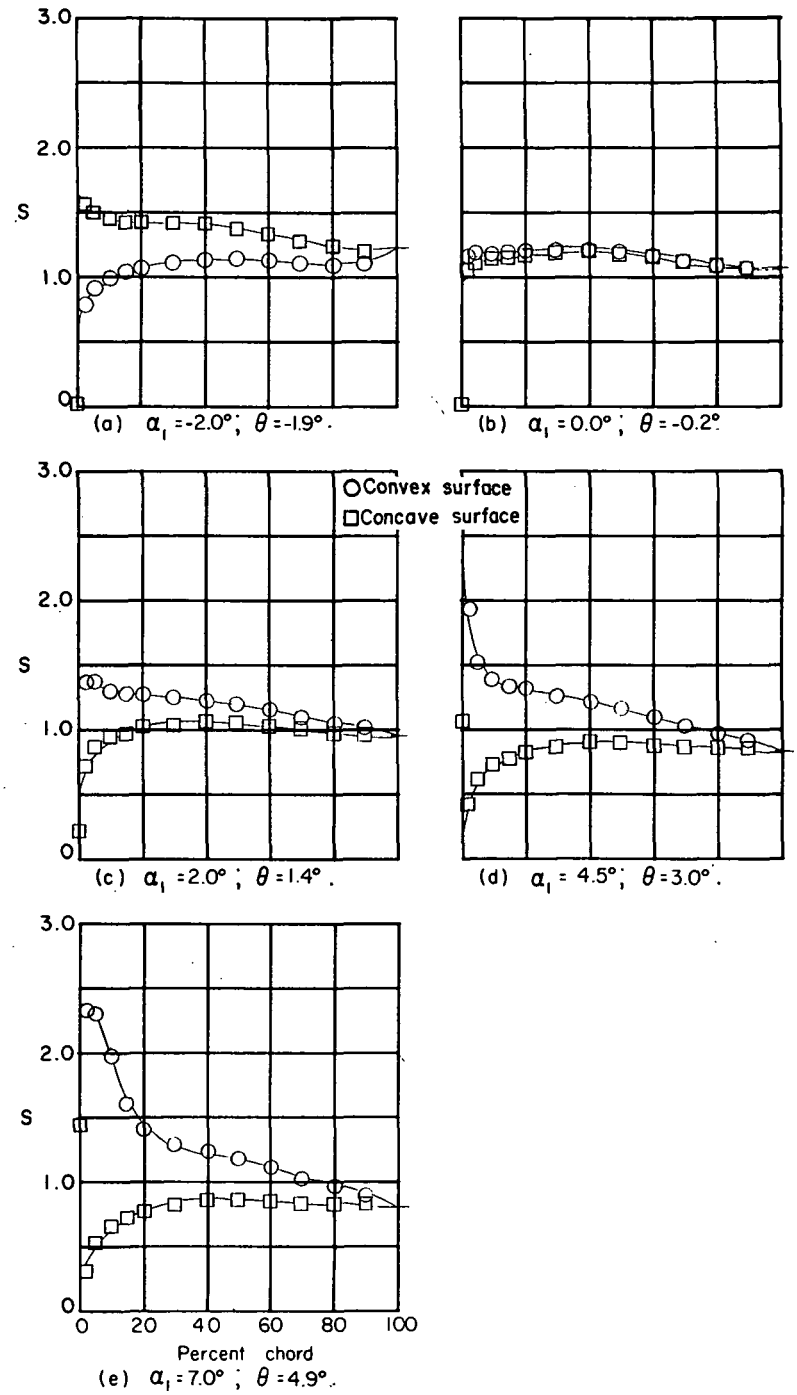

Figure 23.- Blade-surface pressure distributions and section characteristics for the cascade combination $\beta = 75^\circ$, $\sigma = 0.75$, and blade section NACA 65-(0)06.

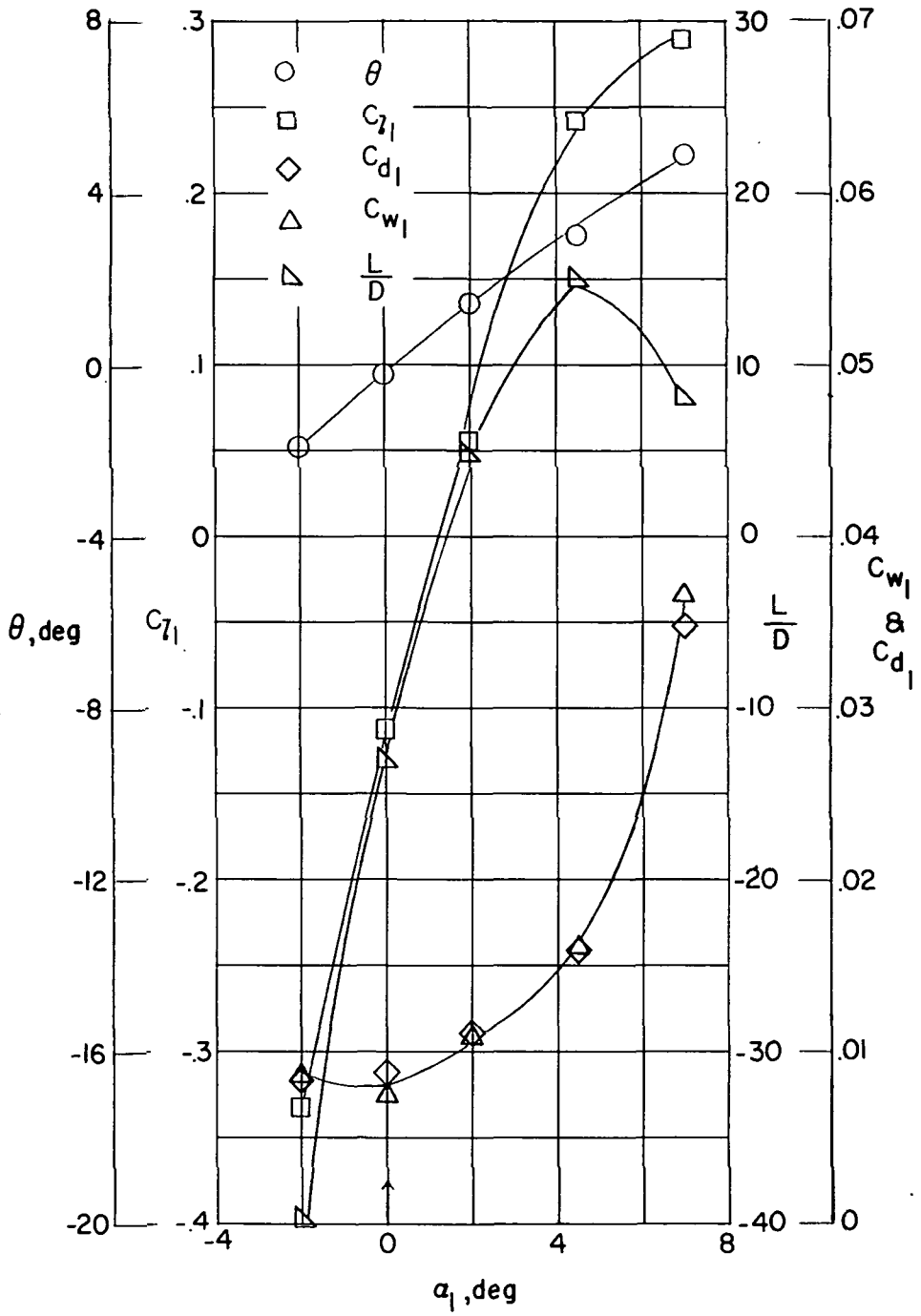

(f) Section characteristics. NACA 65-(0)06; $\beta = 75^\circ$; $\sigma = 0.75$; R = 346,000. Arrow shows α_d.

Figure 23.- Concluded.

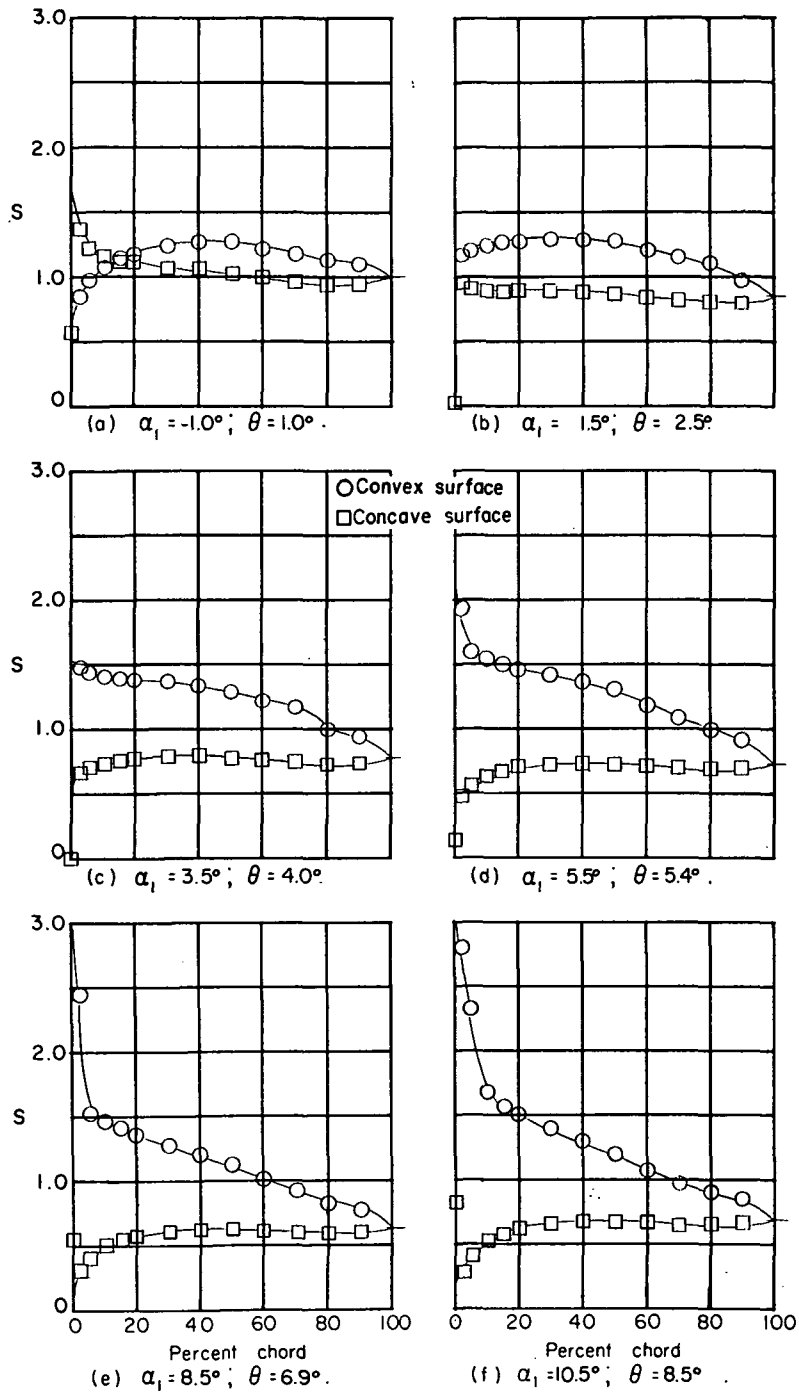

Figure 24.- Blade-surface pressure distributions and section characteristics for the cascade combination $\beta = 75°$, $\sigma = 0.75$, and blade section NACA 65-$(4A_{10})$06.

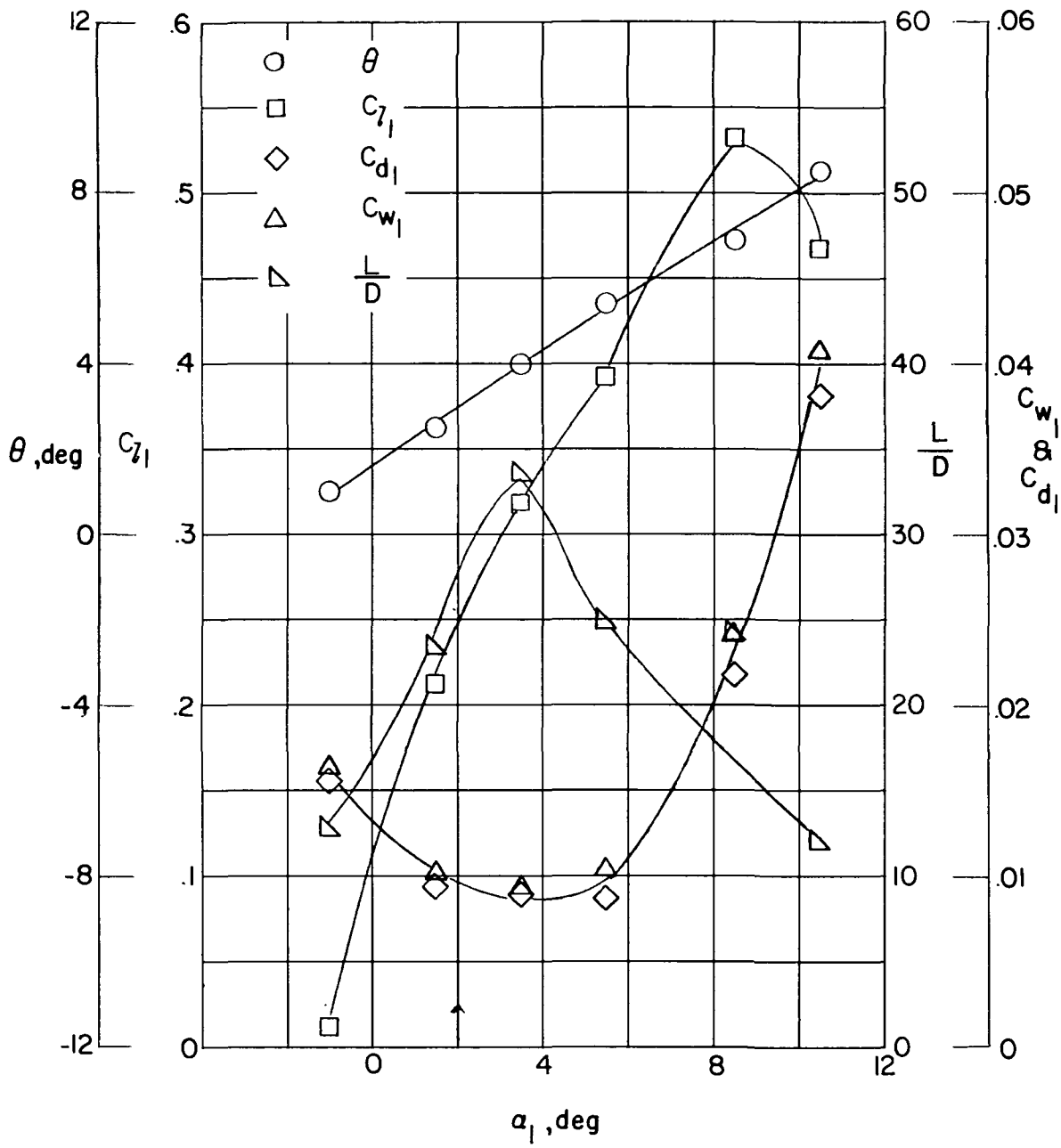

(g) Section characteristics. NACA 65-$(4A_{10})$06; $\beta = 75°$; $\sigma = 0.75$; R = 346,000. Arrow shows α_d.

Figure 24.- Concluded.

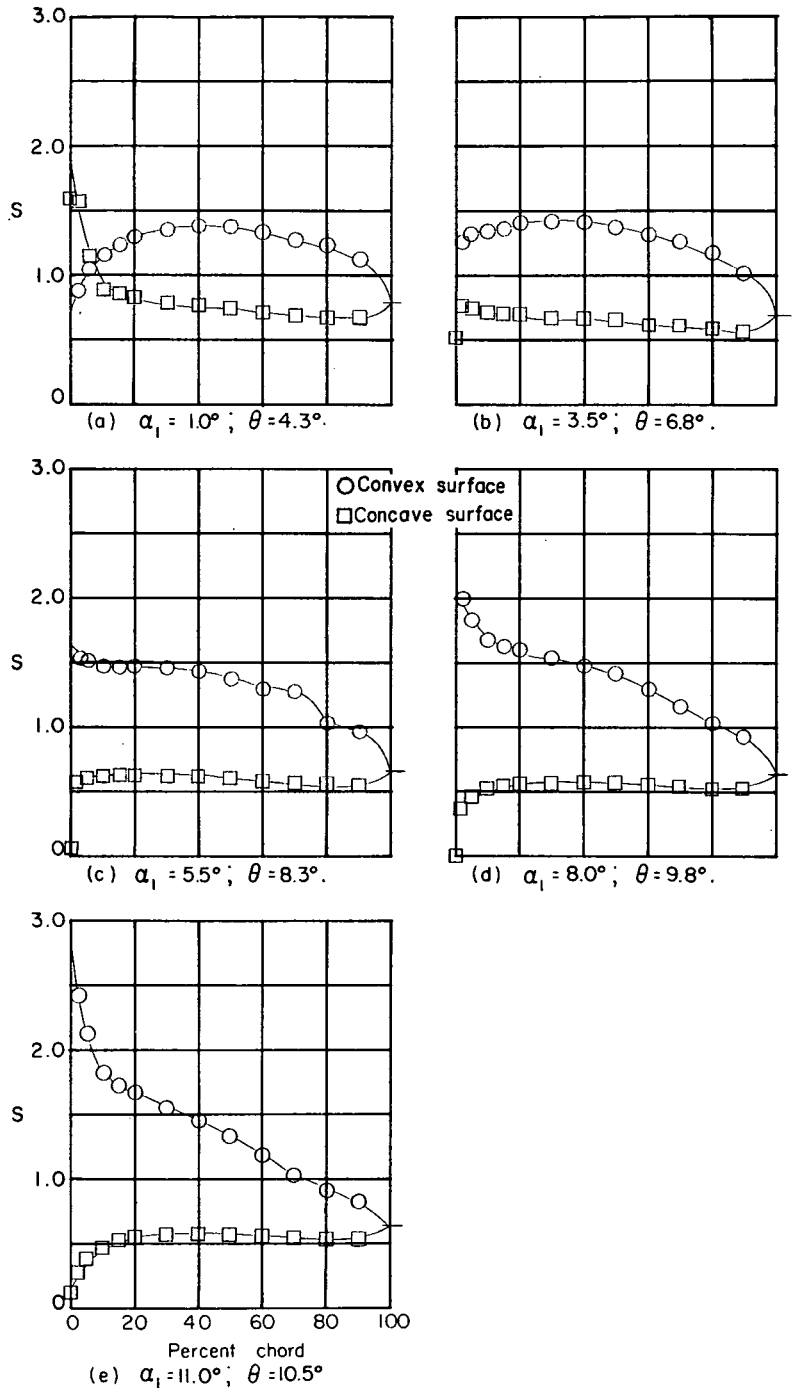

Figure 25.- Blade-surface pressure distributions and section characteristics for the cascade combination $\beta = 75^\circ$, $\sigma = 0.75$, and blade section NACA 65-$\left(8A_{10}\right)$06.

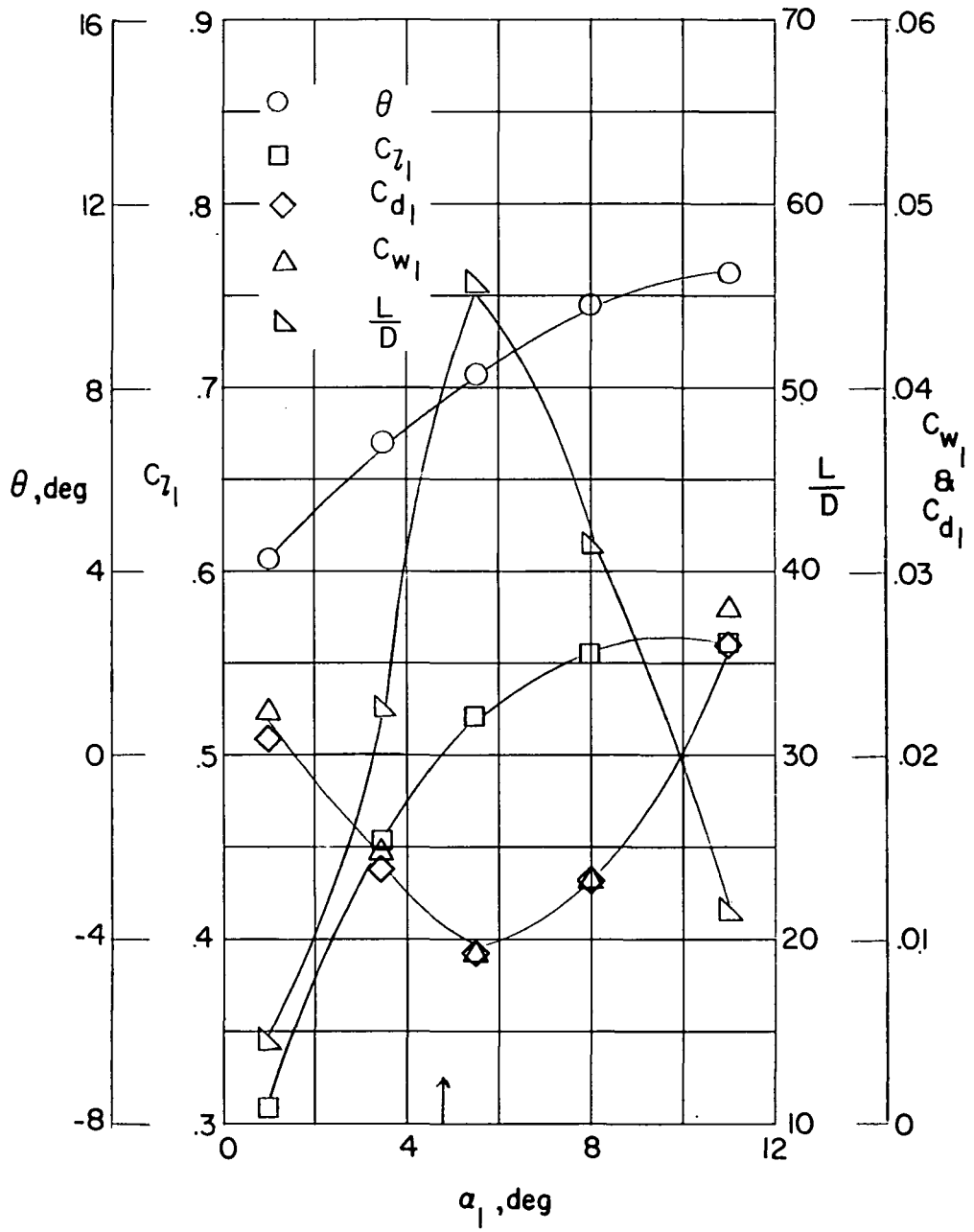

(f) Section characteristics. NACA 65-$(8A_{10})$06; $\beta = 75^{\circ}$; $\sigma = 0.75$; R = 346,000. Arrow shows α_d.

Figure 25.- Concluded.

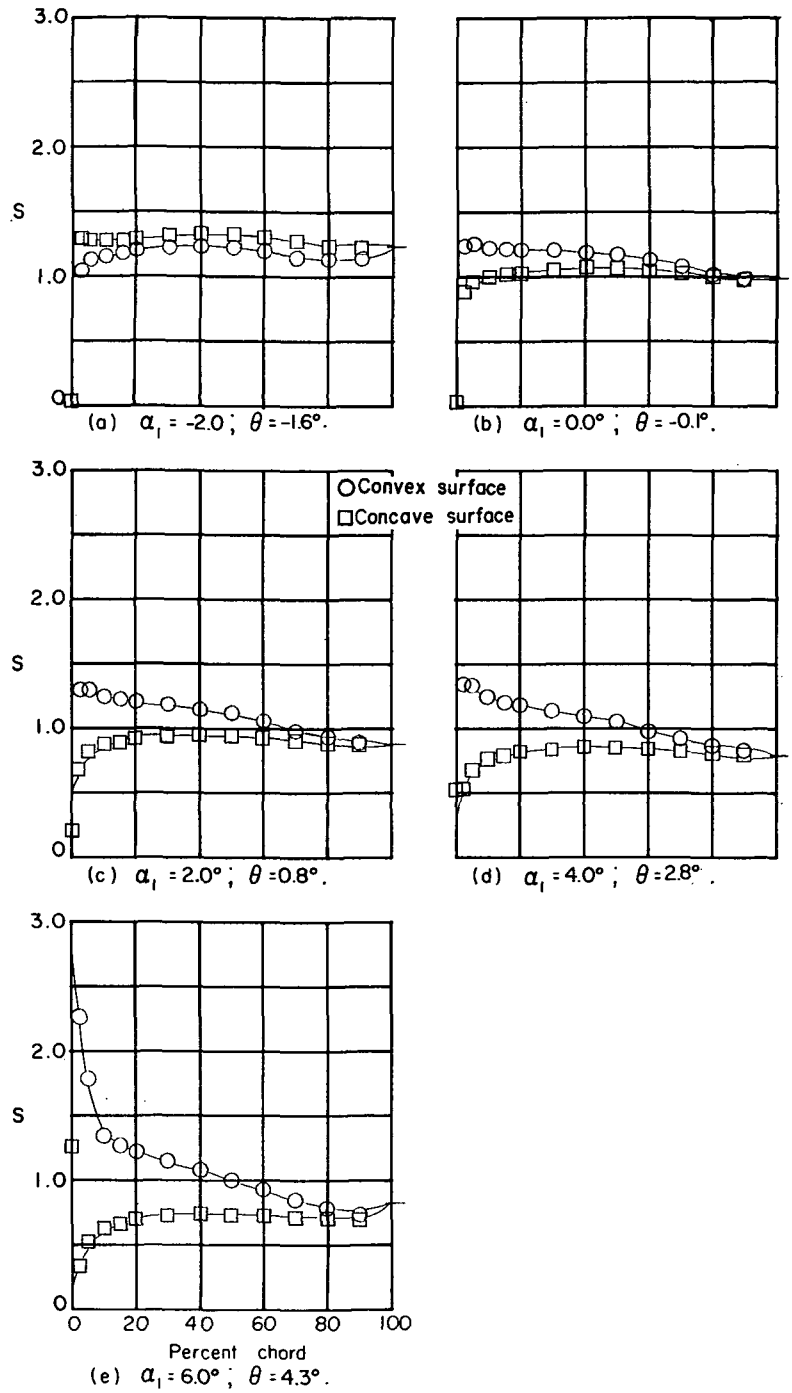

Figure 26.- Blade-surface pressure distributions and section characteristics for the cascade combination $\beta = 75°$, $\sigma = 1.00$, and blade section NACA 65-(0)06.

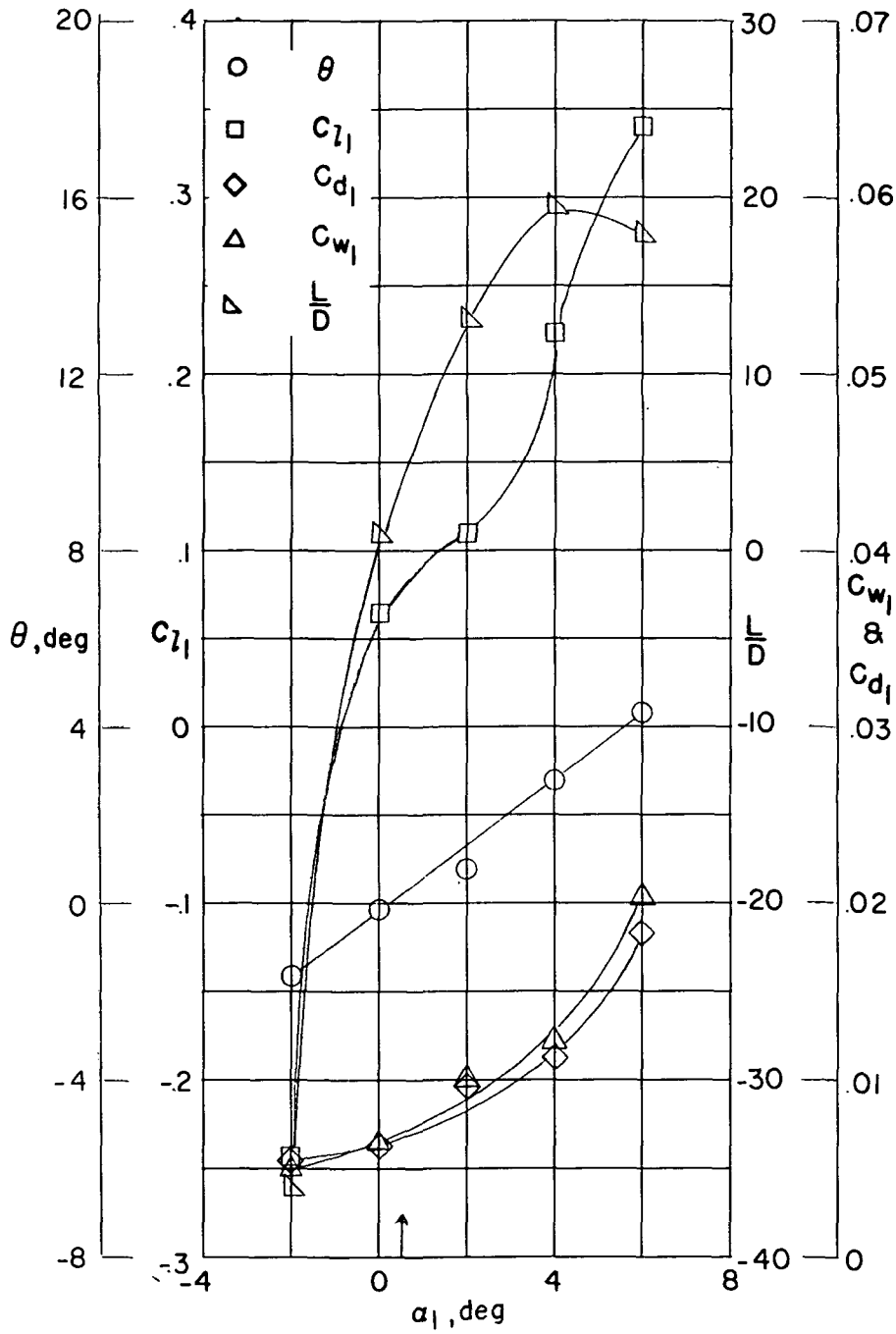

(f) Section characteristics. NACA 65-(0)06; $\beta = 75^{\circ}$; $\sigma = 1.00$; R = 385,000. Arrow shows α_d.

Figure 26.- Concluded.

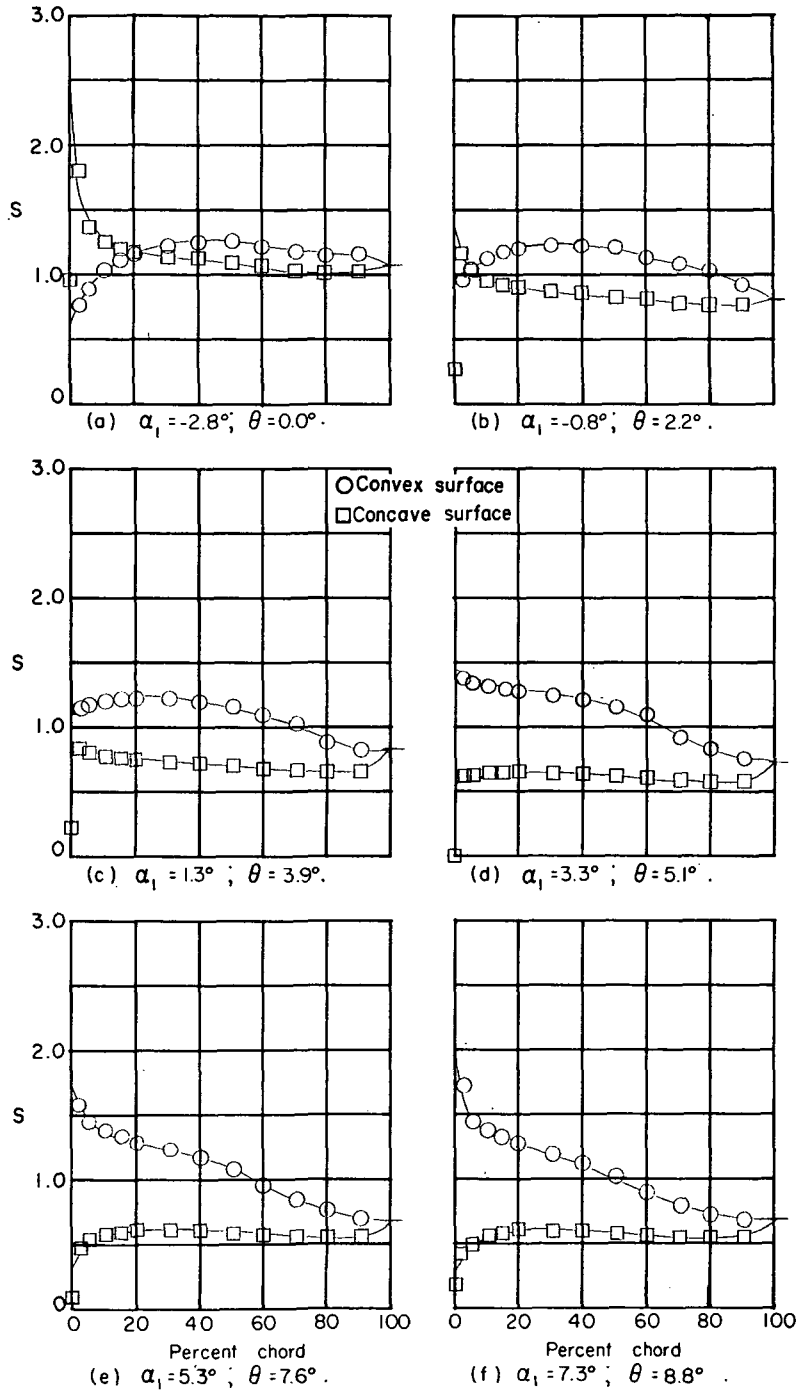

Figure 27.- Blade-surface pressure distributions and section characteristics for the cascade combination $\beta = 75^\circ$, $\sigma = 1.00$, and blade section NACA 65-$(4A_{10})$06.

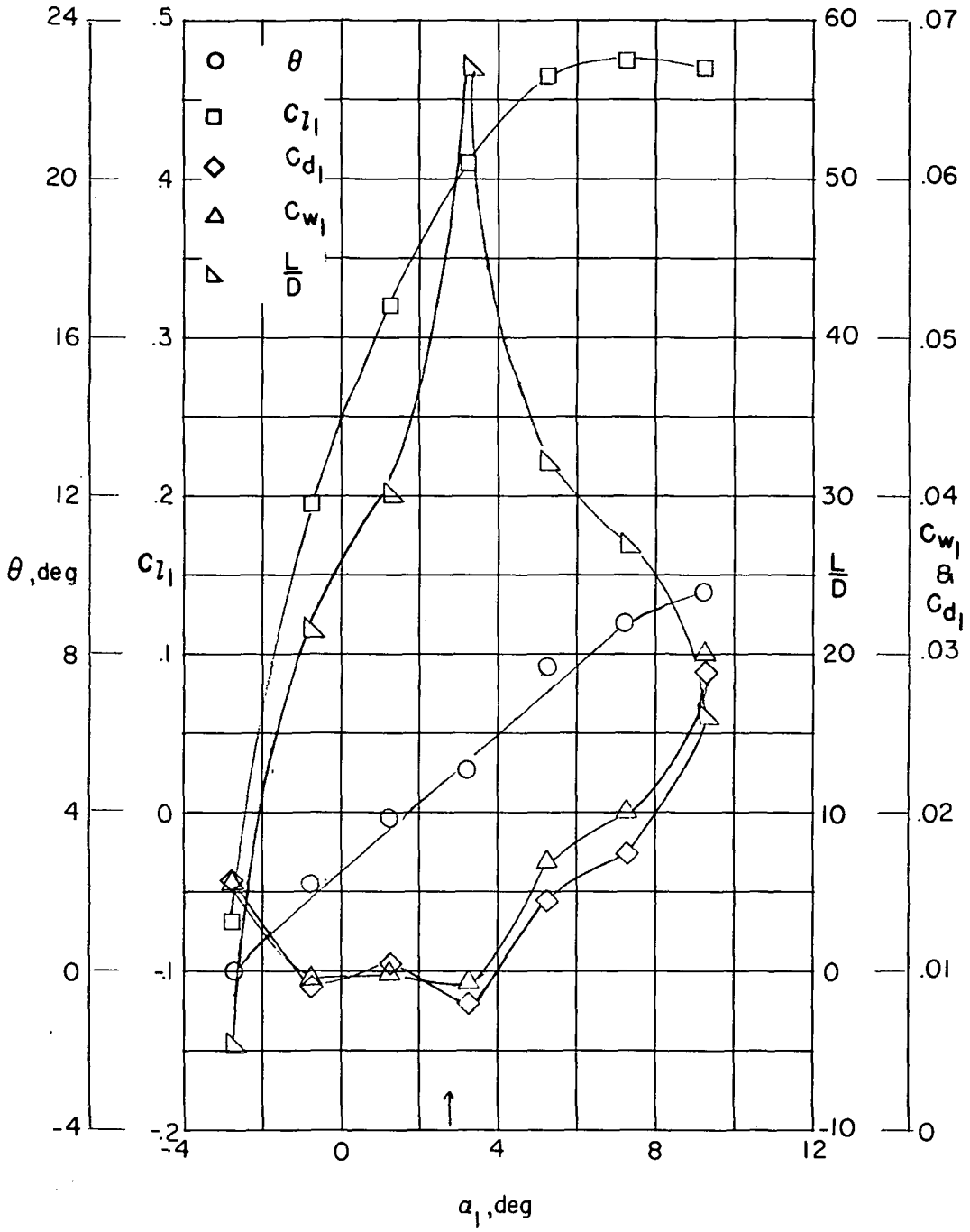

(g) Section characteristics. NACA 65-(4A10)06; $\beta = 75^{\circ}$; $\sigma = 1.00$; R = 385,000. Arrow shows α_d.

Figure 27.- Concluded.

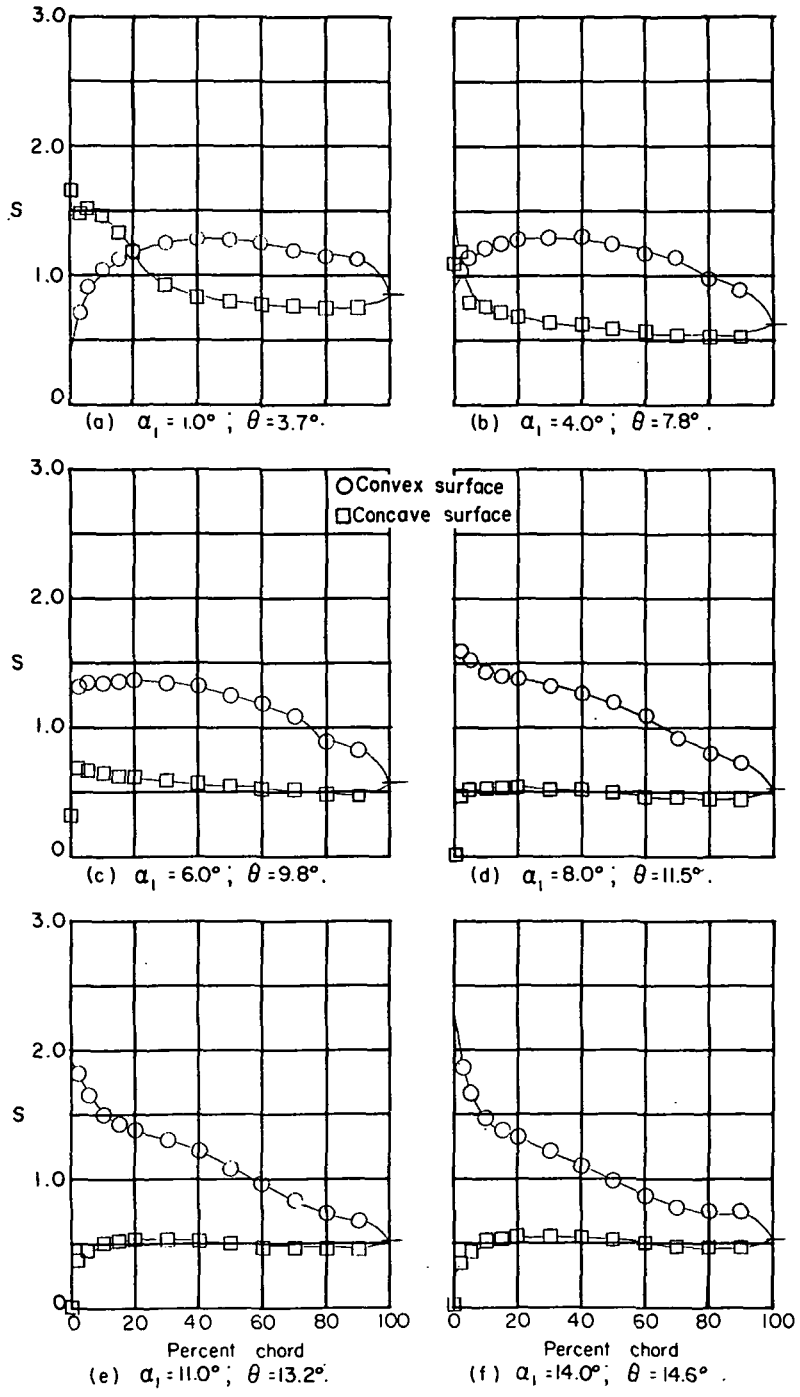

Figure 28.- Blade-surface pressure distributions and section characteristics for the cascade combination $\beta = 75^\circ$, $\sigma = 1.00$, and blade section NACA 65-$(8A_{10})$06.

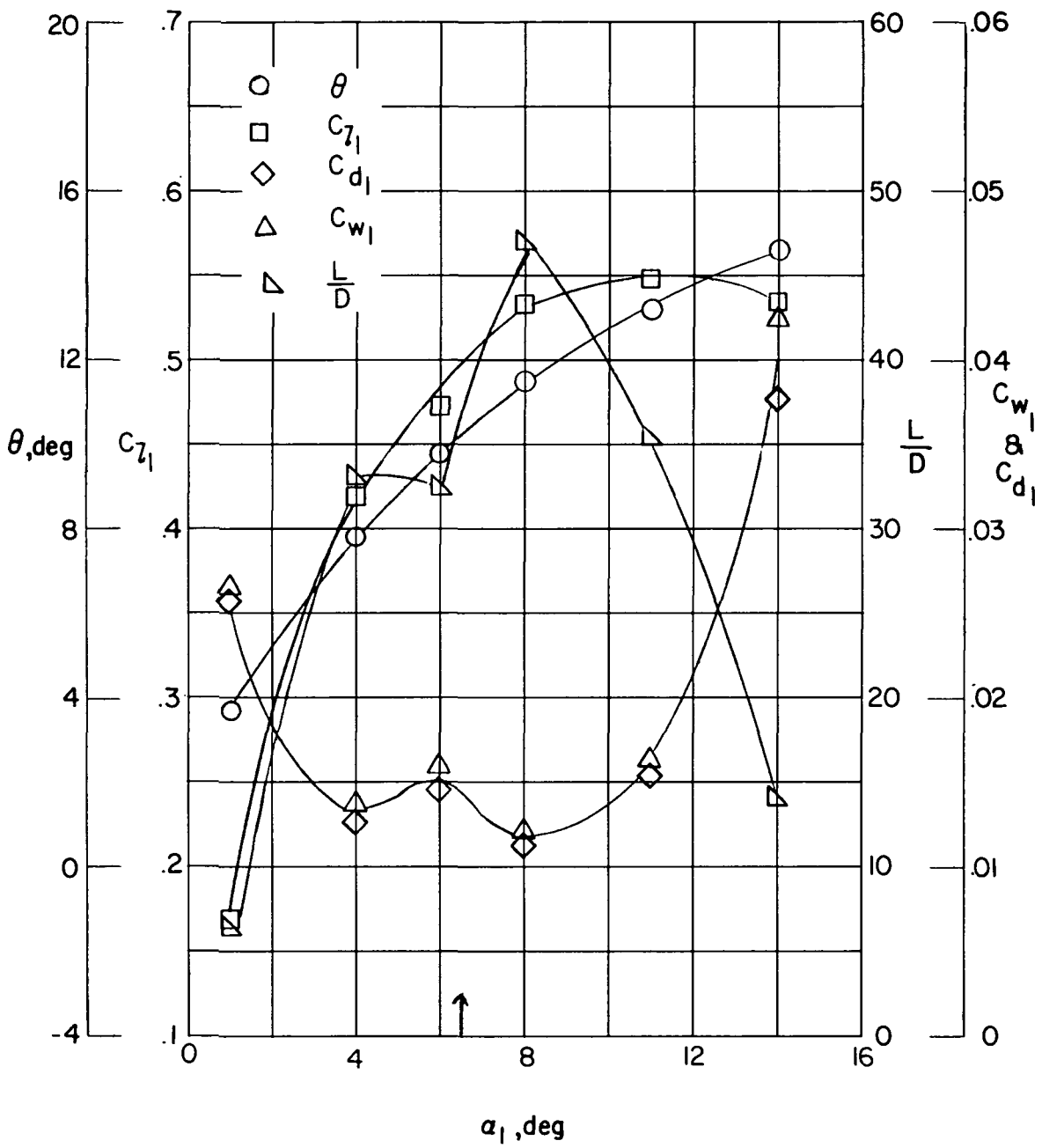

(g) Section characteristics. NACA 65-$(8A_{10})$06; β = 75°; σ = 1.00; R = 346,000. Arrow shows α_d.

Figure 28.- Concluded.

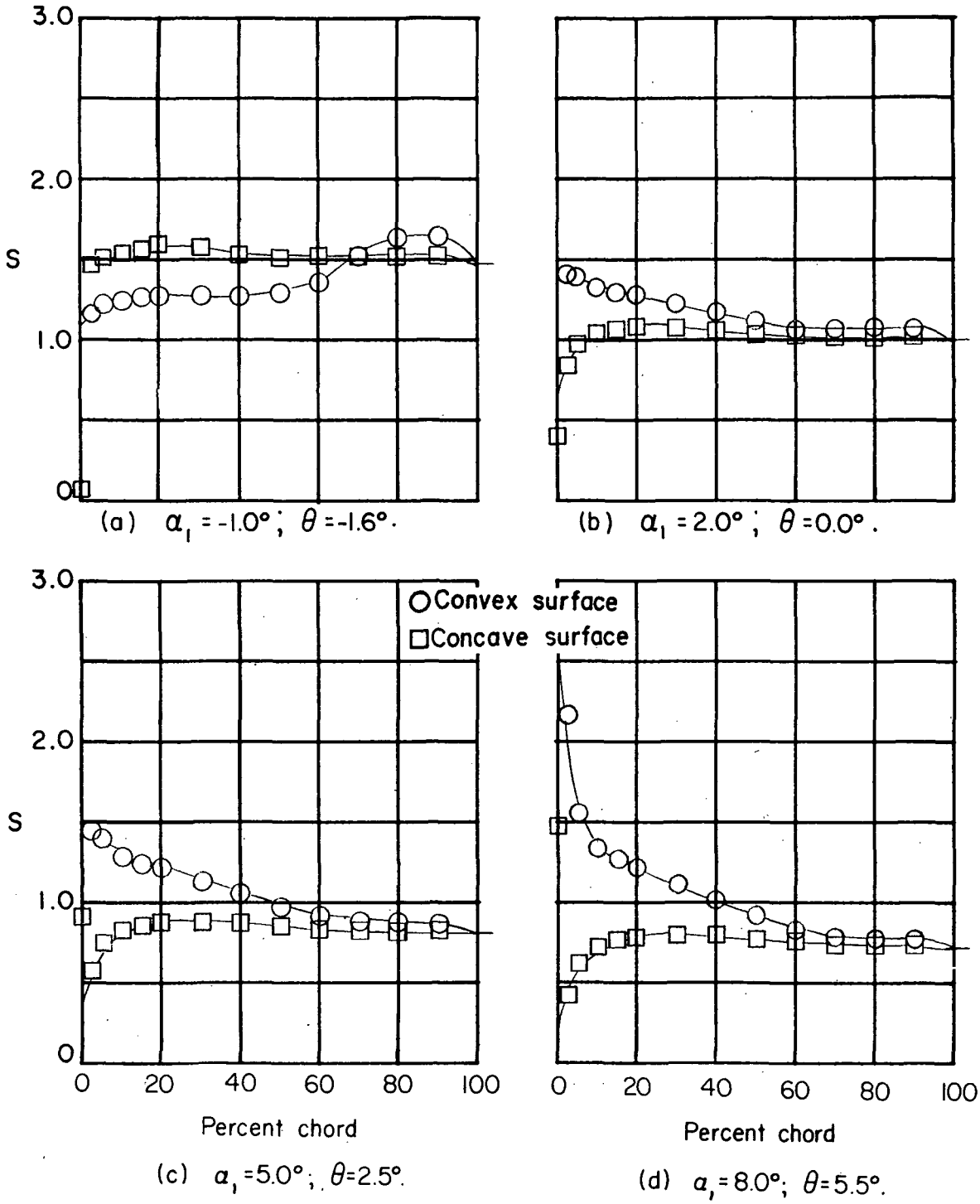

Figure 29.- Blade-surface pressure distributions and section characteristics for the cascade combination $\beta = 75°$, $\sigma = 1.50$, and blade section NACA 65-(0)06.

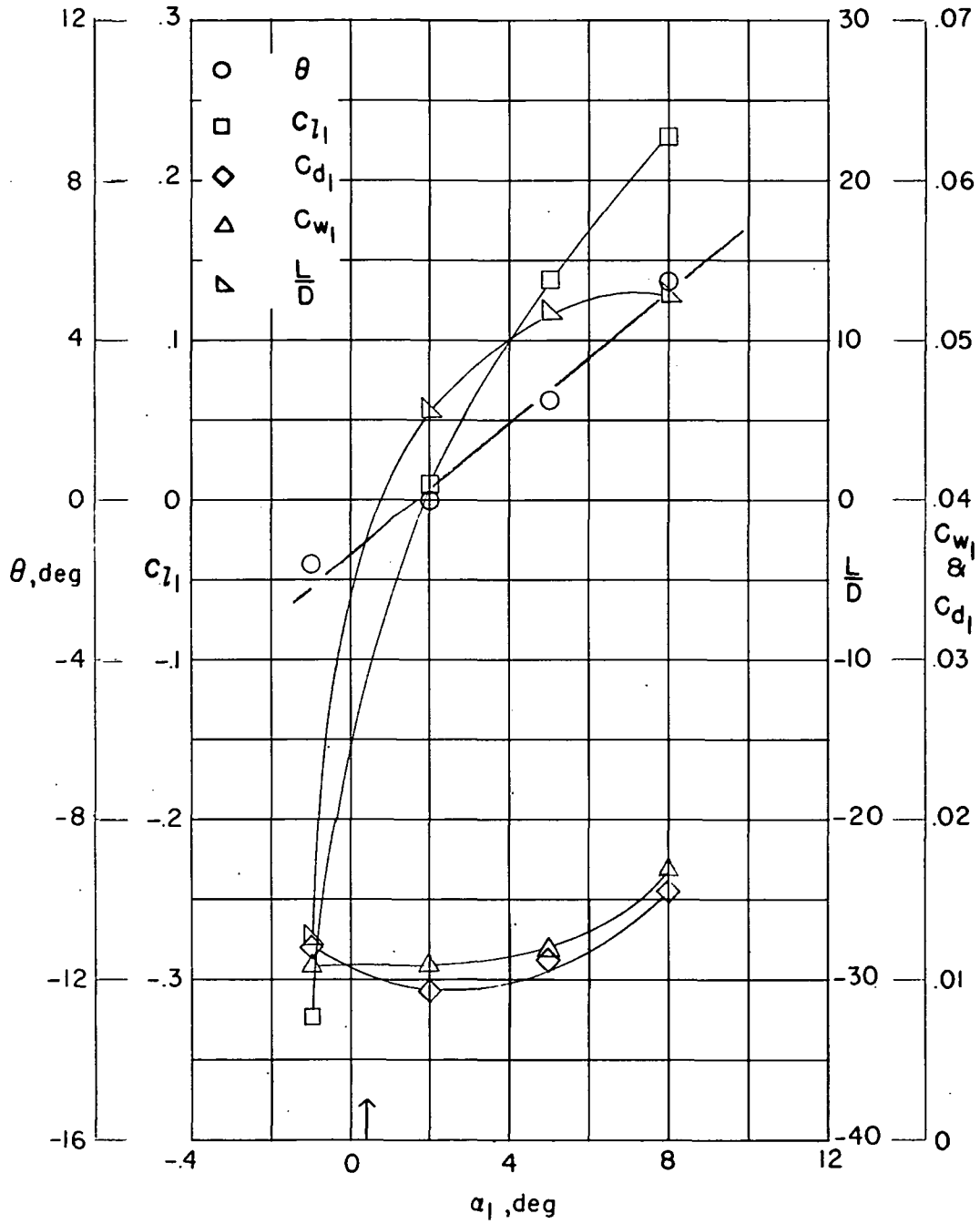

(e) Section characteristics. NACA 65-(0)06; $\beta = 75^\circ$; $\sigma = 1.50$; $R = 346{,}000$. Arrow shows α_d.

Figure 29.- Concluded.

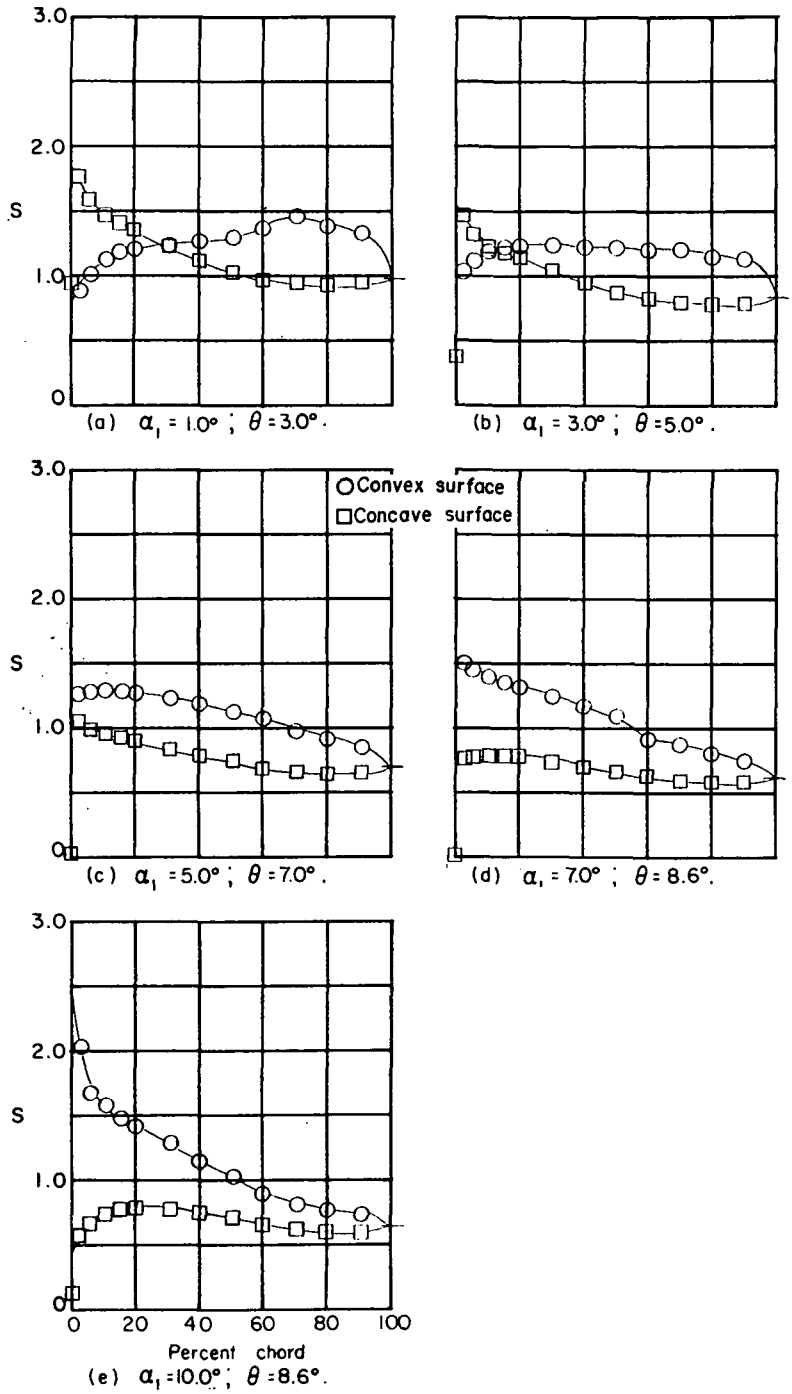

Figure 30.- Blade-surface pressure distributions and section characteristics for the cascade combination $\beta = 75^{\circ}$, $\sigma = 1.50$, and blade section NACA 65-$(4A_{10})$06.

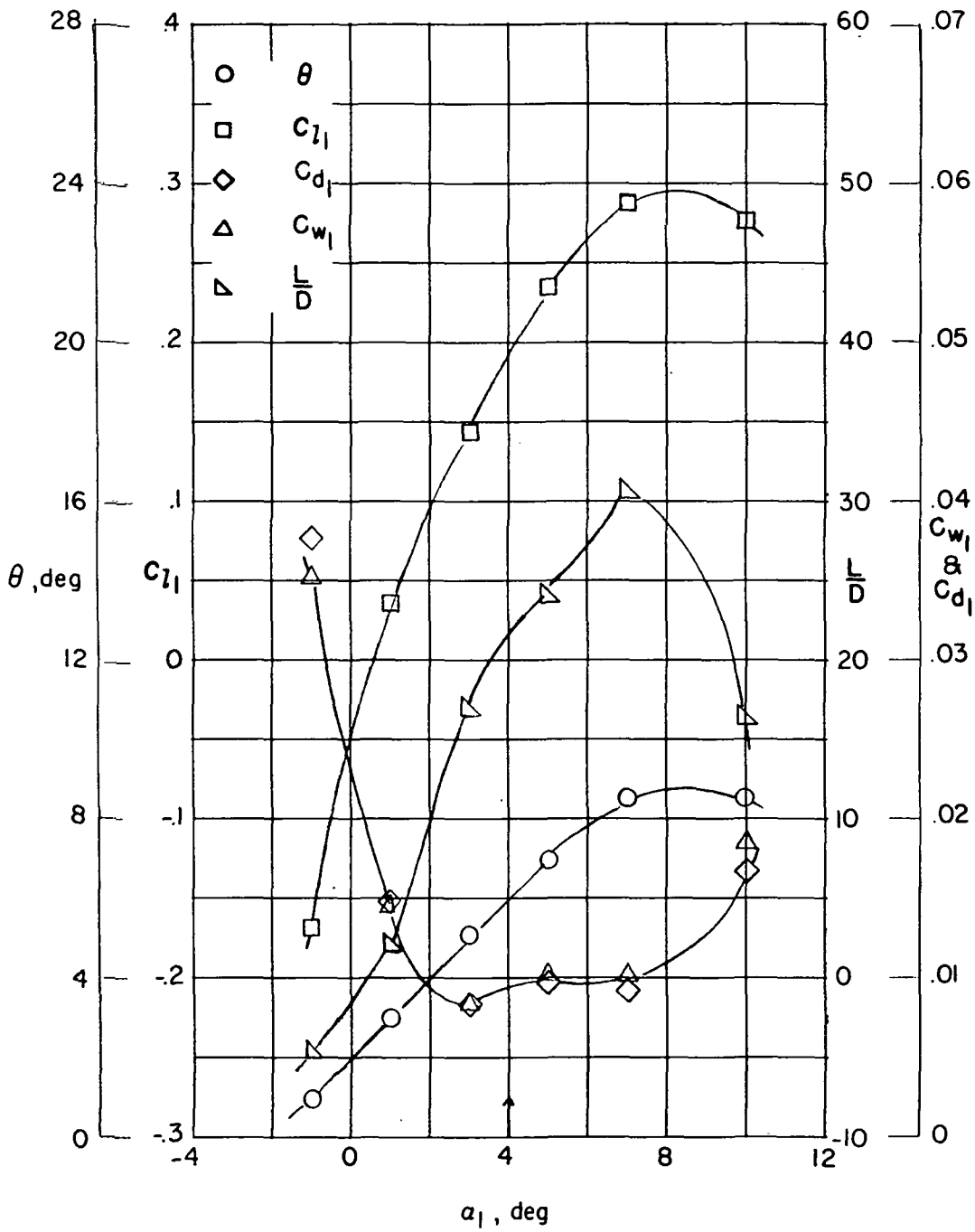

(f) Section characteristics. NACA 65-$(4A_{10})$06; $\beta = 75^{\circ}$; $\sigma = 1.50$; $R = 346{,}000$. Arrow shows α_d.

Figure 30.- Concluded.

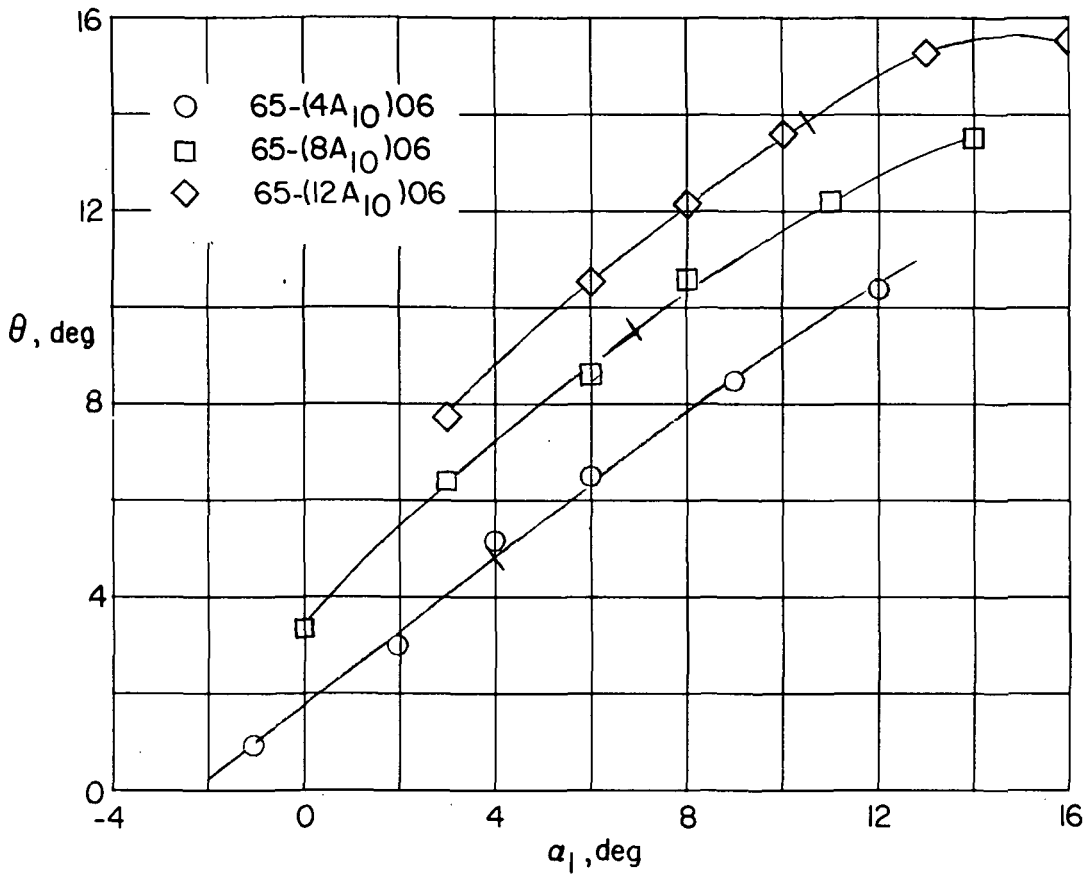

(a) $\beta = 60^{\circ}$; $\sigma = 0.75$.

Figure 31.- Summaries of the relationships between exit angle and angle of attack for the NACA blade sections tested. (Ticks across curves indicate design points.)

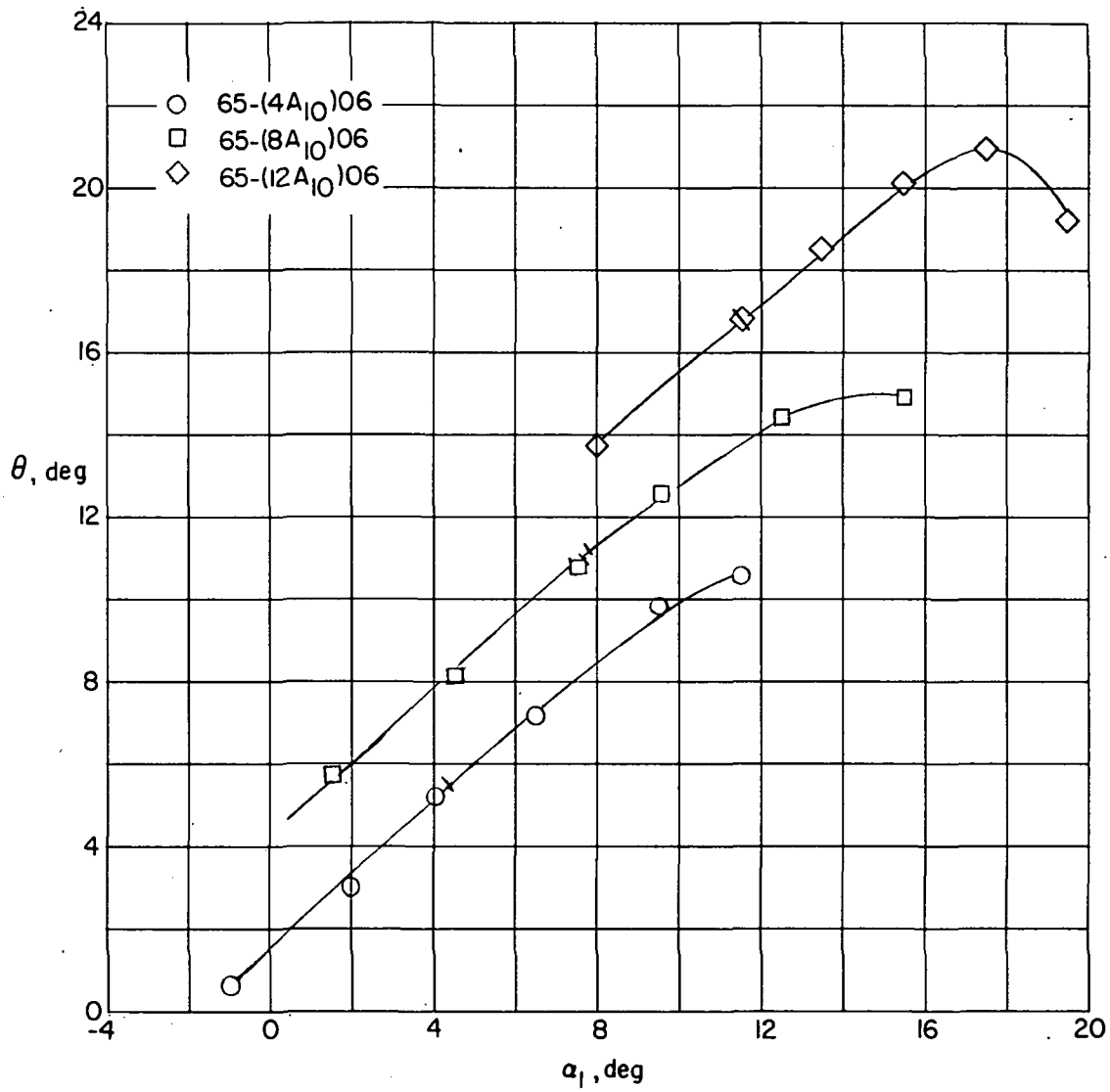

(b) $\beta = 60^{\circ}$; $\sigma = 1.00$.

Figure 31.- Continued.

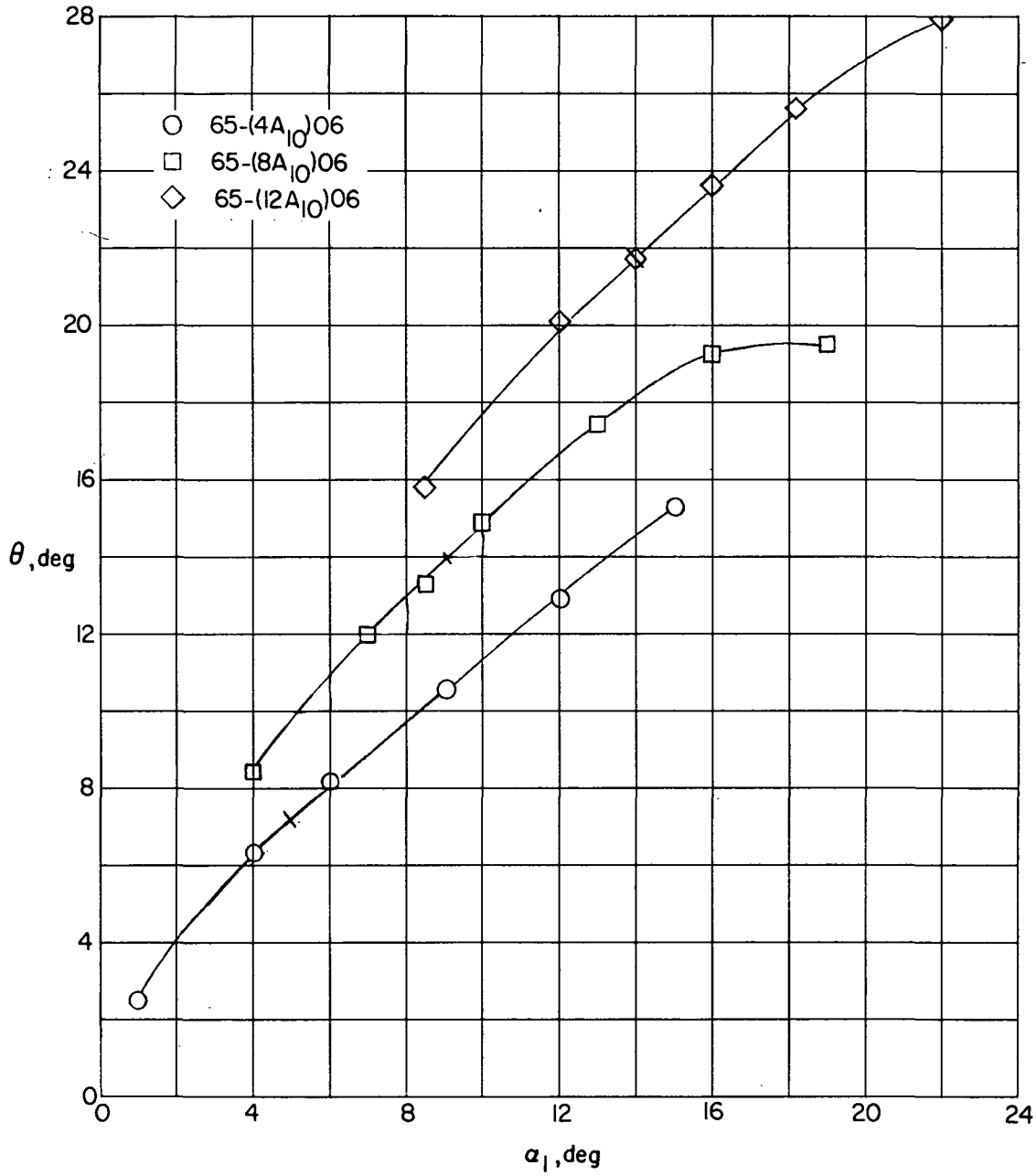

(c) $\beta = 60^{\circ}$; $\sigma = 1.50$.

Figure 31.- Continued.

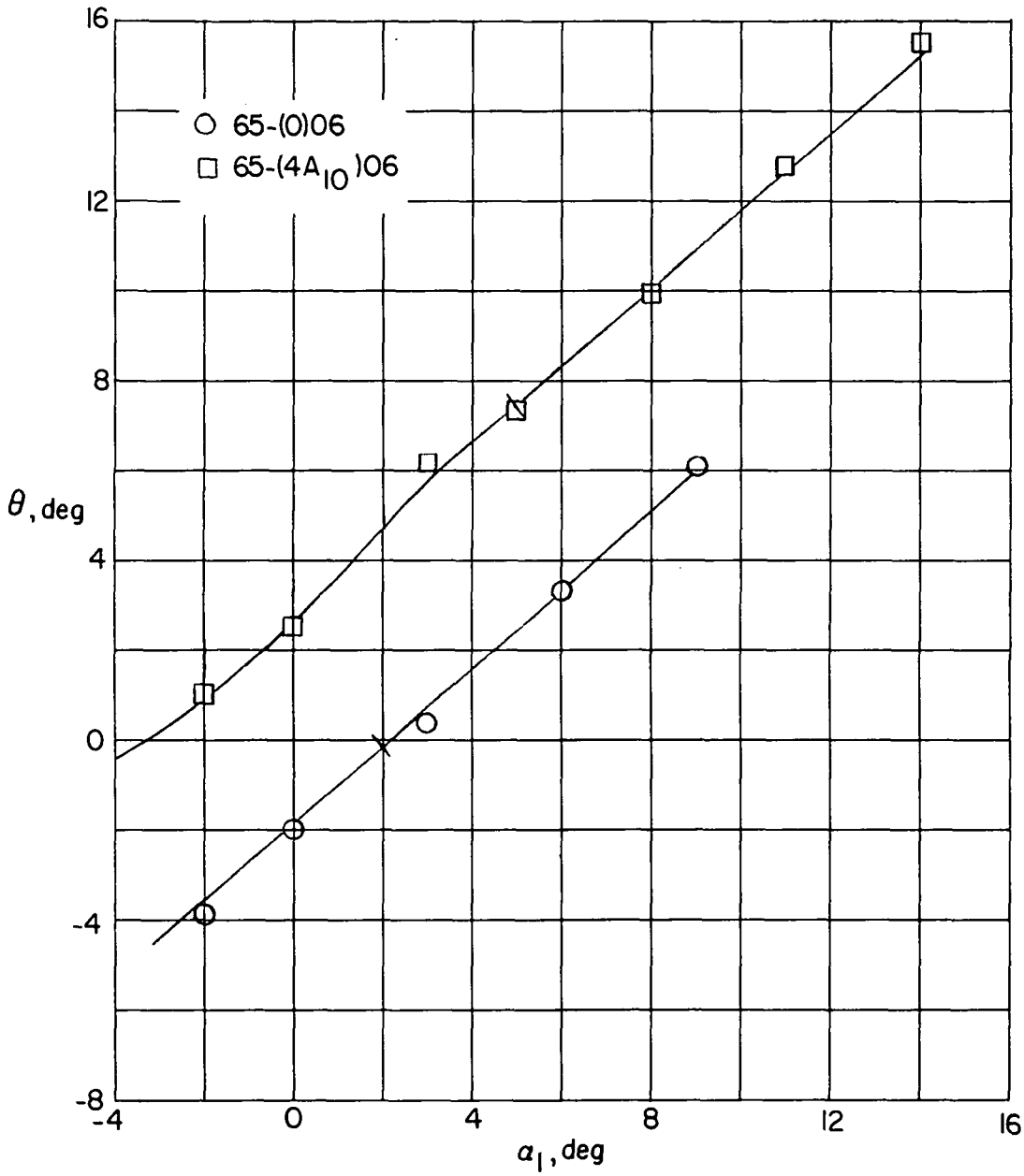

(d) $\beta = 60^{\circ}$; $\sigma = 2.00$.

Figure 31.- Continued.

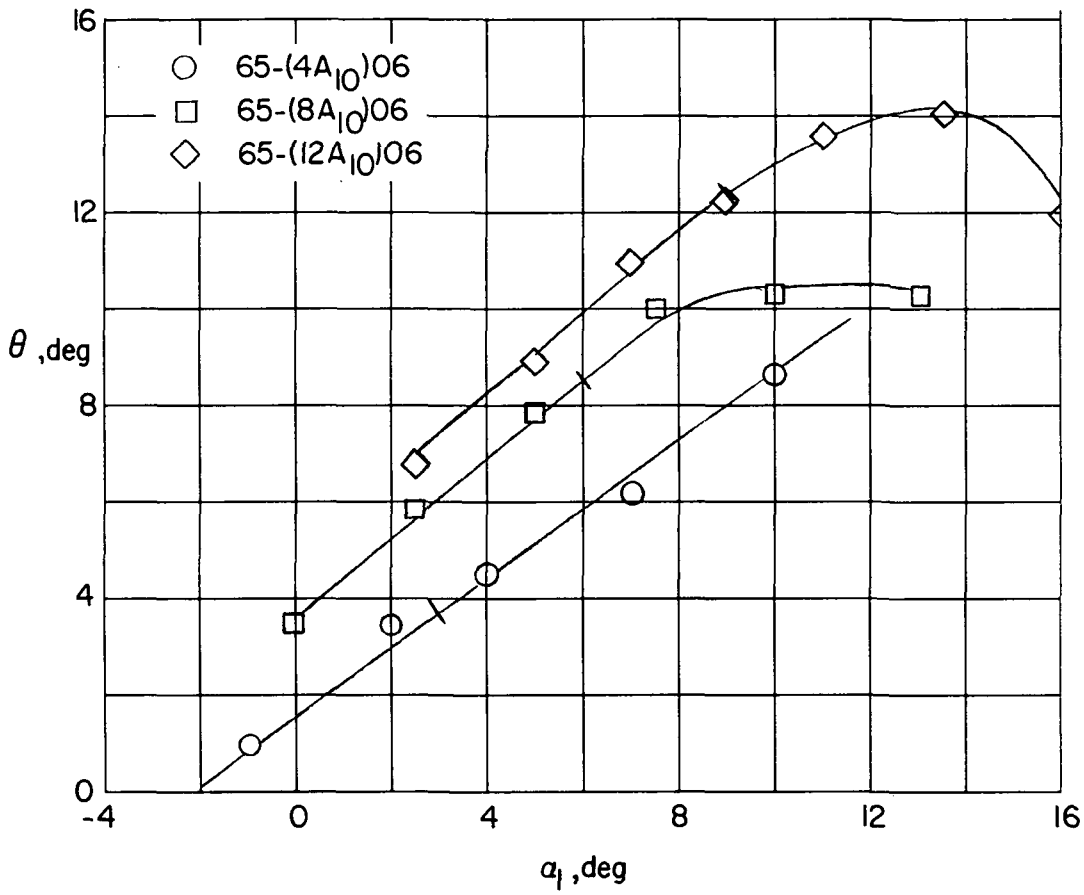

(e) $\beta = 70^{\circ}$; $\sigma = 0.75$.

Figure 31.- Continued.

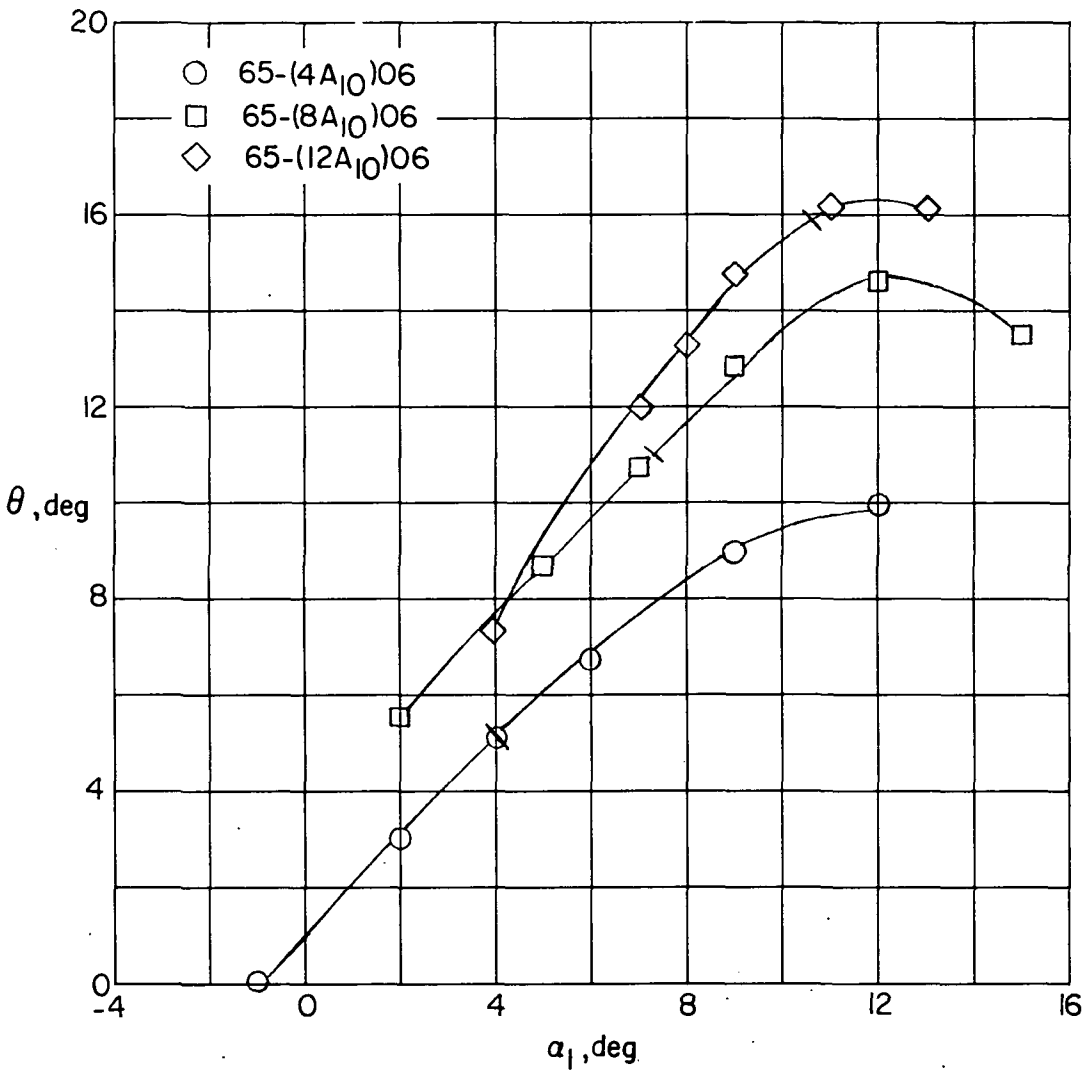

(f) $\beta = 70^{\circ}$; $\sigma = 1.00$.

Figure 31.- Continued.

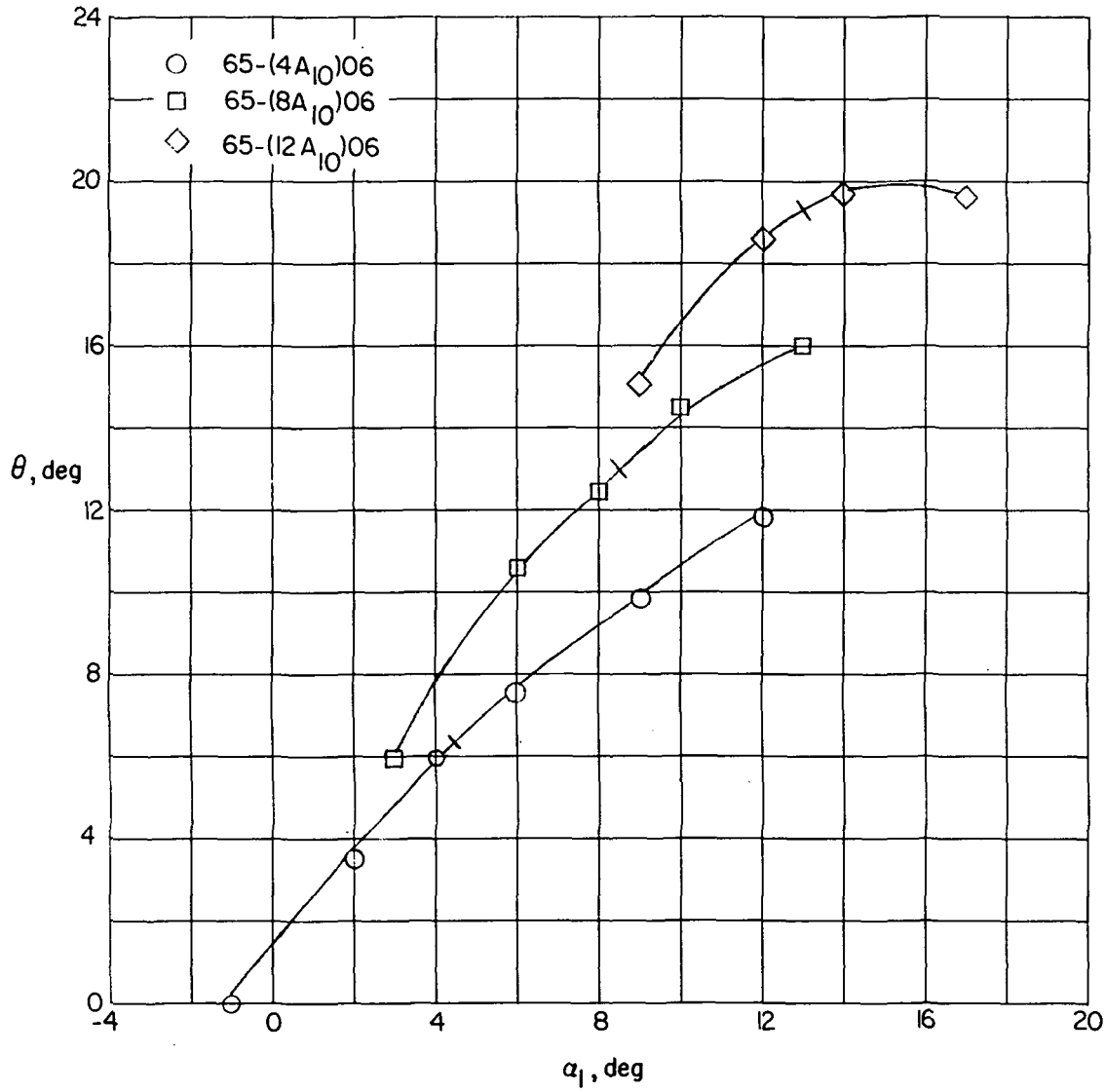

(g) $\beta = 70^{\circ}$; $\sigma = 1.50$.

Figure 31.- Continued.

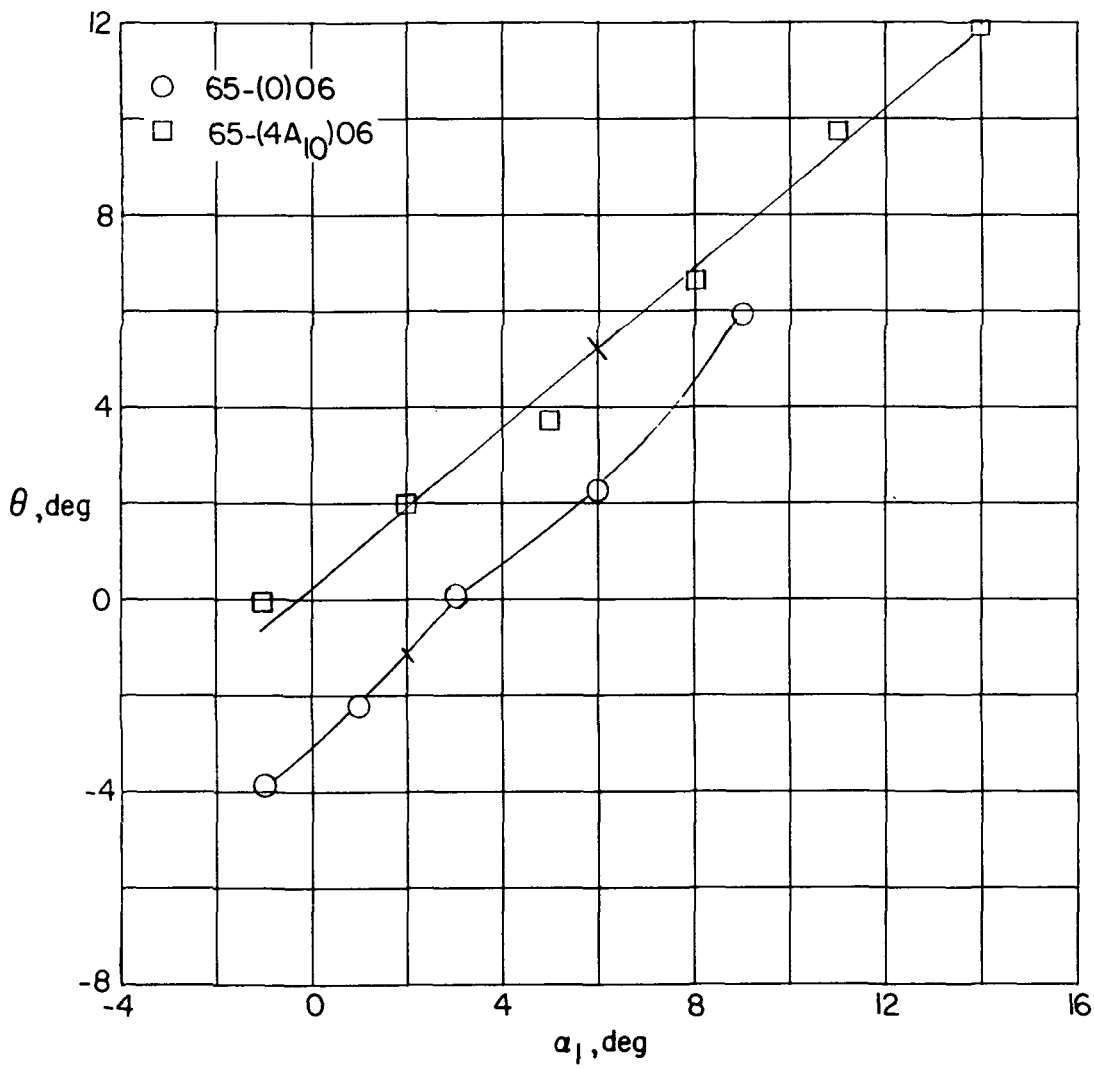

(h) $\beta = 70^{\circ}$; $\sigma = 2.00$.

Figure 31.- Continued.

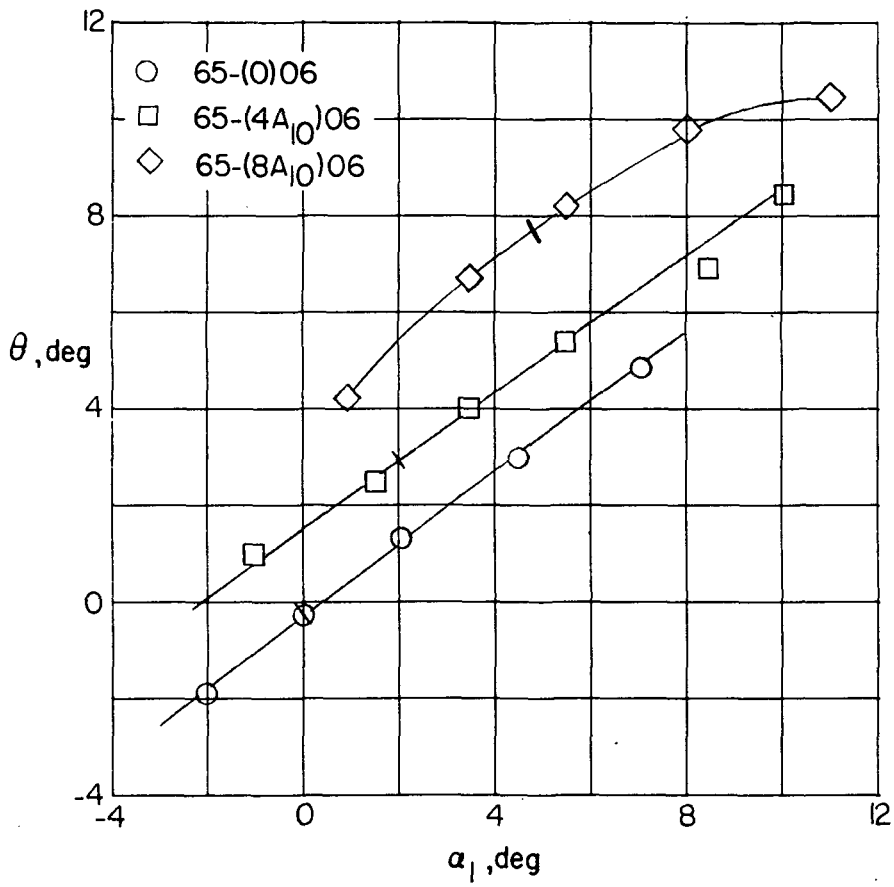

(i) $\beta = 75^{\circ}$; $\sigma = 0.75$.

Figure 31.- Continued.

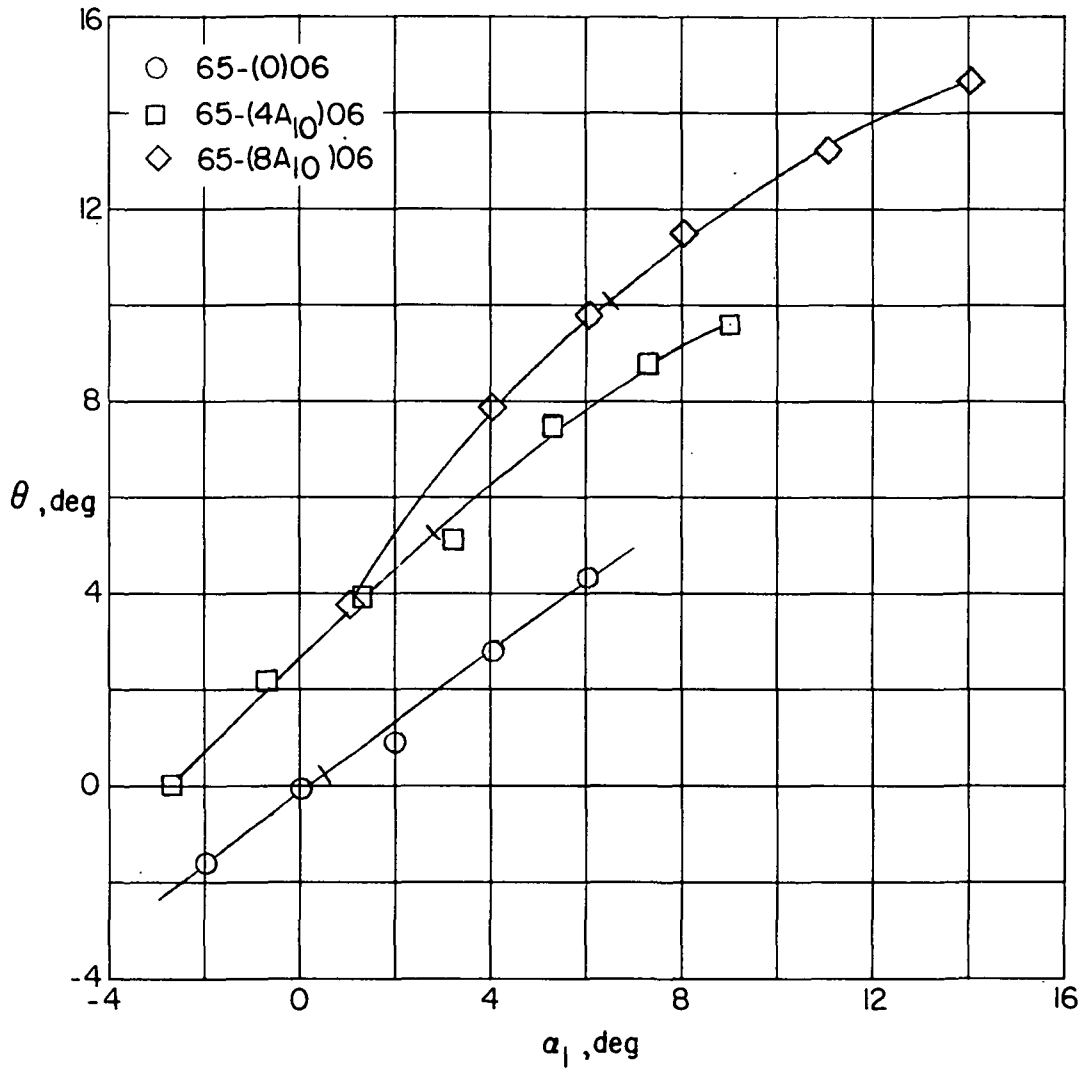

(j) $\beta = 75^{\circ}$; $\sigma = 1.00$.

Figure 31.- Continued.

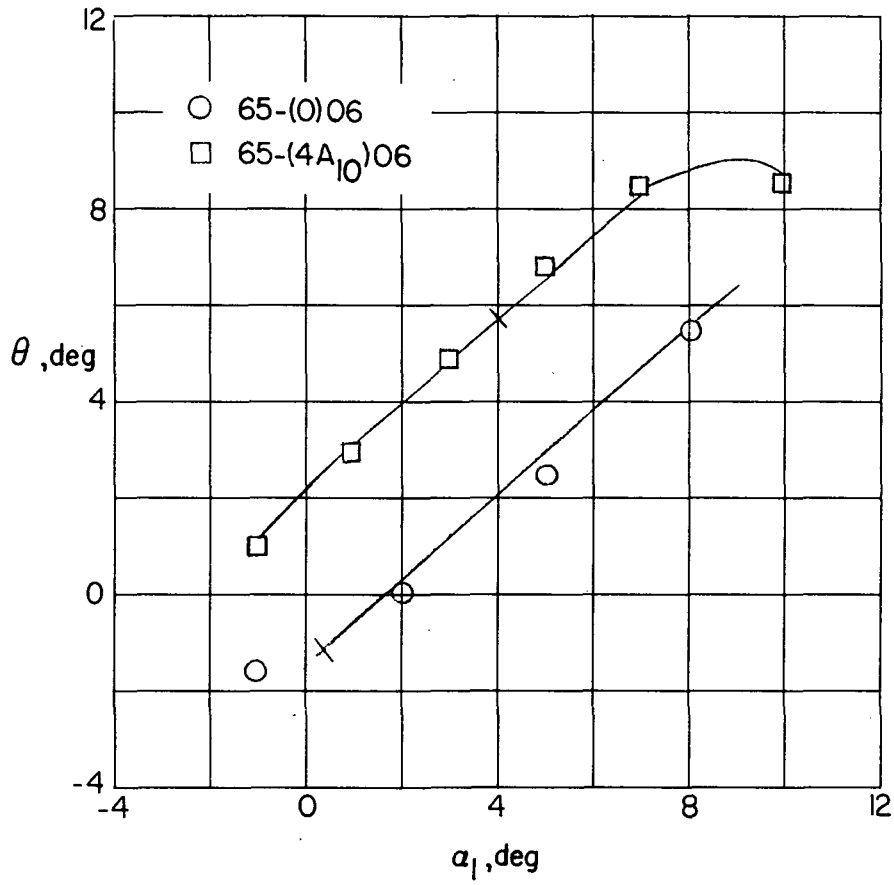

(k) $\beta = 75^{\circ}$; $\sigma = 1.50$.

Figure 31.- Concluded.

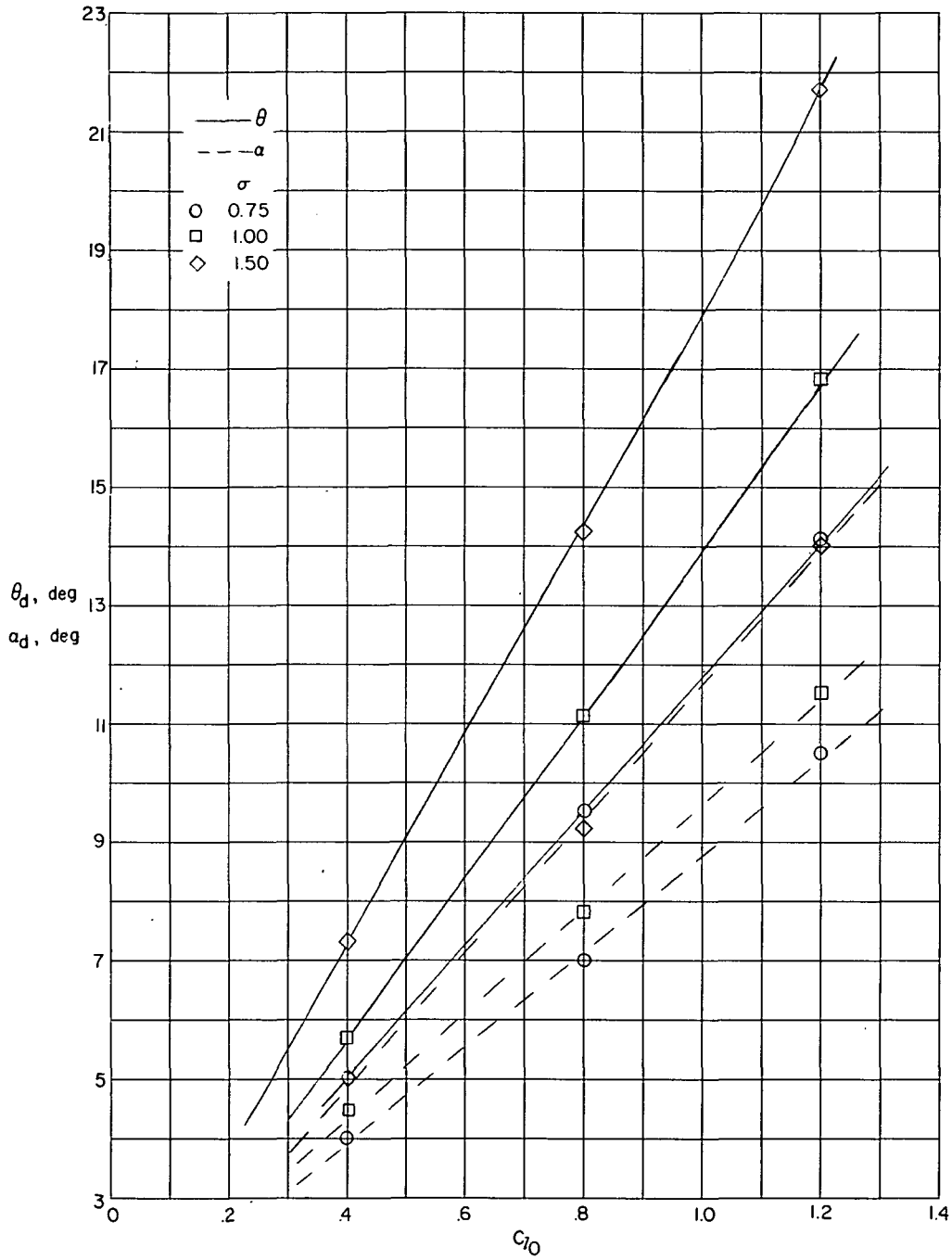

(a) $\beta = 60^{\circ}$.

Figure 32.- Variation of design exit angle and design angle of attack with camber for three 6-percent-thick NACA 65-series blades sections.

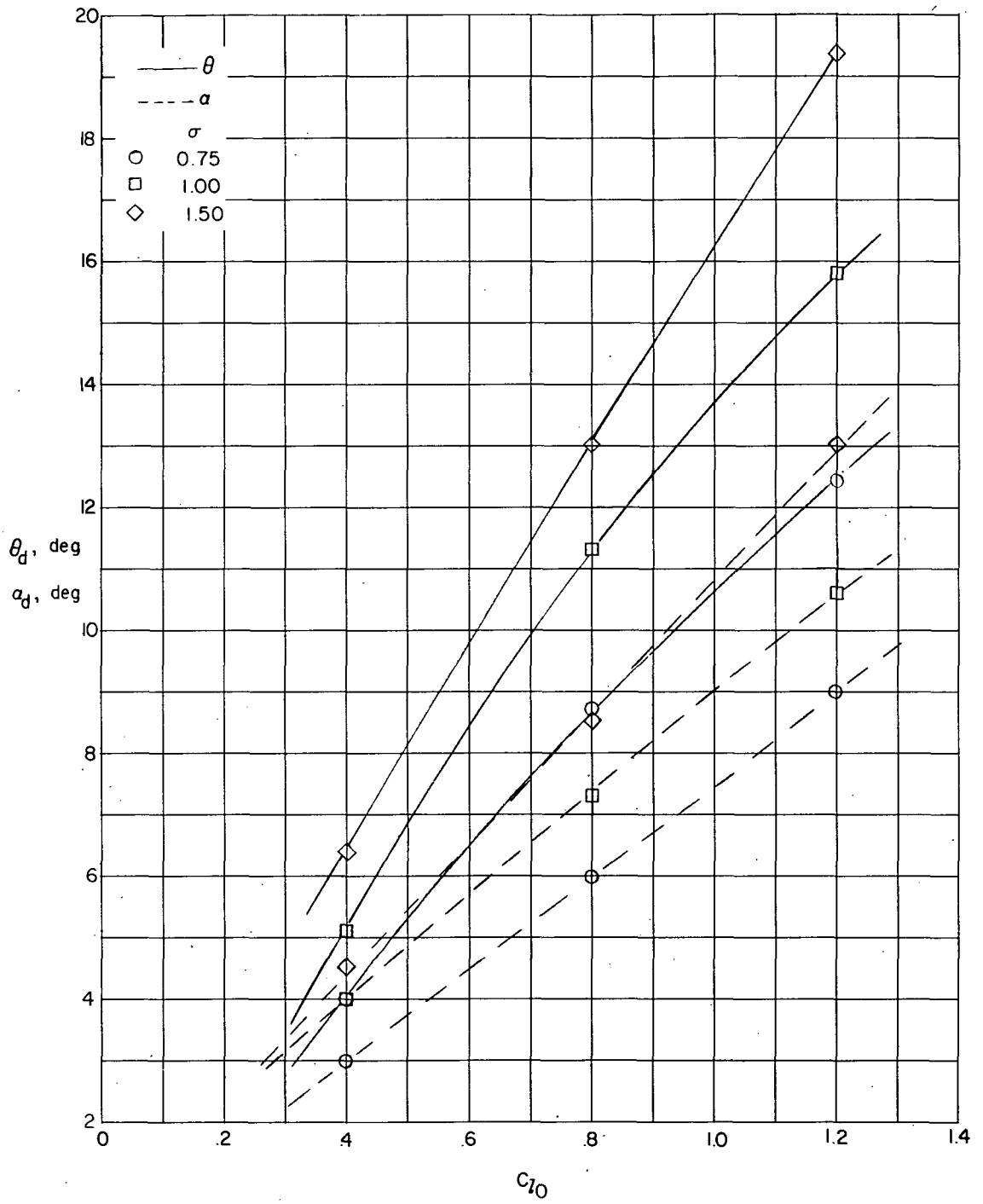

(b) $\beta = 70^{\circ}$.

Figure 32.- Continued.

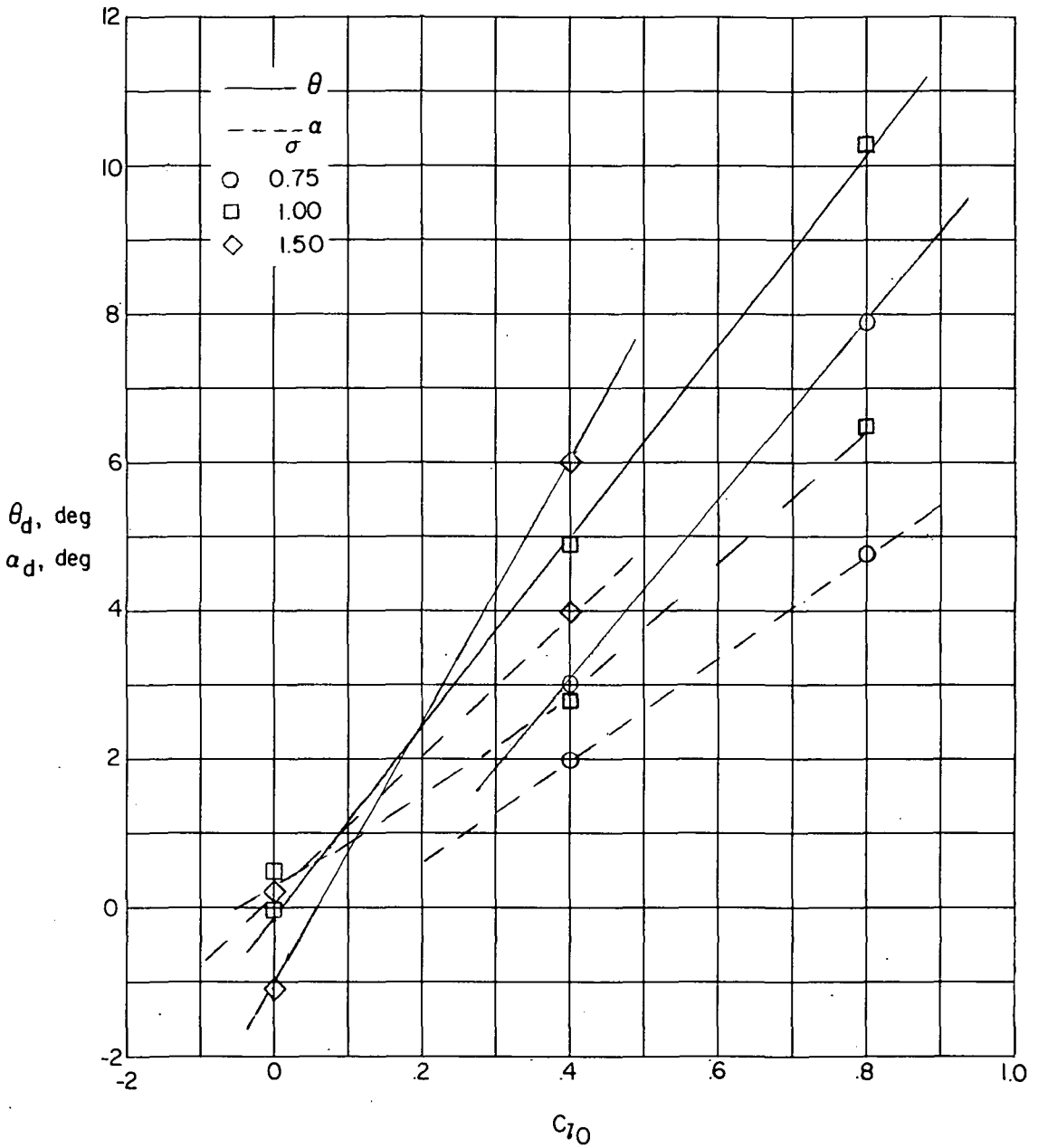

(c) $\beta = 75^{\circ}$.

Figure 32.- Concluded.

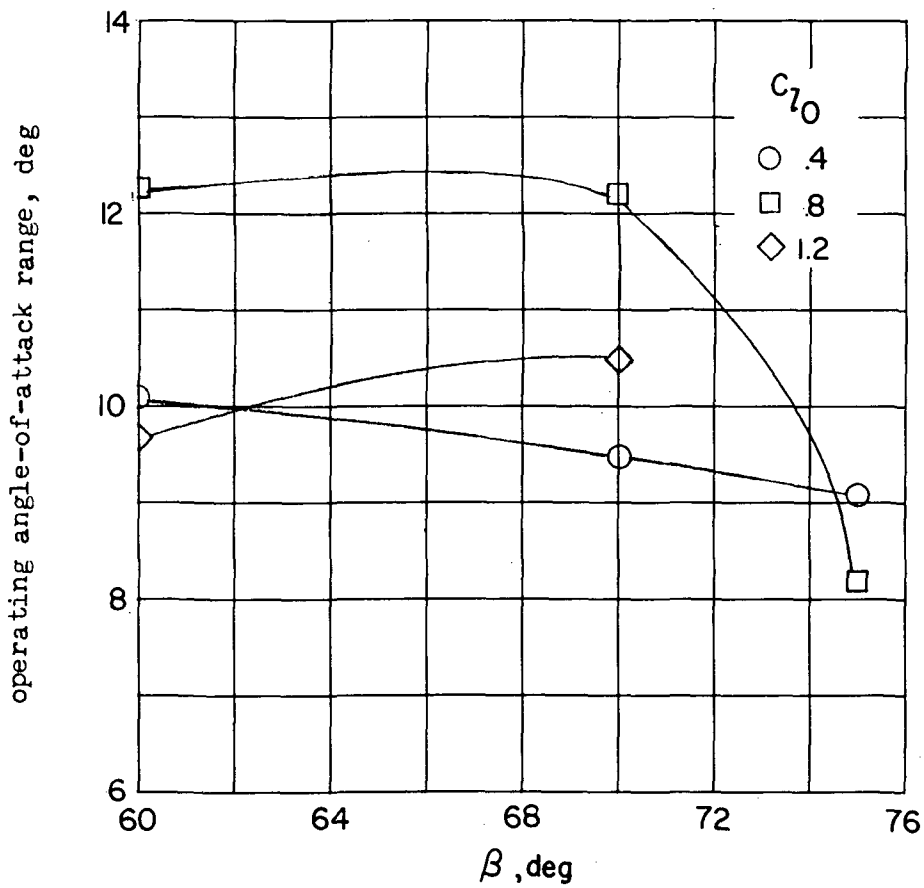

(a) $\sigma = 0.75$.

Figure 33.- Variation of the estimated operating angle-of-attack range with inlet angle for several cambers. 6-percent-thick NACA 65-series blade sections.

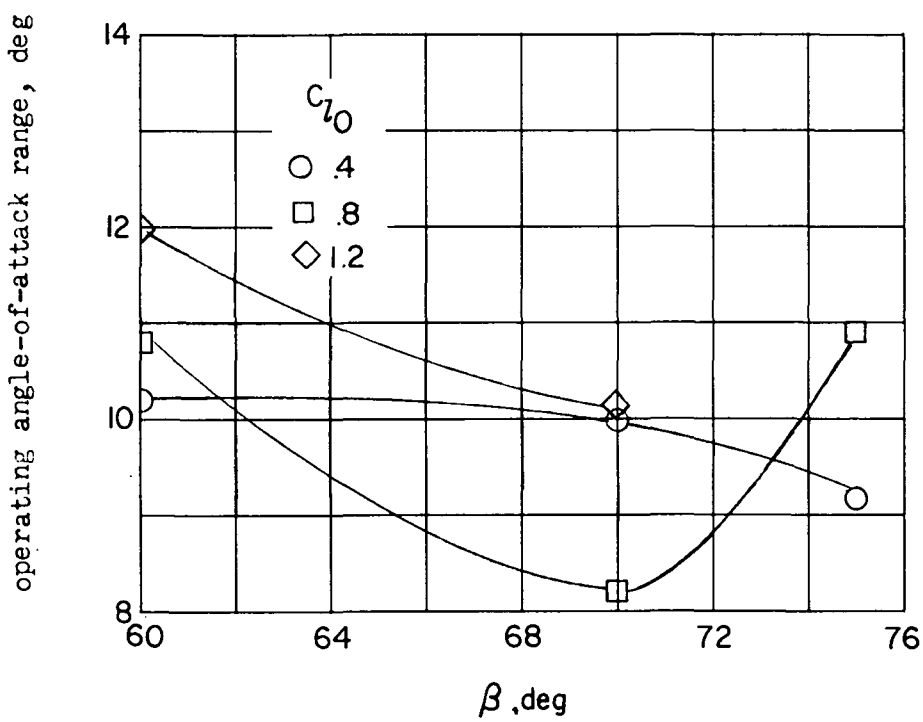

(b) $\sigma = 1.00$.

Figure 33.- Continued.

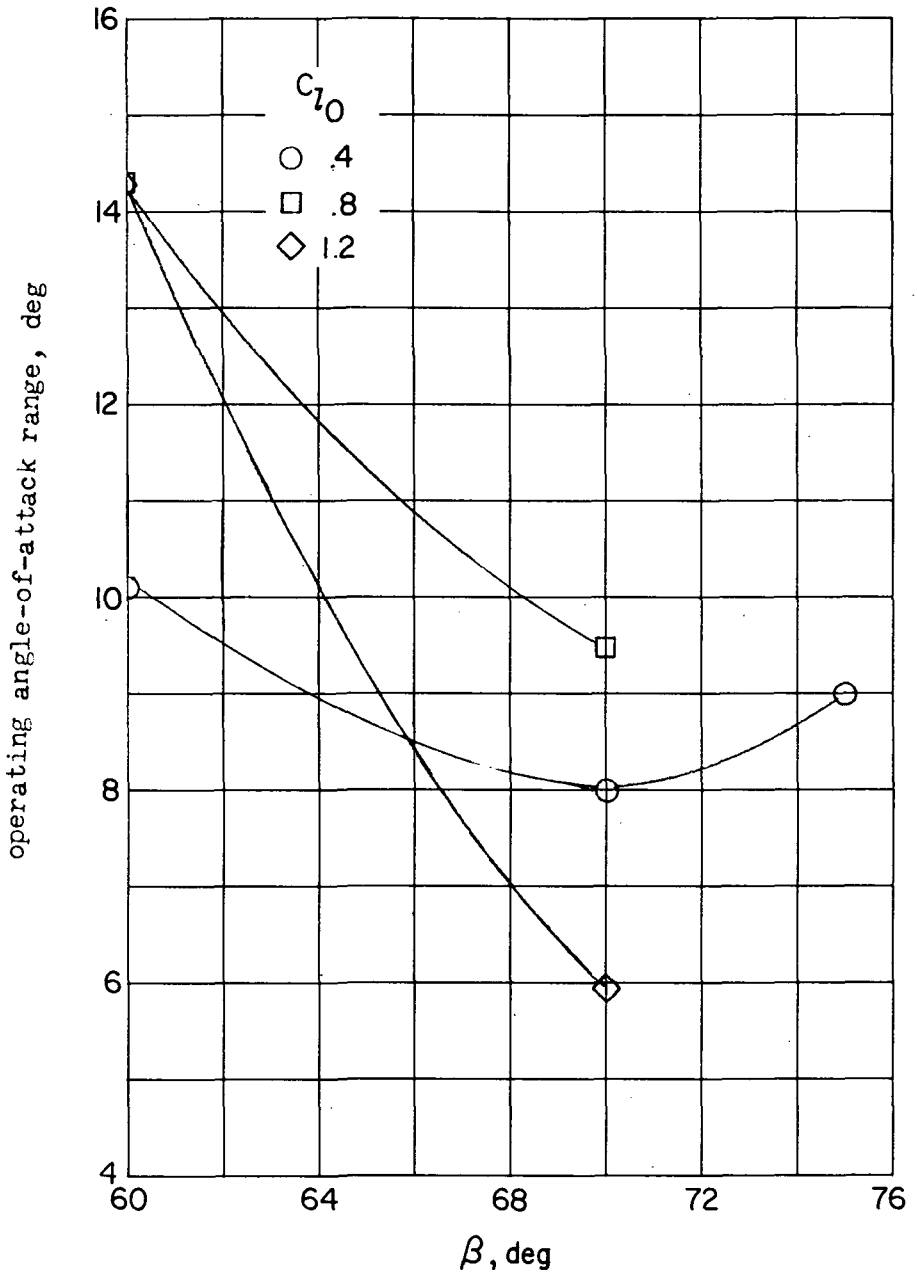

(c) $\sigma = 1.50$.

Figure 33.- Concluded.

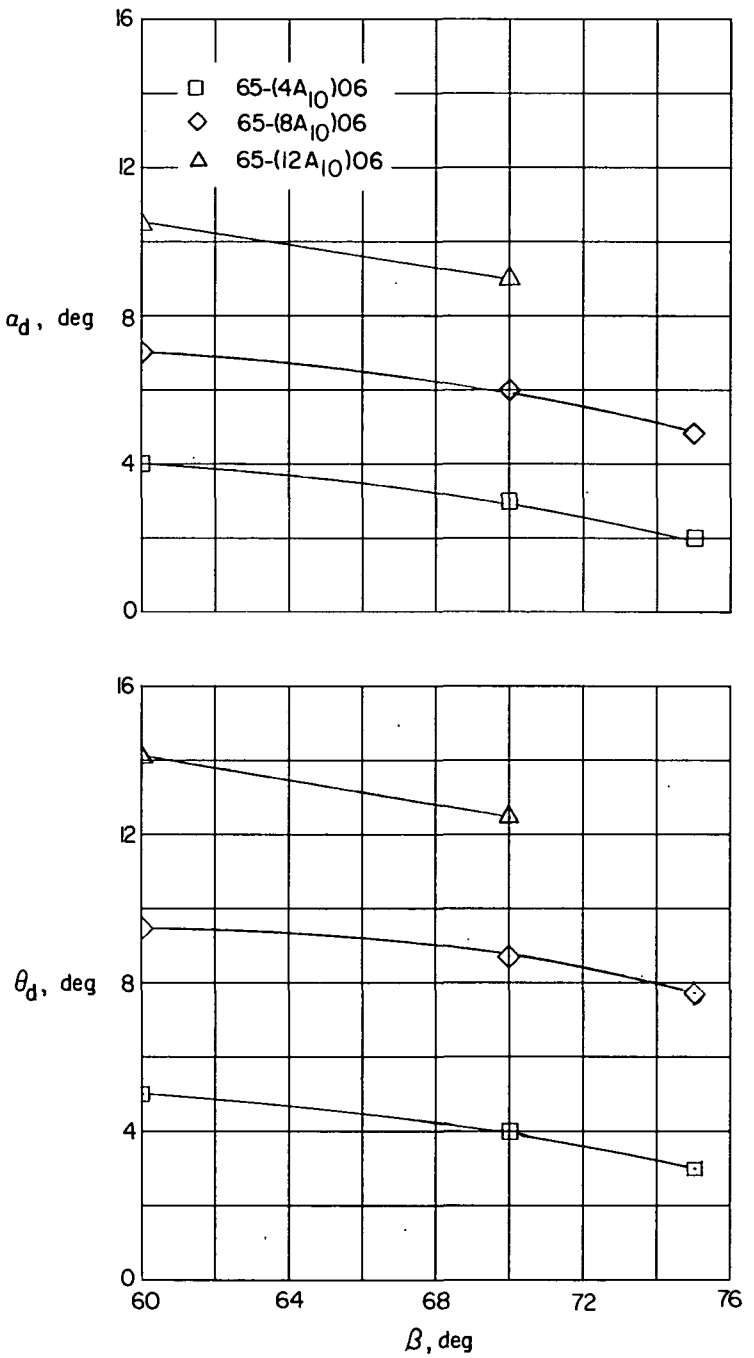

(a) $\sigma = 0.75$.

Figure 34.- Variation of design exit angle and design angle of attack with inlet angle for several NACA 65-series blades.

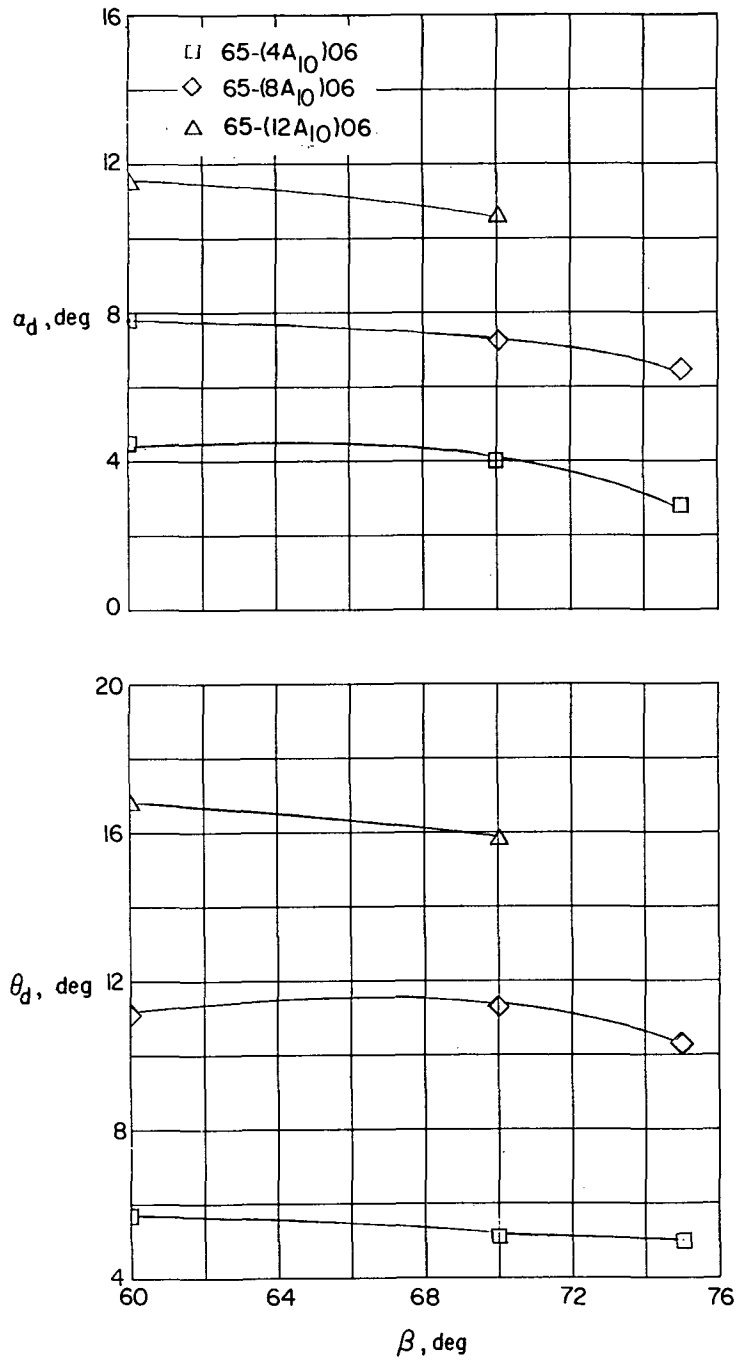

(b) σ = 1.00.

Figure 34.- Continued.

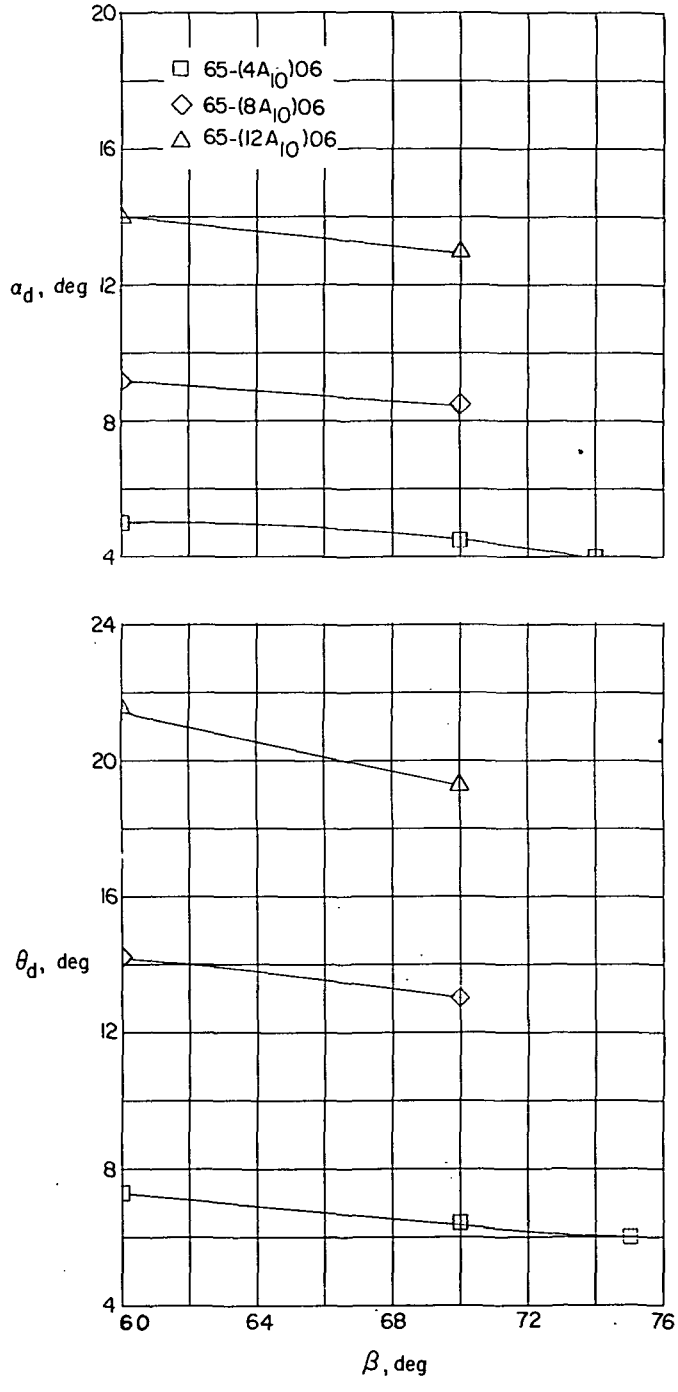

(c) $\sigma = 1.50$.

Figure 34.- Continued.

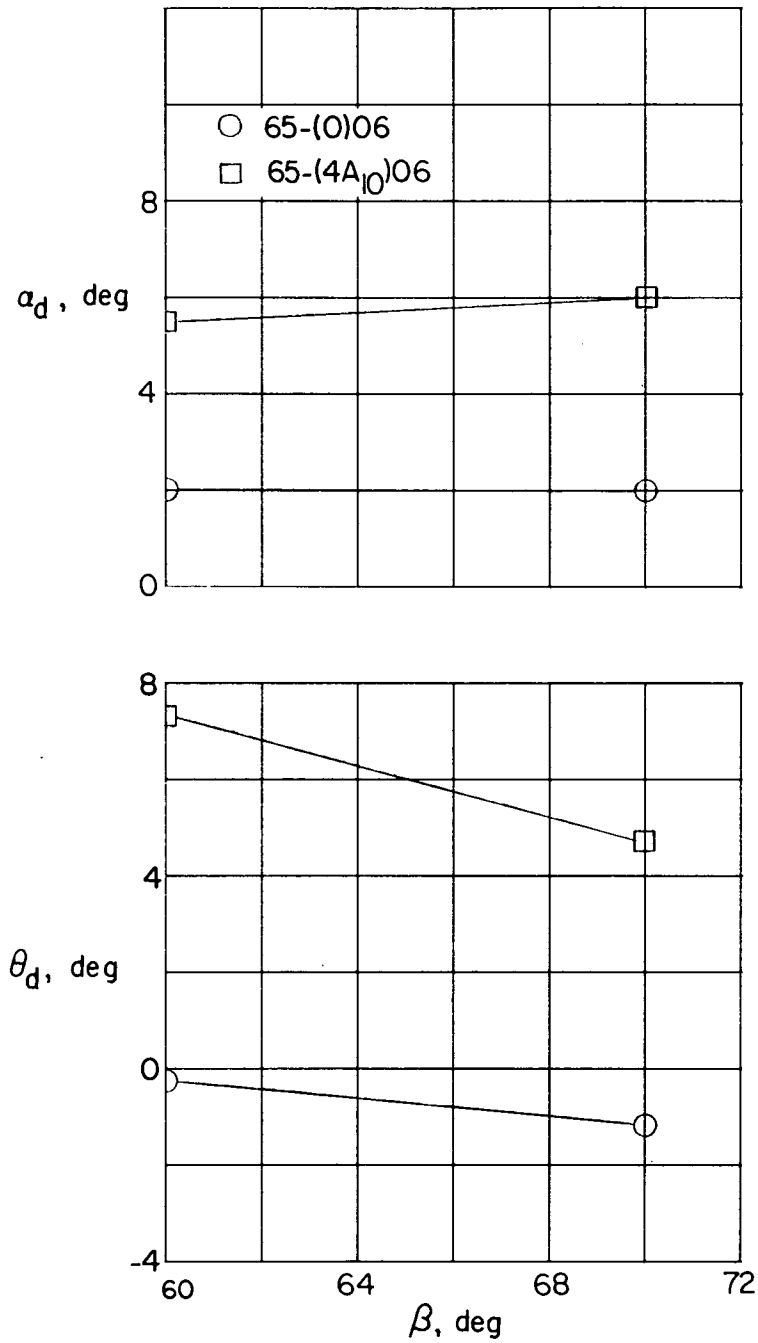

(d) $\sigma = 2.00$.

Figure 34.- Concluded.

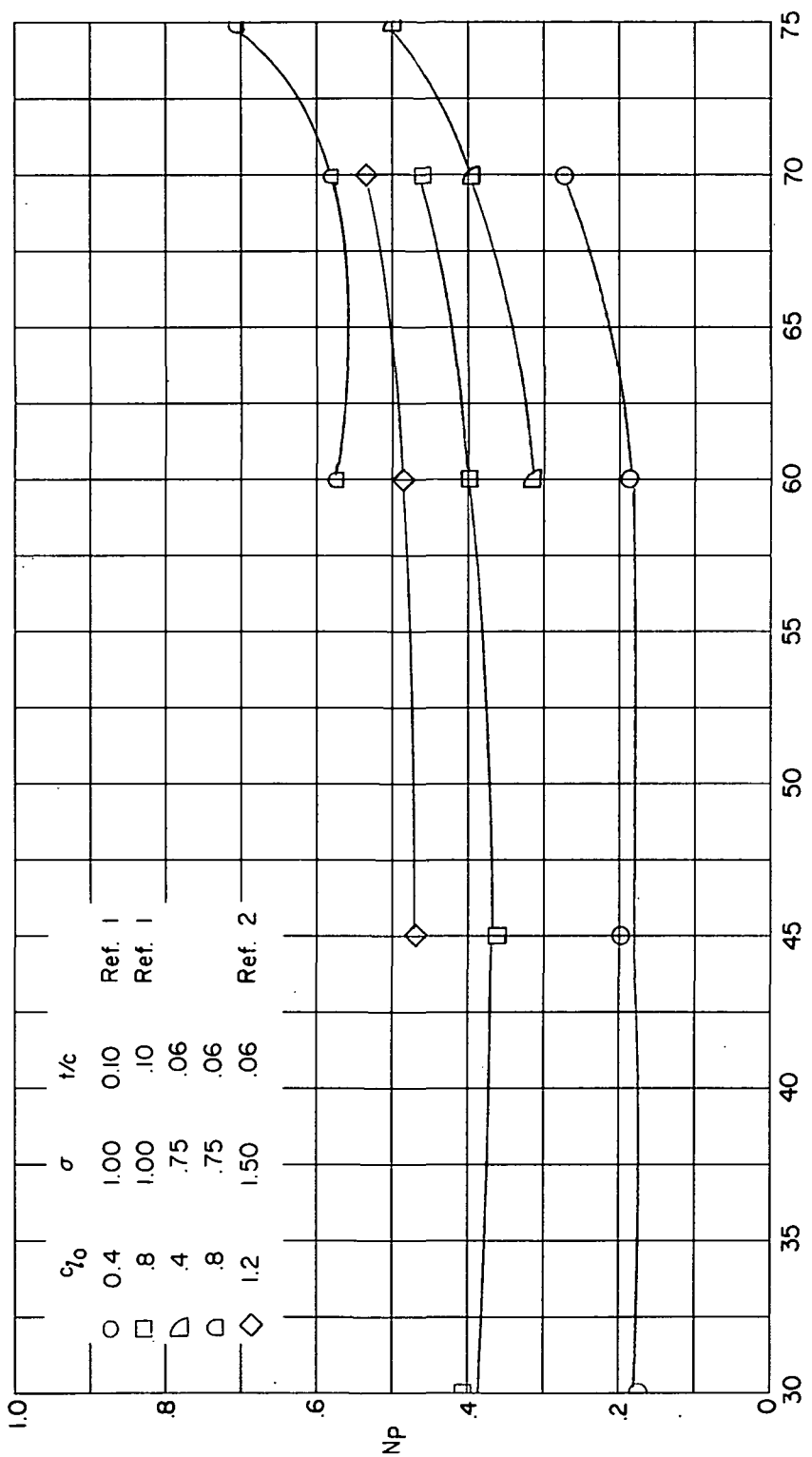

Figure 35.- Variation of c_{N_P} with inlet angle at constant angle of attack for several cambers, solidities, and thickness-chord ratios.

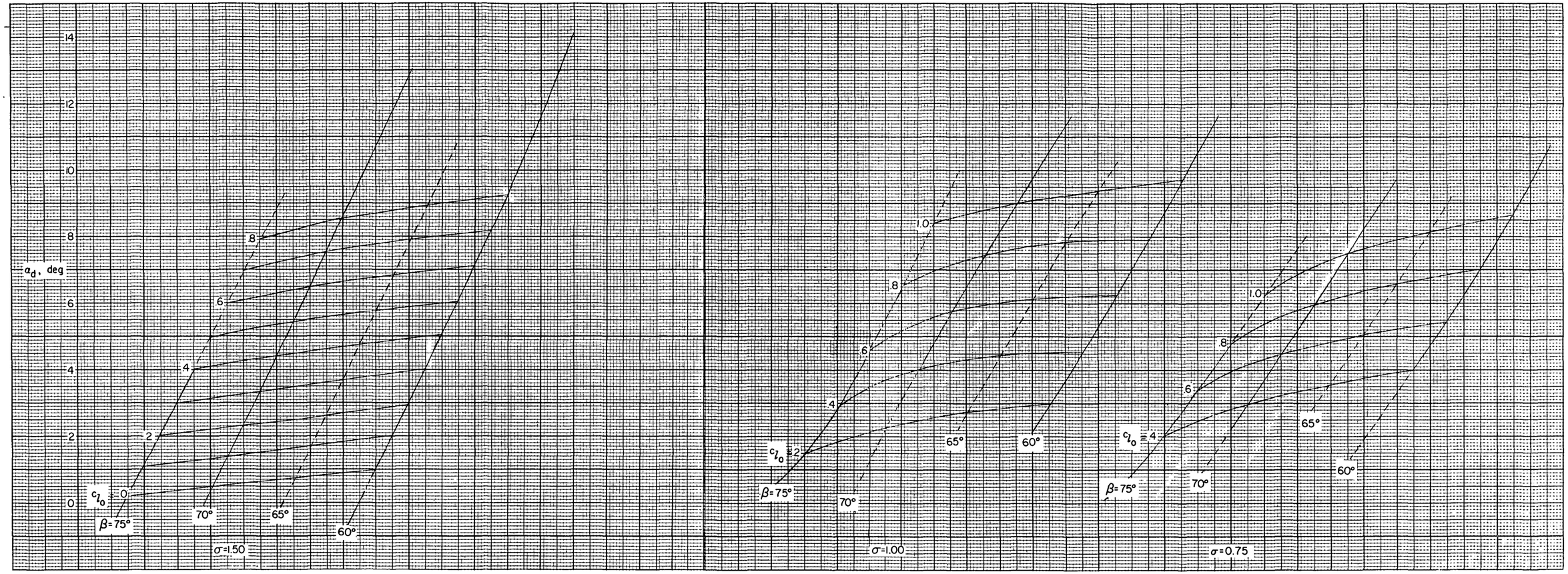

Figure 36.- Design-angle-of-attack carpet plot for the NACA 65-$(c_{l_0}A_{10})$06 blade section at high inlet angles.

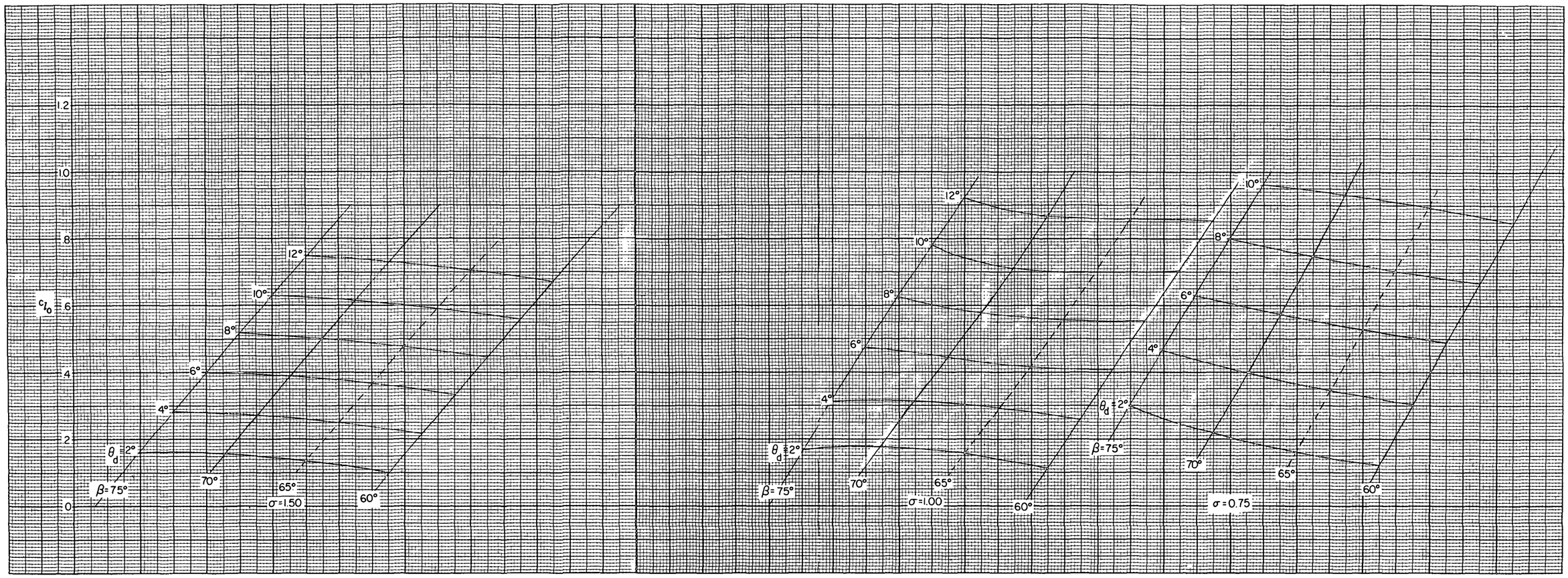

Figure 37.- Design-exit-angle carpet plot for the NACA 65-$(c_{l_0}A_{10})$06 blade section at high inlet angles.